Moritz Blaickner, BSc

Slope stability under consideration of groundwater fluctuations

MASTER'S THESIS

to achieve the university degree of

Diplom-Ingenieur

Master's degree programme: Geotechnical and Hydraulic Engineering

submitted to

Graz University of Technology

Supervisor

Ao.Univ.-Prof. Dipl.-Ing. Dr.techn. M.Sc. tit.Univ.-Prof. Helmut Schweiger

Dipl.-Ing. Georg Michael Ausweger, BSc

Institute of Soil Mechanics and Foundation Engineering

Graz, September 2017

Eidesstattliche Erklärung

Ich erkläre an Eides statt, dass ich die vorliegende Arbeit selbstständig verfasst, andere als die angegebenen Quellen/Hilfsmittel nicht benutzt, und die den benutzten Quellen wörtlich und inhaltlich entnommenen Stellen als solche kenntlich gemacht habe.

Graz, am …… ……

(Unterschrift)

Statutory declaration

I declare that I have authored this thesis independently, that I have not used other than the declared sources / resources, and that I have explicitly marked all material which has been quoted either literally or by content from the used sources.

Graz, …… ……

(signature)

Danksagung

An oberster Stelle gilt mein Dank meinen Eltern, Sonny und Hankrabofzgi. Beide haben mich in den letzten Jahren in allen möglichen und unmöglichen Belangen, sowie in schwierigen Augenblicken ausnahmslos unterstützt. Dies betrifft auch unzählige Momente welche ich nicht mit ihnen geteilt habe, denn oft reicht auch schon der Gedanke daran, um etwas Entspannung einfließen zu lassen.

Mit direktem Bezug auf diese Arbeit, möchte ich mich bei Prof. Dr.techn. Helmut Schweiger bedanken, der es mir ermöglicht hat mich mit diesem interessanten Thema zu befassen und meinen Abschluss am Institut für Bodenmechanik und Grundbau zu absolvieren. Ganz besonderer Dank gilt Dipl.-Ing. Georg Ausweger für die sachlich und persönlich hervorragende Betreuung über die letzten Monate hinweg.

Kurzfassung

Im Zuge dieser Arbeit soll geklärt werden ob zyklische Belastungen in Form von Wasserspiegelschwankungen im Böschungsfußbereich zu einem progressiven Versagen einer Böschung führen können. Hierzu wurden umfangreiche numerische Studien durchgeführt. Einerseits wurde in einer Vorstudie die numerische Standsicherheitsbeurteilung undrainierter Böschungen untersucht. Diese fokussiert sich auf die Unterschiede der in PLAXIS 2D anwendbaren Methoden zur Simulation undrainierten Materialverhaltens (Undrained A, Undrained B und Undrained C, R.B.J. Brinkgreve 2017). Andererseits werden zwei multilaminare Materialgesetze vorgestellt, welche imstande sind Entfestigung zu simulieren. Dies sind, das „Basic model“ (Galavi 2007) und das „Hvorslev model“ (Schädlich 2012). An einfachen Modellen (Triaxialtests und Biaxialtests) wird das Verhalten der multilaminaren Materialmodelle mit dem bekannten „Hardening Soil Small“ Modell verglichen. Dabei werden anhand der festgestellten Unterschiede, Anwendungshinweise für die beiden untersuchten Materialmodelle erarbeitet.

Abschließend werden die beiden multilaminaren Materialmodelle zuerst auf eine vereinfachte Böschung mit einer simulierten Wasserspiegelschwankungen angewendet und die Ergebnisse wiederum mit jenen des Hardening Soil Small Modell verglichen. In einem zweiten Schritt, werden die Einflüsse von Wasserspiegelschwankungen auf eine reale Böschung simuliert um zu klären ob Veränderungen des Wasserspiegels zu einem progressiven Versagen dieser Böschung führen können.

Abstract

In the course of this thesis it should be clarified if cyclic loading in form of groundwater fluctuations could lead to a progressive failure of a slope. For this purpose, extensive numerical studies have been conducted. First, the numerical stability analysis of undrained slopes serve as a preliminary study. This study focuses on the differences between the applicable drainage methods in PLAXIS 2D, concerning the simulation of undrained material behaviour (Undrained A, Undrained B and Undrained C, R.B.J. Brinkgreve 2017). Second, two multilaminate constitutive models with the capability to simulate strain softening, are introduced. These are, the “Basic model” (Galavi 2007) and the “Hvorslev model” (Schädlich 2012). The behaviour of those multilaminate constitutive models is analysed with simple simulations (triaxial tests and biaxial tests), and compared with the “Hardening Soil Small” model. Hints for application for the multilaminate constitutive models are given.

Further on, the multilaminate constitutive models are applied for the simulation of a simple slope, impacted by groundwater fluctuations. The results are compared against to those obtained by the “Hardening Soil Small” model. Conclusively, the influence of groundwater fluctuations impacting a real slope, are simulated to clarify if changes of the groundwater table could lead to a progressive failure.

Table of contents

1 Introduction 1

2 Strength reduction method under undrained conditions 2

2.1 Drainage types in PLAXIS 2D 2016 2

2.1.1 Drainage type (A) 2

2.1.2 Drainage type (B) 2

2.1.3 Drainage type (C) 3

2.2 Undrained shear strength c_u 3

2.3 Stability analysis – Influence of drainage types in case of a simple slope 4

2.3.1 Numerical model and material properties 5

2.3.2 Results 7

2.3.3 Drained vs Undrained (A), (B), (C) 8

2.3.4 Undrained (A) vs Undrained (B), (C) 9

2.3.5 IUB activated / IUB not activated 11

2.3.6 System with / without groundwater table 14

2.4 Conclusion 15

3 Multilaminate framework 17

3.1 Concept of multilaminate models 17

3.2 Mathematical formulations 17

4 Multilaminate models for soils 21

4.1 Basic model 21

4.1.1 Yield criteria 21

4.1.2 Strain hardening 23

4.1.3 Strain softening 24

4.2 Hvorslev model 26

4.2.1 Hvorslev surface and strain softening 27

4.3 Small strain stiffness 28

5 Multilaminate models applied to simple triaxial simulations 30

5.1 Applied constitutive models and material parameters 30

5.2 Axisymmetric / Biaxial simulations without endplates 32
5.2.1 Stress-strain behaviour and Small strain stiffness behaviour 33
5.2.2 Influence of the maximum load fraction 39
5.3 Biaxial simulations with endplate 43
5.3.1 Stress-strain behaviour 44
5.3.2 Determination of softening points 46
5.3.3 Development of softening points due to cyclic loading 48
5.4 Conclusion 50
6 Multilaminate models applied to a simple slope 52
6.1 Numerical model and material parameters 52
6.2 Deformation characteristics 53
6.3 Influence of strain softening on the stability of a simple slope 57
6.3.1 Degree of softening in case of the BMwS depending on the FoS 58
6.4 Softening behaviour of a simple slope due to cyclic loading 61
6.5 Conclusion 61
7 Multilaminate models applied to a real project 63
7.1 Numerical model and material parameters 63
7.2 Results 66
7.3 Conclusion 71
8 Conclusion and outlook 72
9 Bibliography 73

List of figures

Figure 1 Potential stress path Undrained (A) 2
Figure 2 Potential stress path Undrained (B) 3
Figure 3 Potential stress path Undrained (C) 3
Figure 4 Model geometry 5
Figure 5 FE-model with 2384 15-noded elements 5
Figure 6 Comparison of pore pressures - Drained vs Undrained (A) 8
Figure 7 Comparison of effective stresses - Drained vs Undrained (A) 9
Figure 8 Geometric relationship strength - reduction method (undrained) 9
Figure 9 Comparison of Mohr circles for drainage type Undrained (A) and (B) 10
Figure 10 Comparison of pore pressures - IUB activated vs IUB not activated 12
Figure 11 Mohr circles for Undrained (A) / (A) IUB, Mohr Coulomb 12
Figure 12 Mohr circles for Undrained (B) / (B) IUB, Mohr Coulomb 13
Figure 13 Comparison of pore pressures - Drainage type Undrained (A) / (A) IUB 13
Figure 14 Comparison of pore pressures - Drainage type Undrained (B) / (B) IUB 14
Figure 15 Comparison of pore pressures - with / without GW table 15
Figure 16 Comparison of pore pressures - with / without GW table 15
Figure 17 General concept of multilaminate models, (Wiltafsky 2003) 18
Figure 18 Integration plane orientation, (Schädlich 2012) 18
Figure 19 Local stress components, (Schädlich 2012) 18
Figure 20 Yield and failure criterion on an integration plane, (Galavi 2007) 22
Figure 21 Deviatoric hardening, (Galavi 2007) 23
Figure 22 Volumetric hardening, (Galavi 2007) 24
Figure 23 Linear strain softening in relation to the damage strain, (Galavi 2007) 25
Figure 24 a) Friction softening, b) Cohesion softening, c) Friction and cohesion softening, (Galavi 2007) 26
Figure 25 Failure of Wiener Tegel, (Schädlich 2012) 27
Figure 26 Normalized yield surface on integration plane level, (Schädlich 2012) 27
Figure 27 Degradation of small strain stiffness behaviour and transition to large strain behaviour, (Schädlich 2012) 29
Figure 28 Macroscopic (a) and local (b) degradation of small strain stiffness, (Schädlich 2012) 29
Figure 29 Model geometry and loading / unloading cycle, Number of 15-noded elements: 72 32
Figure 30 Axisymmetric / Biaxial model - Stresses, Strains and failure points indicate a uniform response 33

Figure 31 Axisymmetric / Biaxial tests; Stress-strain curves for all models, Phase 2 – Phase 4 34
Figure 32 Axisymmetric / Biaxial tests; p'-q curves for all models, Phase 1 – Phase 4 34
Figure 33 Biaxial Tests; Cartesian stress - strain curves for all models, Phase 1 – Phase 4 35
Figure 34 Axisymmetric Tests; Small strain / unloading / reloading stiffness with $q_{vertical,max}$, Phase 1 – Phase 4 36
Figure 35 Axisymmetric tests; Small strain / unloading / reloading stiffness with $q_{vertical,max}$ – 2 kPa, Phase 1 – Phase 4 37
Figure 36 Axisymmetric tests; Stress-strain curves with $q_{vertical,max}$ – 2 kPa, Phase 2 – Phase 4 37
Figure 37 Axisymmetric tests, Small strain / unloading / reloading stiffness with $q_{vertical,max}$ = 190 kPa for the BMwS, Phase 1 – Phase 4 38
Figure 38 Axisymmetric tests; Stress-strain curves with $q_{vertical,max}$ = 190 kPa for the BMwS, Phase 2 – Phase 4 38
Figure 39 Influence of the maximum load fraction on the HSS model 39
Figure 40 Influence of the maximum load fraction on multilaminate models 40
Figure 41 Total displacements due to cyclic loading with LF = 0.5 41
Figure 42 Relative displacements between the loading cycles with LF = 0.5 41
Figure 43 Total displacements due to cyclic loading with LF = 0.05 42
Figure 44 Relative displacements between the loading cycles with LF = 0.05 42
Figure 45 Model geometry and loading / unloading cycle, Number of 15-noded elements: 96 43
Figure 46 Biaxial models with end plates: Incremental deviatoric strains and plastic points indicate a non-uniform response 44
Figure 47 Biaxial tests; Stress-strain curves for all models at point L, Phase 2 – Phase 4 45
Figure 48 Biaxial tests; Stress-strain curves for all models at point K, Phase 2 – Phase 4 46
Figure 49 Comparison of softening points (SP) vs. failure points (FP) – BMwS 47
Figure 50 Comparison of softening points (SP) vs. failure points (FP) – HM 47
Figure 51 Total displacements due to cyclic loading at point A 48
Figure 52 Relative displacements between the loading cycles at point A 49
Figure 53 Development of the softening rate for the stress point with the minimum strength values 50
Figure 54 Mean softening rate for all stress points in softening 50
Figure 55 FE-model with 880 15-noded elements 52

Figure 56 Displacements of point A / C during phase 3 and 4 for all models 54
Figure 57 Displacements of point A / C during phase 3 and 4 for the Basic models 54
Figure 58 Displacements of the slope surface after phase 4 (consolidation) for all models 55
Figure 59 Displacements of the slope surface after phase 4 (consolidation) for the BMwS and the BMnS 55
Figure 60 Total amount of failure points (failure point history) after phase 4 (consolidation).....56
Figure 61 Softening rate of φmin and $cmin$ for different FoS after phase 6 59
Figure 62 Mean softening rate of $\varphi res,\ mean$ and $cres,\ mean$ for different FoS after phase 6 59
Figure 63 Total amount of failure points (failure point history) for different FoS – Phase 6 (consolidation).....60
Figure 64 Percentage of stress points / integration planes in softening for different FoS after phase 6 60
Figure 65 FE-model (Length: 400 m, Height: 360 m).....64
Figure 66 Section of the FE-model, GW-tables (BMwS).....66
Figure 67 BMwS with high residual parameters / BMnS - Total displacements for points A, D, H 67
Figure 68 BMwS with low residual parameters / BMnS - Total displacements for points A, D, H 67
Figure 69 BMwS with high residual parameters - Total displacements vs time for points A, D, H 68
Figure 70 BMwS with low residual parameters - Total displacements vs time for points A, D, H 68
Figure 71 BMnS - Development of failure points (FP).....69
Figure 72 BMwS with high residual strength parameters - Development of failure points (FP).....69
Figure 73 BMnS with low residual strength parameters - Development of failure points (FP).....70
Figure 74 BMwS with high residual parameters - Mean softening rate of $\varphi_{res,mean}$ and $c_{res,mean}$ for all softening soils.....70
Figure 75 BMwS with low residual parameters - Mean softening rate of $\varphi_{res,mean}$ and $c_{res,mean}$ for all softening soils.....71

List of tables

Table 1 Model properties 6
Table 2 Selected points 6
Table 3 Factors of safety 7
Table 4 Material parameters 31
Table 5 Summary loading / unloading cycle 32
Table 6 Summary loading / unloading cycle 43
Table 7 Initial material parameters 53
Table 8 Selected points 53
Table 9 Strength parameters with corresponding FoS for all models 57
Table 10 Strength parameters with corresponding FoS for the BMwS 58
Table 11 Material parameters for soils with softening behaviour 65

List of symbols and abbreviations

Capital letters

A_i	[m²]	Area of influence of an integration plane
A_d	[-]	Scaling parameter to control the relative proportion of distortional and volumetric degradation
A_{mat}	[-]	Deviatoric hardening parameter
A_{sphere}	[m²]	Surface area of a unit sphere
$A_{vol/dev}$	[-]	Softening strain weighting of volumetric to deviatoric strains for the Basic model
B_{CS}	[-]	Parameter to define the position of the critical state line
C_i	[-]	Local elastic compliance matrix on integration plane
E	[kPa]	Young's modulus
E_{50}	[kPa]	Deviatoric hardening modulus
$E_{50,ref}$	[kPa]	Deviatoric hardening modulus at reference pressure
$E_{oed,ref}$	[kPa]	Stiffness in compression at reference pressure
E_u	[kPa]	Undrained stiffness
E_{ur}	[kPa]	Stiffness in un-/reloading
$E_{ur,ref}$	[kPa]	Stiffness in un-/reloading at reference pressure
G	[kPa]	Shear modulus
G_0	[kPa]	Initial shear modulus at small strain
$G_{0,ref}$	[kPa]	Initial shear modulus at small strain at reference pressure
$G_{tan,ref}$	[kPa]	Shear modulus at reference pressure
G_{ur}	[kPa]	Un- / reloading shear modulus
K	[-]	Hardening parameter
K_0	[-]	Lateral earth pressure coefficient at rest
K_{0nc}	[-]	Lateral earth pressure coefficient at rest for normally consolidated conditions
L_{cal}	[m]	Internal length for non-local regularization
M_α	[-]	Shape factor determining the shape of the volumetric part of the yield curve
R_f	[-]	Failure ratio
T_i	[-]	Transformation matrix of integration plane i

Small letters

c'	[kPa]	Effective cohesion

c'_{HV}	[kPa]	Cohesion intercept of Hvorslev surface in τ - σ' - diagram, normalised with σ'_{ne}
c'_{min}	[kPa]	Softening point with minimum effective cohesion
c'_{mob}	[kPa]	Mobilized effective cohesion
c'_{peak}	[kPa]	Effective cohesion at peak strength
c'_{res}	[kPa]	Effective cohesion at residual strength
$c'_{res,mean}$	[kPa]	Mean effective cohesion of all softening points
c_u	[kPa]	Undrained shear strength
c'_{ve}	[kPa]	Cohesion intercept of Hvorslev surface in τ - σ' - diagram, normalised with σ'_{ve}
f_t	[-]	Tension yield function
f_d	[-]	Deviatoric yield function
f_{HV}	[-]	Hvorslev yield function
f_v	[-]	Volumetric yield function
g_i	[-]	Local plastic potential function on integration plane
h_{soft}	[-]	Softening parameter for the Hvorslev model
i	[-]	Index number of integration plane
m	[-]	Power of stress dependency
$m_{soft,\varphi}$	[-]	Rate of friction softening
$m_{soft,c}$	[-]	Rate of cohesion softening
n_i	[-]	Local normal vector of integration plane
n_{CP}	[-]	Number of sampling planes
p'	[kPa]	Mean effective stress
p_{excess}	[kPa]	Excess pore water pressure
p_{water}	[kPa]	Pore water pressure
p_{ref}	[kPa]	Reference pressure
q	[kPa]	Deviatoric stress
s_i	[-]	Local unit vector in s - direction on integration plane
t_i	[-]	Local unit vector in t - direction on integration plane
w_i	[-]	Weighting coefficient of sampling planes

Greek letters

α_i	[°]	Orientation angle of integration plane
β_i	[°]	Orientation angle of integration plane
γ	[kPa]	Unit weight of soil
$\gamma_{0.7}$	[-]	Shear strains at 70% of G_0

γ_s	[-]	Local shear strains in s - direction on integration plane
γ_t	[-]	Local shear strains in t - direction on integration plane
γ_{xy}	[-]	Global shear strain
Δc_u	[kPa]	Increase of undrained shear strength with depth
$\Delta\varepsilon_{n,v}^p$	[-]	Plastic normal strain increment from the volumetric yield curve
ε	[-]	Global strain tensor
$\varepsilon_{\gamma,d}^p$	[-]	Plastic shear strain from the deviatoric yield curve
$\varepsilon_{\gamma,i}^p$	[-]	Local plastic shear strain on integration plane from all yield surfaces
ε_{deg}	[-]	Local degradation strain
$\varepsilon_{deg,1}$	[-]	Local degradation strain defining onset of stiffness degradation
$\varepsilon_{deg,2}$	[-]	Local degradation strain defining transition to large strains
ε_{di}	[-]	Local damage strain on integration plane
$\varepsilon_{di,peak}$	[-]	Local damage strain on integration plane at peak level
ε_i	[-]	Local strain tensor on integration plane
ε_i^e	[-]	Local elastic strain tensor on integration plane
ε_i^p	[-]	Local plastic strain tensor on integration plane
ε_n	[-]	Local normal strain on integration plane
$\varepsilon_{n,i}^p$	[-]	Local plastic normal strain on integration plane from all yield surfaces
ε_{xx}	[-]	Global normal strain tensor
Λ_i	[-]	Local plastic multiplier
ν	[-]	Poisson's ratio
ν'	[-]	Drained Poisson's ratio
ν_u	[-]	Undrained Poisson's ratio
ν_{ur}	[-]	Poisson's ratio for un- / reloading
σ'	[kPa]	Effective stresses
σ_i'	[kPa]	Effective stress vector in terms of micro level components of plane i
σ_n'	[kPa]	Effective normal stress on integration plane
σ_{nc}'	[kPa]	Effective normal preconsolidation stress of structured soil on integration plane
$\sigma_{nc}'^*$	[kPa]	Effective normal preconsolidation stress of reconstituted soil on integration plane
$\sigma_{nc,i}'^*$	[kPa]	Initial effective normal preconsolidation stress of reconstituted

		soil on integration plane
$\sigma_{ne}^{\prime *}$	[kPa]	Equivalent normal stress on local normal consolidation line
σ_s'	[kPa]	Effective normal stress at the intersection point f_d - f_v
σ_t'	[kPa]	Tensile strength
σ_{ve}'	[kPa]	Equivalent vertical stress on 1D - normal consolidation line
σ_{xx}'	[kPa]	Horizontal effective stress
σ_{yy}'	[kPa]	Vertical effective stress
τ	[kPa]	Local shear stresses on integration plane
τ_s	[kPa]	Local shear stresses in s - direction on integration plane
τ_t	[kPa]	Local shear stresses in t - direction on integration plane
φ	[°]	Friction angle
φ'	[°]	Effective friction angle
φ_{CS}'	[°]	Effective critical state friction angle
φ_e'	[°]	Inclination of the Hvorslev surface
φ_i'	[°]	Mobilised effective friction angle related to the initial stress state
φ_{min}'	[°]	Softening point with minimum effective friction angle
φ_{mob}'	[°]	Mobilised effective friction angle
φ_{mod}'	[°]	Modified effective friction angle
φ_{peak}'	[°]	Effective friction angle at peak strength
φ_{res}'	[°]	Effective friction angle at residual strength
$\varphi_{res,mean}'$	[°]	Mean effective friction angle of all softening points
φ_u	[°]	Undrained friction angle

Abbreviations

BMwS	Basic model with strain softening
BMnS	Basic model no strain softening
FE	Finite Element
FoS	Factor of safety
FP	Failure Points
HSS	Hardening Soil model with small strain stiffness
HM	Hvorslev model
IUB	Ignore undrained behavior
LF	Maximum load fraction
MaxPoint	Maximum number of stress points for non-local regularization
OCR	Over-consolidation rate
SP	Softening points

SR	Softening rate
$SSS_{recovery}$	Recovery of small strain stiffness at strain reversal, 0 = no recovery and 1 = full recovery
SWCC	Soil water characteristic curve

1 Introduction

Many fine-grained soils exhibit strain softening after a certain amount of deformation until they reach their critical state, or residual strength. This circumstance is a well-known issue and has been investigated on sites and verified in laboratory tests for many years. However, the classical approach in soil mechanics is to use constant strength parameters with no consideration of further deformations. In many cases this classical approach is sufficient, especially for systems far away from failure state or soils with a brittle behaviour. Nonetheless, constant strength parameters may not be suitable for soils which show a progressive decrease of strength parameters (softening) with increasing deformations. Particularly, slow moving slopes are often influenced by decreasing strength parameters along a certain slip surface, thus resulting in a progressive failure.

Recurring loading cycles are often the trigger of such slow, but progressive movements. Such cycles could be caused, e.g. by natural events like heavy falls, or water level fluctuations in a reservoir of a power plant.

To evaluate the behaviour of such systems is a difficult task, either with empirical or analytical and numerical methods. Although numerical methods employ the most advanced constitutive models, concerning softening behaviour, this is still a field of research. In general, these constitutive models are considerably more complex than the common known material models. This issue makes an appropriate input and interpretation of simulations more difficult and usually requires a higher computational effort.

Accordingly, the main objective of this thesis was the evaluation of slope movements influenced by cyclic loading and strain softening. Furthermore, the general behaviour and potential numerical issues of two constitutive material models, capable of simulating strain softening, were investigated. The two constitutive models presented are namely the Basic model (Galavi 2007) and the Hvorslev model (Schädlich 2012), both based on the multilaminate framework. Additionally, a preliminary study was carried out to gain a better understanding, concerning the determination of the factor of safety of slopes under undrained conditions.

2 Strength reduction method under undrained conditions

The numerical tests reported in this chapter have been conducted to study the different Factors of Safety (FOS), resulting from different drainage types as Undrained (A), (B), (C) (R.B.J. Brinkgreve, 2017) and Drained, under various boundary conditions. These simulations are intended to discuss which conditions during a safety analysis lead to the most appropriate Factor of Safety for slopes under undrained conditions. The following investigations serve as a preliminary study. As most slope stability analysis in this thesis are performed under undrained conditions, the main issue of this study is to gain a better understanding of the determination of the safety factor under undrained conditions. However, the issues of this preliminary study are a separate field of research. In the course of this comparison, only some general aspects are going to be discussed in addition to some basic information concerning undrained simulations.

2.1 Drainage types in PLAXIS 2D 2016

2.1.1 Drainage type (A)

Drainage type Undrained (A) allows to model undrained conditions in terms of an effective stress analysis using effective strength parameters (c', φ) and effective stiffness parameters (e.g. E'_{50}, ν'). Generally, a realistic prediction of pore pressures is generated. The undrained shear strength c_u is an outcome of the constitutive model, not an input parameter, but the resulting undrained shear strength c_u should be compared against existing data (R.B.J. Brinkgreve, 2017).

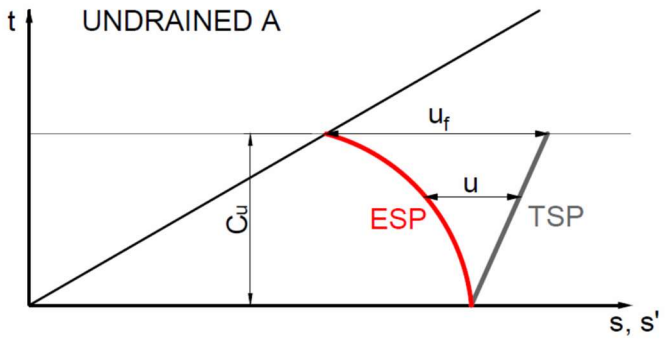

Figure 1 Potential stress path Undrained (A)

2.1.2 Drainage type (B)

Drainage type Undrained (B) allows to model undrained conditions in terms of a "combined" analysis using undrained strength parameters $(c = c_u, \varphi = \varphi_u)$ and effective

stiffness parameters (e.g. E'_{50}, ν'). Generally, an unrealistic prediction of pore pressures is generated. The undrained shear strength c_u is an input parameter (R.B.J. Brinkgreve, 2017).

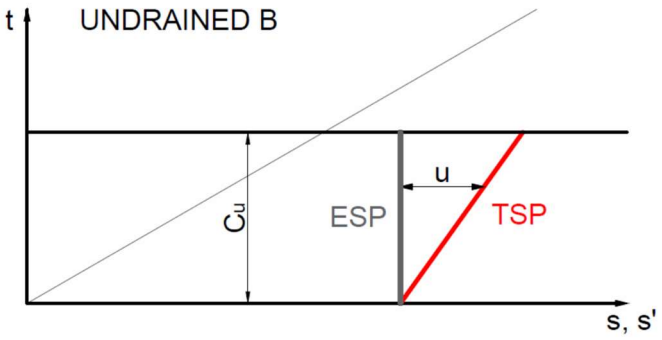

Figure 2 Potential stress path Undrained (B)

2.1.3 Drainage type (C)

Drainage type Undrained (C) allows to model undrained conditions in terms of a total stress analysis using undrained strength parameters ($c = c_u, \varphi = \varphi_u = 0$) and undrained stiffness parameters (E_u, ν_u). Assuming constant volume behaviour under undrained conditions, Poisson's ratio $\nu = 0{,}5$. However, this value is impossible in the current numerical implementation because it would lead to a singularity of the stiffness matrix, thus ν_u = 0.495 – 0.499 [-] is usually used. There is no prediction of pore water pressures ($p = 0$) and all stresses have to be interpreted as total stresses. The undrained shear strength c_u is an input parameter (R.B.J. Brinkgreve, 2017).

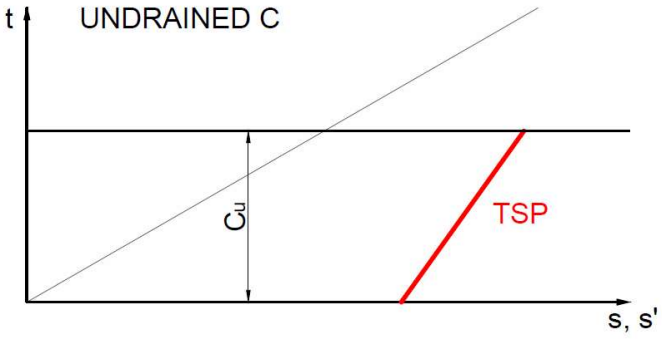

Figure 3 Potential stress path Undrained (C)

2.2 Undrained shear strength c_u

The undrained shear strength c_u (= s_u) can be characterized as the shear strength of fine-grained soils under undrained conditions. The parameter is governed by effective stresses. In case of a Mohr Coulomb failure criterion (Undrained A), c_u increases with depth and can be calculated as follows:

$$c_u = \Delta c_u + c \cos \varphi \quad (1)$$

$$\Delta c_u = \frac{1}{2}(K_0 + 1)\sigma'_{yy} \sin \varphi \quad (2)$$

$$\Delta c_u = \frac{1}{2}(\sigma'_{xx} + \sigma'_{yy})\, sin\, \varphi \quad (3)$$

$$K_0 = 1 - sin\, \varphi \quad (4)$$

$$K_0 = \frac{\nu}{1 - \nu} \quad (5)$$

c_u	[kPa]	Undrained shear strength
Δc_u	[kPa/m]	Increase of shear strength with depth
K_0	[-]	Coefficient of lateral pressure
σ'_{yy}	[kPa]	Vertical effective stress
σ'_{xx}	[kPa]	Horizontal effective stress
φ	[°]	Friction angle
c	[kPa]	Cohesion
ν	[-]	Poisson number

K_0 can be calculated in two different ways, (formula (3) and formula (4)) with usually different results. It is essential to note, that in terms of comparing the behaviour of Undrained (A), (B) and (C), K_0 has to be consistent for all three drainage types. For the following calculations, c_u has been calculated with K_0 deriving from formula (5).

2.3 Stability analysis – Influence of drainage types in case of a simple slope

Two constitutive models are compared in this chapter; the Mohr Coulomb model and the Hardening Soil model. Regarding the boundary conditions, three distinctions have been made:

- Undrained excavation without groundwater table and an undrained safety analysis
- Undrained excavation without groundwater table and a drained safety analysis
- Undrained excavation with groundwater table and an undrained safety analysis

Simulations of an excavated slope with a consecutive safety analysis (Chapter 2.3.1) have been made with all available drainage types, namely Undrained (A), Undrained (B), Undrained (C) and Drained.

2.3.1 Numerical model and material properties

The numerical model is a plane strain simulation of an excavation, creating a simple slope (Figure 4 and Figure 5). The simulated phases are:

- Initial phase (K_0-procedure)
- Undrained excavation phase
- Safety analysis

The excavation creates positive excess pore pressures for drainage type (A) and (B). Referring to PLAXIS 2D, positive pore pressures are associated with stabilizing pore pressures in this thesis.

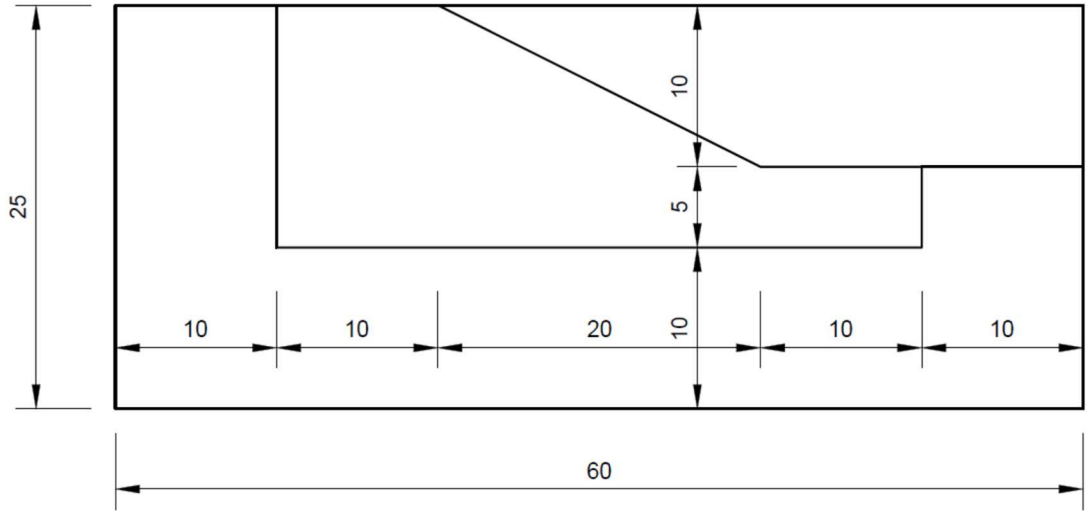

Figure 4 Model geometry

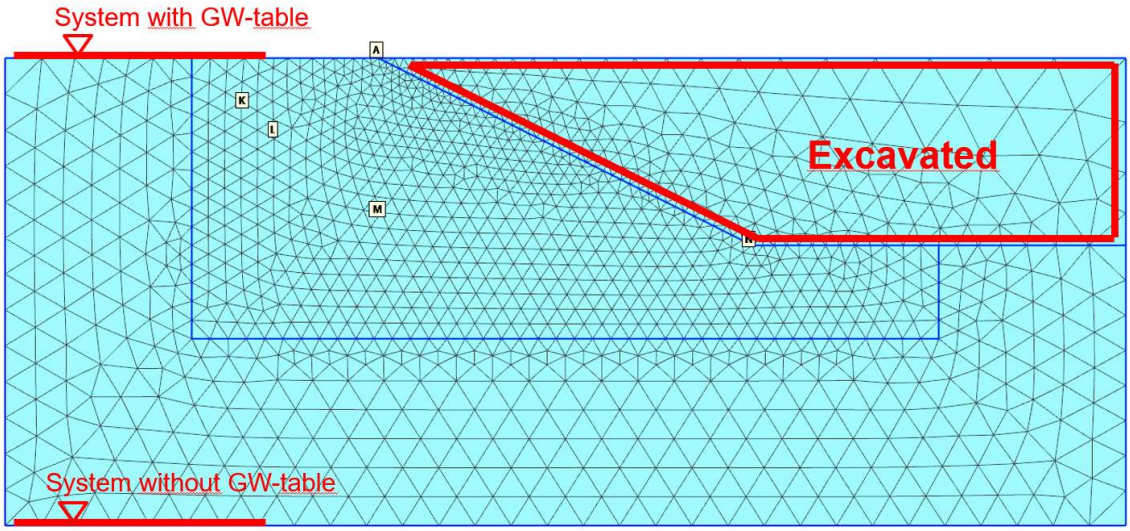

Figure 5 FE-model with 2384 15-noded elements

The following tables present the material properties (Table 1) and the coordinates of the selected nodes of interest (Table 2), respectively. The coordinates of the selected nodes vary in a small range between the different calculation types, as the nodes were situated directly in the slip surface. The calculations were also performed with a higher / lower number of elements as well as with 6-noded elements; no significant differences could be observed. The abbreviation IUB indicates that the option “Ignore undrained behaviour” is activated (e.g. Table 2). This term derives from PLAXIS 2D and means that an undrained material behaves like a drained material for the selected phase (R.B.J. Brinkgreve, 2017). In this thesis, IUB only is active during the safety analysis if activated.

Table 1 Model properties

	Mohr Coulomb			**Hardening Soil**	
	Undrained (A)	**Undrained (B)**	**Undrained (C)**	**Undrained (A)**	**Undrained (B)**
γ [kPa] =	20	20	20	20	20
E / E_u [kPa] =	7500	7500	9375		
ν / ν_u [-] =	0.35	0.35	0.495		
c' [kPa] =	20			20	
φ' / φ_u [°] =	20	20		20	
c_u [kPa] =		18.79	18.79		18.79
Δc_u [kPa/m] =		5.262 / 2.631	5.262 / 2.631		5.262 / 2.631
E_{50} [kPa] =				7500	7500
$E_{oed,ref}$ [kPa] =				7500	7500
E_{ur} [kPa] =				25000	25000
m [-] =				1	1
p_{ref} [kPa] =				100	100
K_{0nc} [-] =				0.5385	0.5385

Table 2 Selected points

			Selected Points				
			A	**K**	**L**	**M**	**N**
System without groundwater table	**Drained**	**x**	19.9	16.88	18.01	25.74	39.82
		y	0	-2.63	-4.22	-8.6	-10.11
	(A), (A)IUB only for HS model, (B), (B)IUB	**x**	19.9	12.7	14.35	19.92	39.82
		y	0	-2.67	-4,22	-8.49	-10.11

	(A)IUB only for MC model	**x**	19.9	14.3	15.85	21.28	39.82
		y	0	-2.64	-4.21	-8.61	-10.11
	(C)	**x**	19.9	13.24	14.52	19.92	39.82
		y	0	-2.61	-4.31	-8.49	-10.11
System with groundwater table	**Drained, (C)**	**x**	19.9	12.7	14.35	18.75	39.82
		y	0	-2.67	-4.22	-8.61	-10.11
	(A), (B)	**x**	19.9	12.7	14.35	20.25	39.82
		y	0	-2.67	-4.22	-8.56	-10.11

2.3.2 Results

Table 3 shows the summarized factors of safety for the various simulations. The matrix row “Drained” indicates drained behaviour for all phases whereas, the matrix columns “IUB” (= Ignore undrained behaviour in PLAXIS 2D) indicate drained behaviour only during the safety analysis. An “error” indicates a failure during the excavation process. Hence, these calculations could not be completed and cannot be compared with the other calculations. The parameter Δc_u (Formula (2) and (3)) is an input value only for Undrained (B) and Undrained (C). If not declared otherwise, Δc_u = 5.262 kPa/m for all simulations. In case of the systems with groundwater table, simulations with an adjusted value of Δc_u = 2.631 kPa/m have been carried out. Crossed out cells are calculations, which cannot be performed.

Table 3 Factors of safety

	Factors of safety							
	Mohr Coulomb				**Hardening Soil**			
	System without Groundwater table		**System with Groundwater table**		**System without Groundwater table**		**System with Groundwater table**	
Drained (all phases)	1.77	**IUB**	error	**Δc_u = 2.631**	1.76	**IUB**	error	**Δc_u = 2.631**
Undrained (A)	2.29	2.8	1.48		2.4	2.58	1.47	
Undrained (B)	2.24	2.24	2.24	1.44	2.24	2.24	2.23	1.44
Undrained (C)	2.24		2.24	1.44				

Depending on the respective boundary conditions, constitutive model and used drainage type, the FoS ranges from 1.76 to 2.8. This wide range of results will be discussed in detail in the following chapters.

2.3.3 Drained vs Undrained (A), (B), (C)

All undrained simulations are producing significantly higher FoS-Values (FoS = 2,24 – 2,4) than the drained simulations (FoS = 1,76 – 1,77), looking at the systems without groundwater table. In case of Undrained (A) this is a result of the excavation process. The removal of the soil cluster leads to an unloading stress path which causes positive excess pore pressures and therefore higher effective stresses (Figure 7). Those stabilizing positive pore pressures are of course absent in the drained simulation where no pore pressures develop. Figure 6 shows a representative example of the developing pore pressures over the calculation progress. In case of drainage type Undrained (B) and Undrained (C), the FOS derives from the maximum deviatoric stresses, which are approaching the decreasing undrained shear strength c_u during the safety analysis. Although excess pore pressures are calculated for Undrained (B), the shear strength is unaffected by any shift of the mean stresses (Figure 12), therefore $FOS_{Undrained\ (B)} = FOS_{Undrained\ (C)}$.

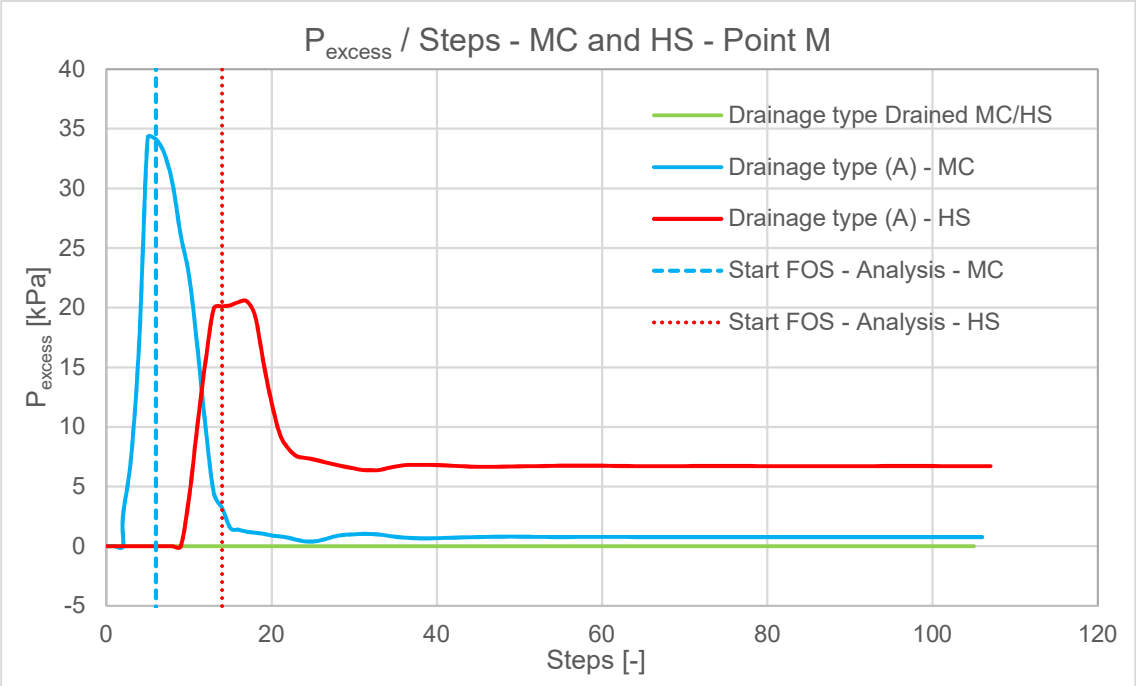

Figure 6 Comparison of pore pressures – Drained vs Undrained (A)

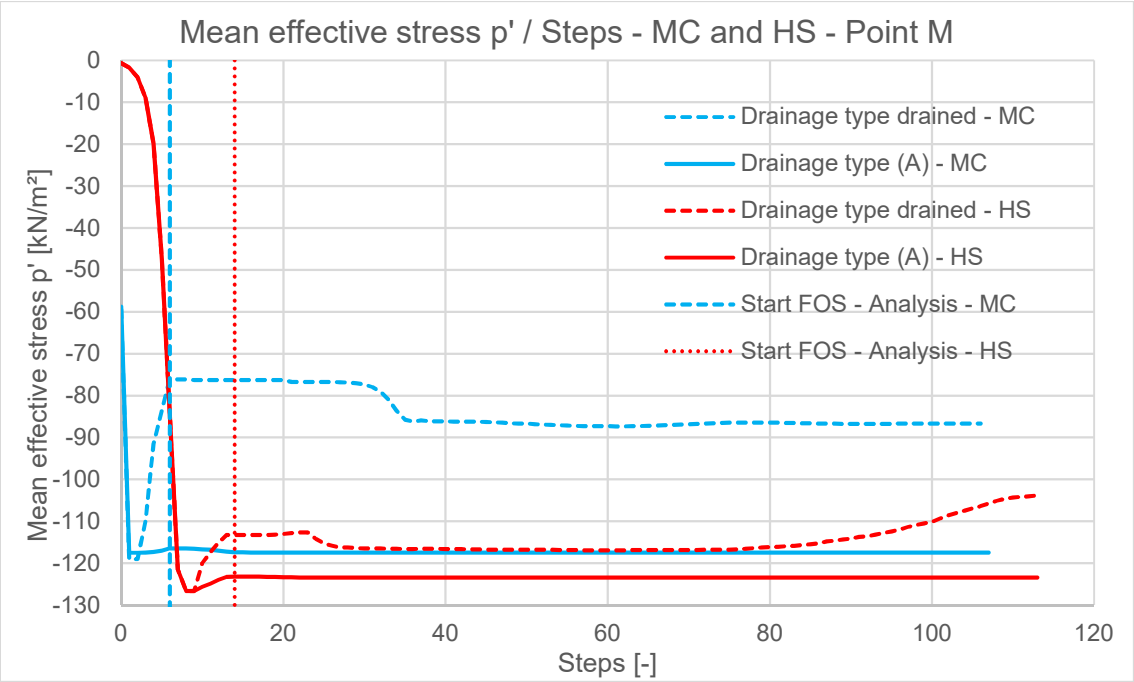

Figure 7 Comparison of effective stresses – Drained vs Undrained (A)

2.3.4 Undrained (A) vs Undrained (B), (C)

The drainage type Undrained (A) produces slightly higher values (FoS = 2.29 – 2.4) than the drainage types (B) and (C) (FoS = 2.24), in case of an undrained analysis and no groundwater table.

The results can be explained by differences in the FoS-calculation or, from another point of view, can be seen as a geometrical problem, as demonstrated in the following theoretical example (Figure 8).

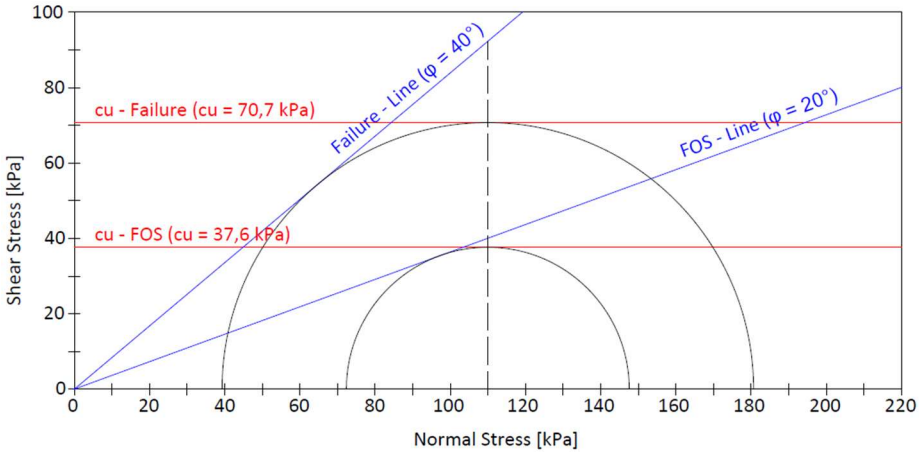

Figure 8 Geometric relationship strength - reduction method (undrained)

$$FoS = \frac{\tan\varphi}{\tan\varphi_{reduced}} = \frac{\tan 40}{\tan 20} = 2.30 \quad (6)$$

$$FoS = \frac{c_u}{c_{u,reduced}} = \frac{70{,}7}{37{,}6} = 1.88 \quad (7)$$

c_u	[kPa]	Undrained shear strength
φ	[°]	Friction angle
FoS	[-]	Factor of safety

This example shows that in case of a constant mean effective stress p' during the safety analysis, which is the case for an undrained strength reduction method, the FoS calculated by means of $\tan\varphi$ (Undrained (A)) will always give higher values than the FoS calculated by means of c_u (Undrained (B) and (C)).

The difference in the FoS due to the different definition of the failure criterion was also investigated with the presented FE-model of a simple slope. Analyses were performed with Undrained (A): c = 2 kPa, φ = 35 and Undrained (B): c_u = 2.82 kPa, Δc_u = 8.82 kPa. Subsequently, the FoS of both analyses were determined manually by applying a Mohr Coulomb (φ, c) and an undrained (c_u) failure criterion to both types of analyses. Figure 9 shows the Mohr circles after the Excavation and after the FoS-analysis for both drainage types at Point K and M. The produced stress states are nearly the same.

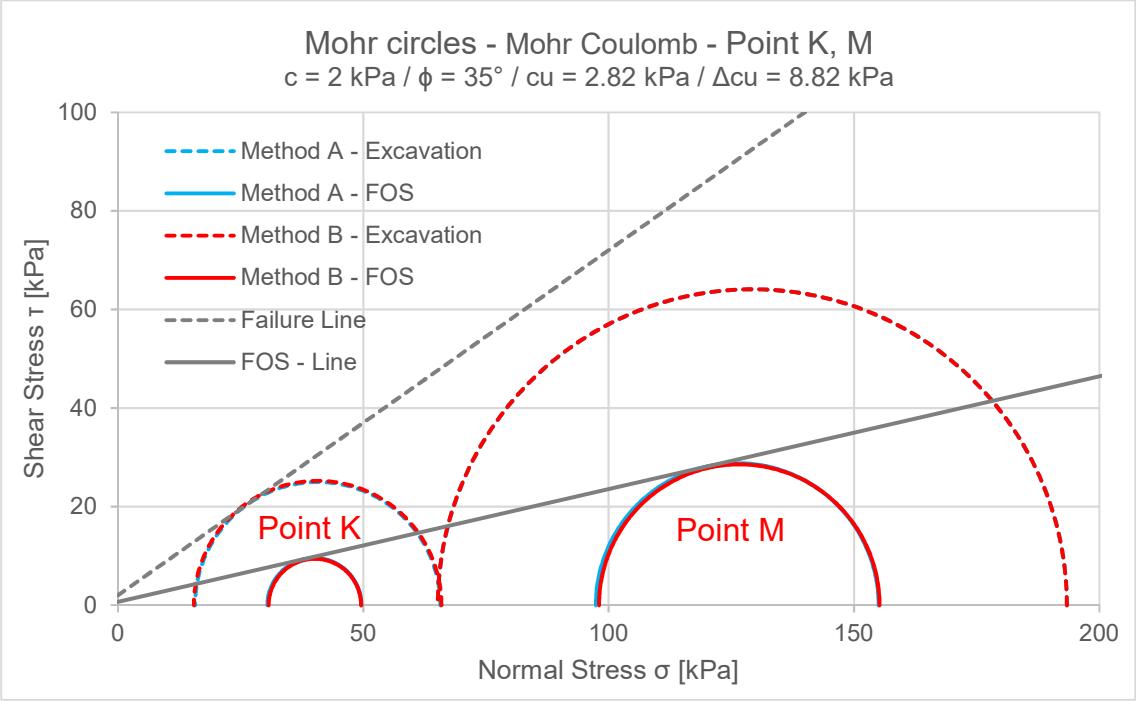

Figure 9 Comparison of Mohr circles for drainage type Undrained (A) and (B)

The calculated FoS are presented in the following:

Undrained (A):

- FoS calculated with φ *and* c = 3.06
- FoS calculated with c_u = 2.66

Undrained (B):

- FoS calculated with φ *and* c = 3.08
- FoS calculated with c_u = 2.68

Both drainage types lead to very similar stress states. Hence, the difference arises from the definition of the failure criteria. This effect certainly becomes less significant if cohesion is more relevant in the definition of the failure criterion of Undrained (A)-analysis, or for smaller mean (effective) stress states. Nevertheless, it is a considerable difference, which also is reflected in the results of this thesis (Table 3).

2.3.5 IUB activated / IUB not activated

This option only makes a difference in the FoS for drainage type Undrained (A) because it is the only drainage type, which is effected by a change of pore pressures. Although drainage type Undrained (B) produces pore pressures, the result of the FOS-Analysis are not effected by them as an undrained failure criterion is applied. For drainage type Undrained (C), the option IUB is not available.

For drainage type (A) IUB activated (drained safety analysis) leads to substantially higher FoS (FoS = 2.58 – 2.8) than IUB not activated (undrained analysis, FoS = 2.29 – 2.4). Plotting the development of excess pore pressures over the calculation steps point out the differences between those options (Figure 10).

IUB is only activated for the safety analysis. Therefore, the results of previous phases remain the same. Comparing drainage type Undrained (A) and Undrained (A) IUB, there seems to be a different behaviour even before IUB is activated. This difference originates from the fact that Point M is slightly shifted horizontally due to a change of the slip surface (Table 2).

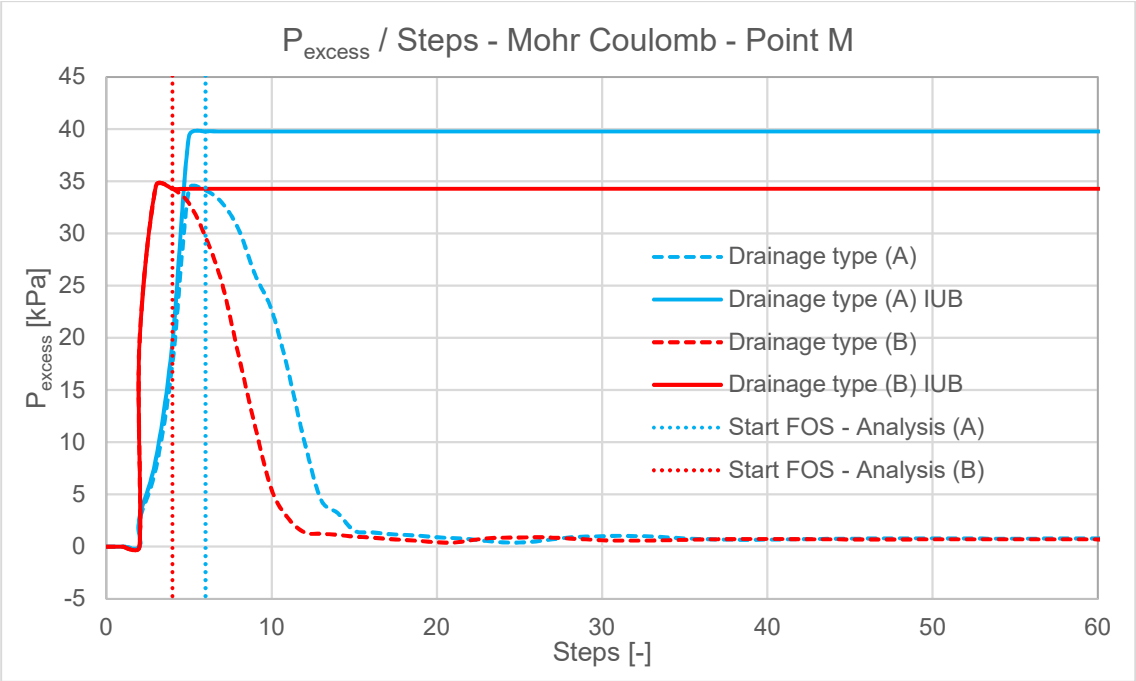

Figure 10 Comparison of pore pressures - IUB activated vs IUB not activated

With activated IUB, the pore pressures are “locked” during the Safety analysis, consequently the positive pore pressures of the previous excavation, sustains over the entire Safety analysis, which leads to a higher FoS. Hence, the generated principal stresses also progress in a different way. The mean effective stresses *p’* are not constant during the safety analysis anymore (Figure 11 for drainage type Undrained (A) and Figure 12 for drainage type Undrained (B)).

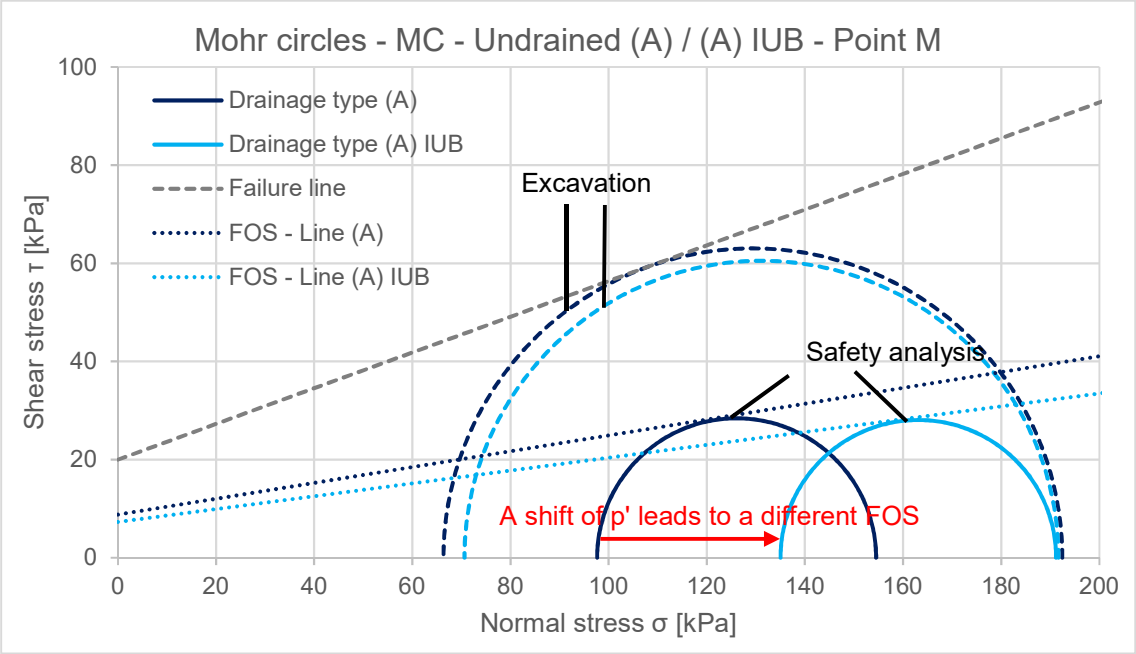

Figure 11 Mohr circles for Undrained (A) / (A) IUB, Mohr Coulomb

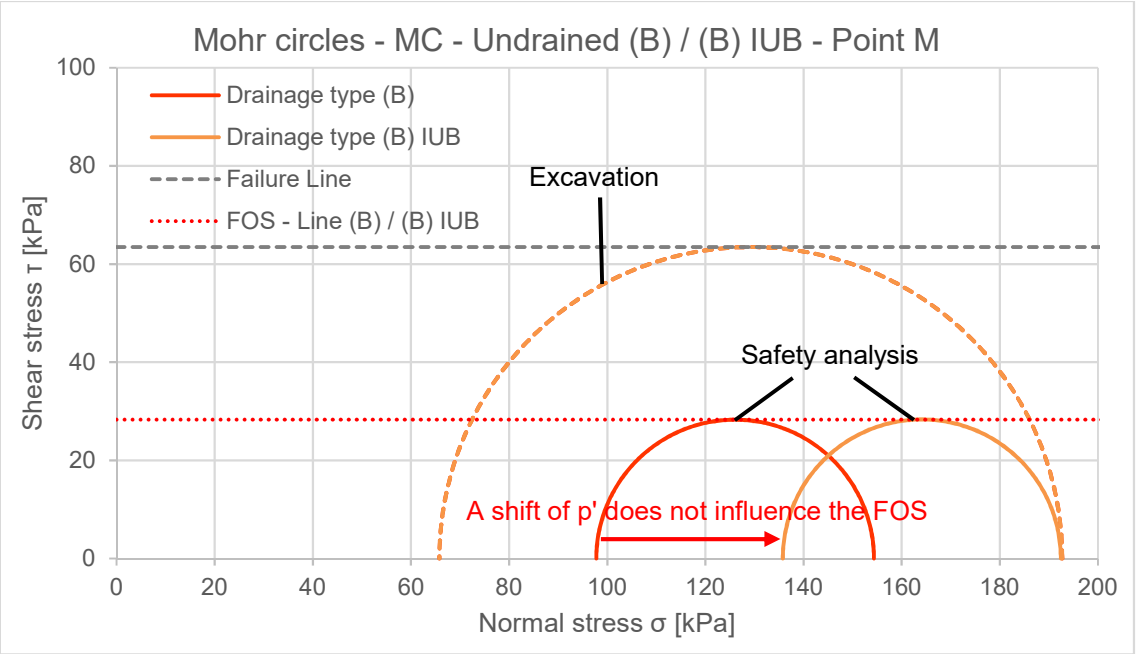

Figure 12 Mohr circles for Undrained (B) / (B) IUB, Mohr Coulomb

To evaluate which pore pressures and thus which FoS is more realistic, simulations with strength parameters divided by the respective calculated FoS were carried out, to "push" the system closer to failure manually. The resulting pore pressures are plotted against the pore pressure results of the previous safety analyses (Figure 10) in Figure 13, for drainage type Undrained (A), and Figure 14 for drainage type Undrained (B).

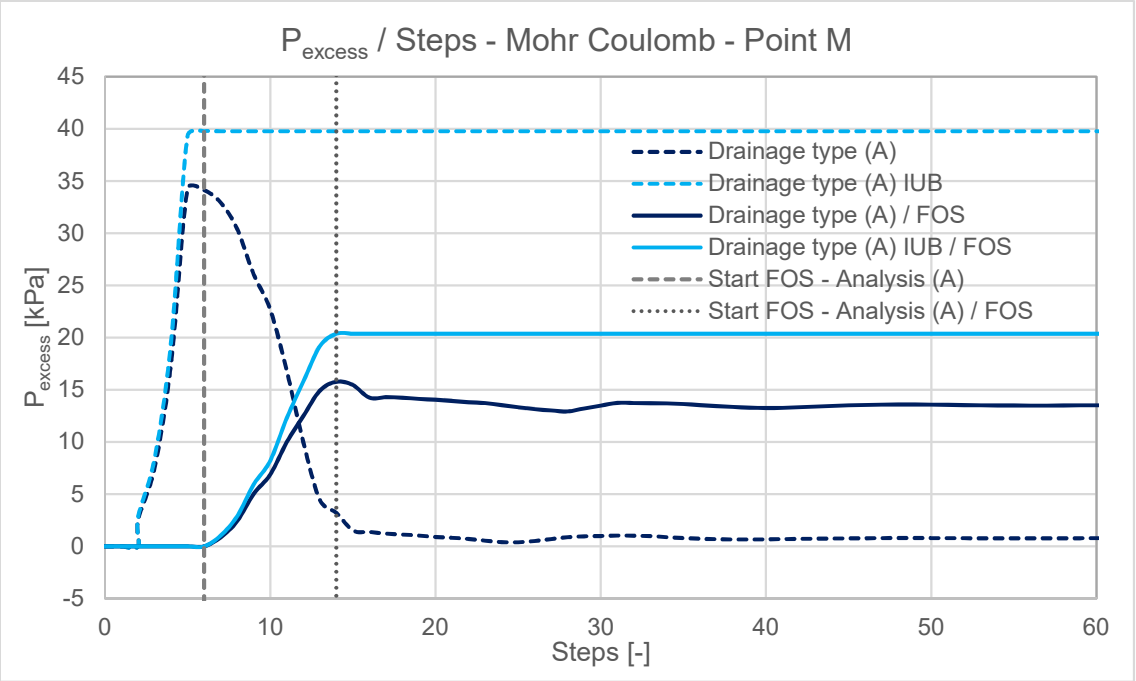

Figure 13 Comparison of pore pressures - Drainage type Undrained (A) / (A) IUB

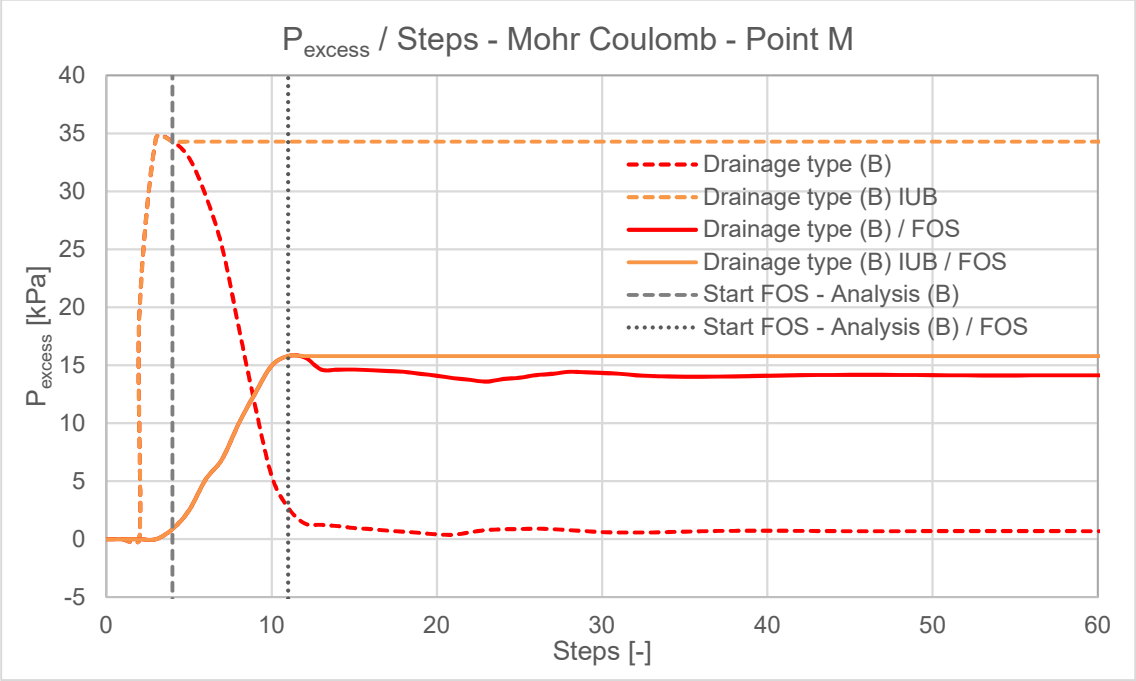

Figure 14 Comparison of pore pressures - Drainage type Undrained (B) / (B) IUB

The pore pressures are hardly comparable therefore, a general recommendation for the settings during a safety analysis cannot be made.

2.3.6 System with / without groundwater table

Considering a groundwater table, changes the pore pressure situation in the model and therefore effective stresses are different. This only effects the FoS-results of drainage type Undrained (A) automatically. The model with a groundwater table results in significantly lower values for the FoS (FoS = 1.47 – 1.48) compared to the model without groundwater table (FOS = 2.29 – 2.4).

This can be explained by the fact that in case of no groundwater table, the simulation starts with pore pressures of zero. In the other case it starts with negative pore pressures, which reduces the effect of the stabilizing, positive excess pore pressures, produced by the excavation (Figure 15 and Figure 16).

As long as the magnitude of the deviatoric stresses q remain the same, the drainage types Undrained (B) and Undrained (C) are unaffected without manual adjustment of c_u. This is reflected in the constant FoS values of 2.24, using a constant undrained shear strength of Δc_u = 5.262 (Table 3). Only if the effective stress σ'_{yy} is adjusted to the "new" groundwater situation (σ'_{yy} = 10 kPa instead of 20 kPa in a depth of 1m, thus Δc_u =

2.631), the drainage types (B) and (C) give reasonable results with a FoS = 1.44 (Table 3).

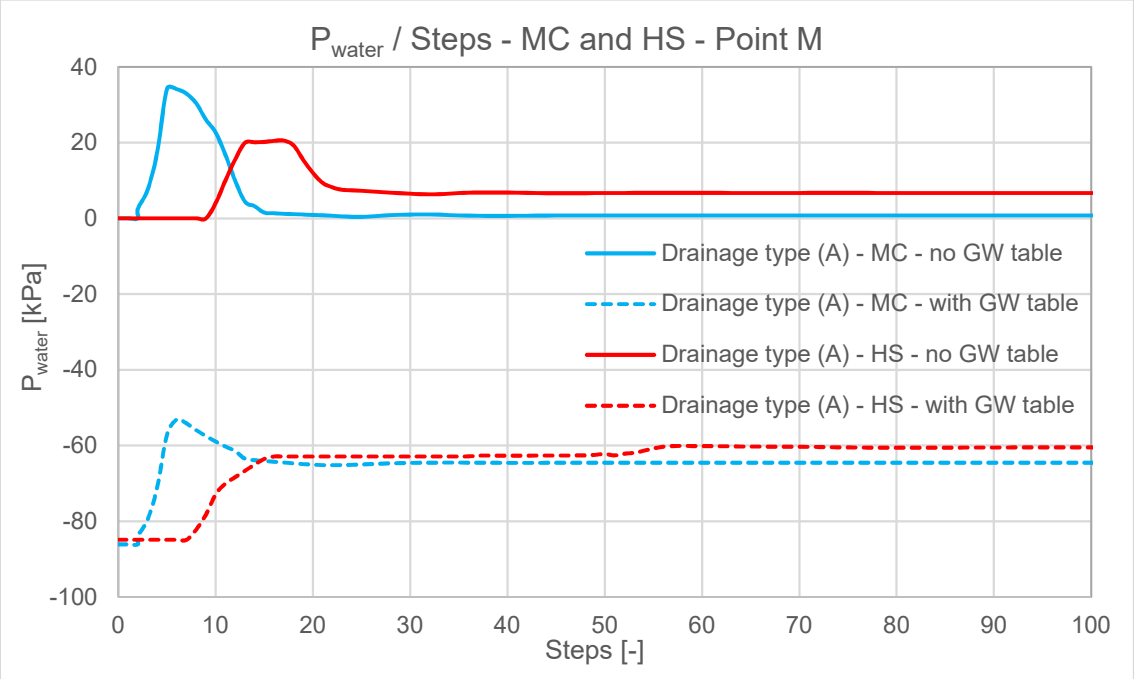

Figure 15 Comparison of pore pressures - with / without GW table

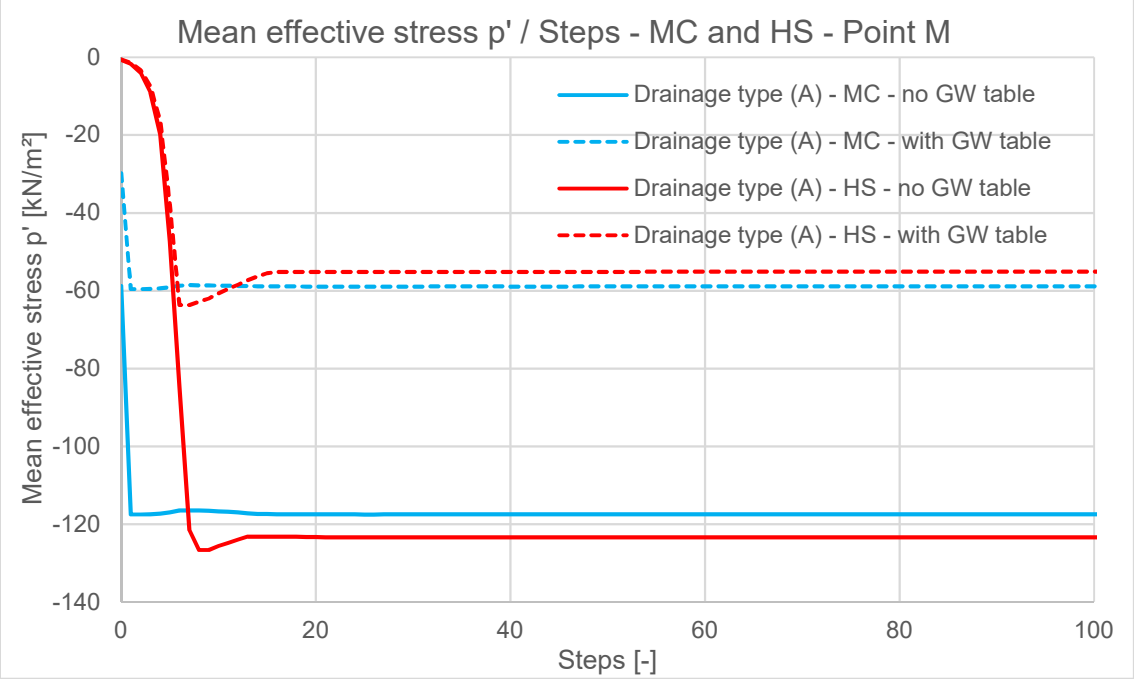

Figure 16 Comparison of pore pressures - with / without GW table

2.4 Conclusion

The undrained shear strength c_u has a large influence on the factor of safety and is defined differently, depending on the applied drainage type. In case of Undrained (A), strength is defined by the effective strength parameters φ', c' and c_u is the outcome of

the constitutive model. However, in case of Undrained (B) and (C), c_u is an input parameter which has to be adopted manually to any change concerning the effective stresses (e.g. change of the pore pressures).

Although Undrained (B) calculates pore pressures, they actually have no influence on the stability of a system. Varying pore pressures are equal to a shift of mean effective stresses, which has no effect applied on an undrained failure criterion. This circumstance could even be deceptive for users, which is why drainage type Undrained (C) is recommended in general, if c_u is used as an input parameter.

With appropriate parameters, similar results can be obtained with all three drainage types. Nevertheless, it has to be considered that two different failure criteria are applied (Undrained (A) → Mohr Coulomb failure criterion, Undrained (B) and (C) → Undrained failure criterion). This could lead to significantly diverging FoS under specific circumstances (low cohesion or high mean effective stress).

Concerning the safety analysis, a general recommendation for the settings (IUB activated → drained analysis, IUB not activated → undrained analysis) cannot be made. It is recommended to reduce the strength parameters stepwise until failure to determine more realistic FoS in case of small models and low calculation times. Otherwise, both types of safety analyses (IUB activated/not activated) should be performed to determine realistic limits for the FoS. .

3 Multilaminate framework

The general intention of the multilaminate framework is based on the concept of relating processes at micro-mechanical scale to the macro-mechanical behaviour of a system. Therefore, it seems to be especially attractive to characterize the behaviour of granular materials like soil. In principle, soils consist of discrete, solid particles that interact with each other. Thus, elastic deformations can be related to the inner structural behaviour of the particles whereas plastic deformation is associated with the inter-particle movement. Apparently, numerical analysis which contain a large number of discrete particles are not feasible, which lead to a simplified formulation of the micro-macro relationship, namely the multilaminate framework. (Galavi 2007), (Schädlich 2012)

3.1 Concept of multilaminate models

To overcome the numerical limitations concerning the analysis of a large number of discrete particles, the multilaminate framework considers a continuum with an infinite number of potential sliding planes at each integration point, instead of modelling individual particles. The potential sliding planes are randomly orientated in space and vary in their orientation. Elastic deformations are generated by the continuum, while plastic deformations are obtained by the movement or sliding along these planes. Modelling an infinite number of planes is certainly not feasible, for which reason a predefined number of so-called sampling or integration planes is introduced. In this study, these planes are called “integration planes”. The integration planes have a predefined orientation for the reason that each of them represents a sector of a virtual unit sphere around the stress point. A weighting coefficient is then applied according to the proportion of its sector, regarding to the volume of the unit sphere. Yield and plastic potential functions are defined on each integration plane separately. Therefore, plastic strains develop independently on the planes and without additional parameters induced anisotropy can be taken into account. By varying the model parameters over the sampling planes, which results in obtaining different strength in different directions, inherent anisotropy can also be introduced. (Galavi 2007), (Schädlich 2012)

3.2 Mathematical formulations

Multilaminate constitutive models are based on the concept that the macroscopic strain associated to a global stress increment is obtained by the summation of the local strains over the integration planes. The local strains are calculated corresponding to the local constitutive model (Figure 17). (Galavi 2007), (Schädlich 2012)

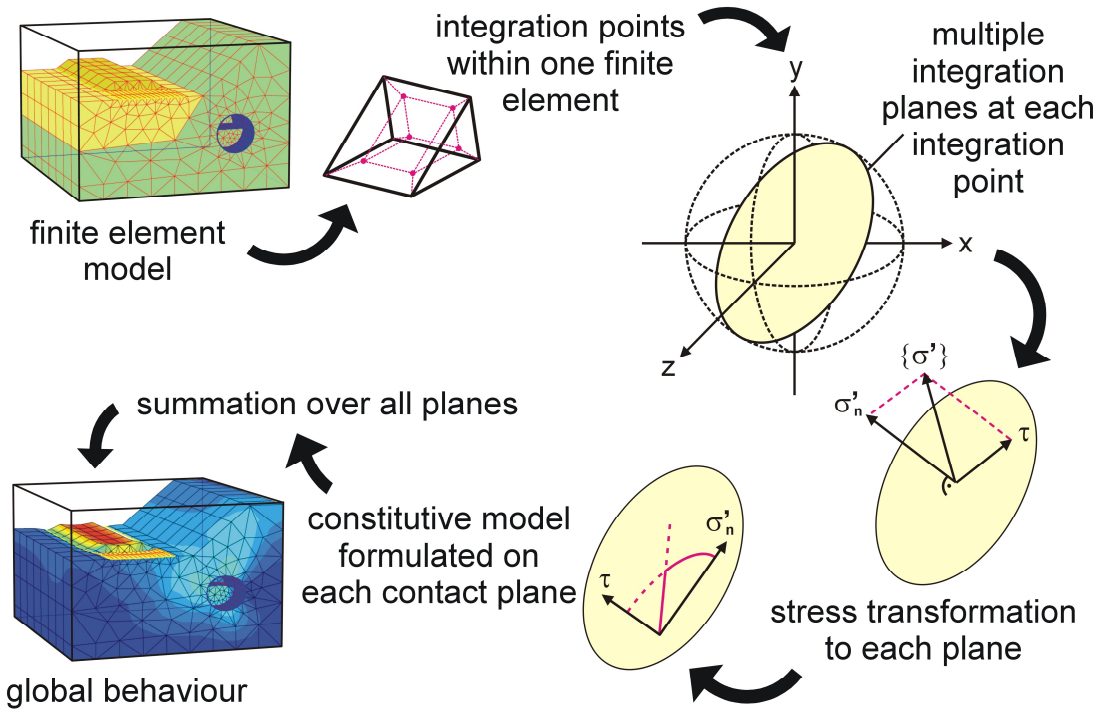

Figure 17 General concept of multilaminate models, (Wiltafsky 2003)

An integration plane i is defined by its normal vector n_i, whose orientation is given by α_i and β_i (Figure 18). Furthermore the local unit vectors s_i and t_i are introduced, which define the direction of the local stresses and strains (Figure 19). (Galavi 2007), (Schädlich 2012)

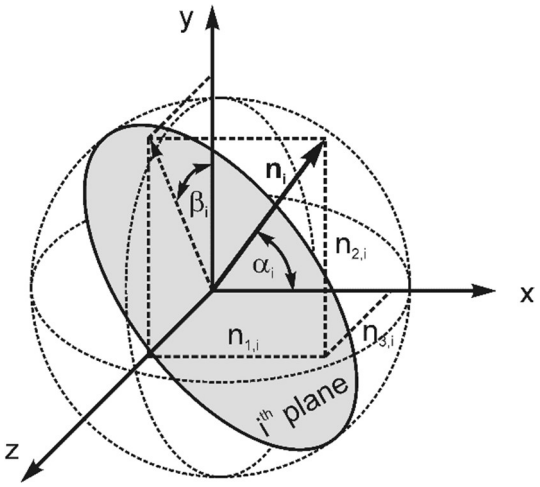

Figure 18 Integration plane orientation, (Schädlich 2012)

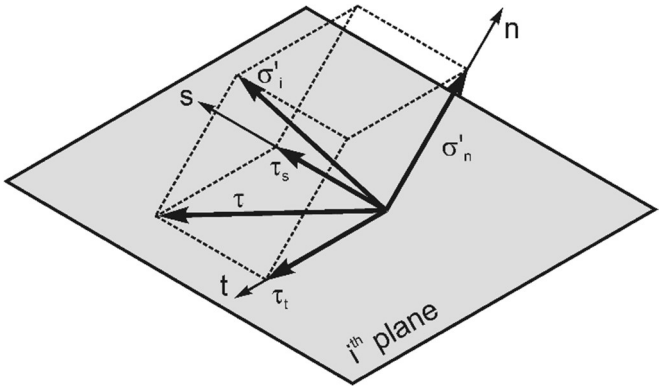

Figure 19 Local stress components, (Schädlich 2012)

The global stress increment $d\sigma'$ is projected on the integration plane i with the transformation matrix T_i. Hence, the local stress increment $d\sigma_i'$ contains the derivatives of the local stress units with regard to the global axes. (Galavi 2007), (Schädlich 2012)

$$d\sigma_i' = (T_i)^T \cdot d\sigma' = (d\sigma_n' \; d\tau_s \; d\tau_t)^T \quad (8)$$

$$T_i = \frac{\partial \sigma_i'}{\partial \sigma'} \quad (9)$$

$d\sigma_n'$	[kPa]	Local effective normal stress increment on integration plane
$d\tau_{s\ or\ t}$	[kPa]	Local shear stress increments on integration plane

Considering an elasto-plastic constitutive model, an elastic strain increment $d\varepsilon_i^e$ and a plastic strain increment $d\varepsilon_i^p$ are calculated to obtain the local strain increment $d\varepsilon_i$.

$$d\varepsilon_i = d\varepsilon_i^e + d\varepsilon_i^p = (d\varepsilon_n \; d\gamma_s \; d\gamma_t)^T \quad (10)$$

$$d\varepsilon_i^e = C_i + d\sigma_i' = (d\varepsilon_n^e \; d\gamma_s^e \; d\gamma_t^e)^T \quad (11)$$

$$d\varepsilon_i^p = d\Lambda_i \cdot \frac{\partial g_i}{\partial \sigma_i'} = \left(d\varepsilon_n^p \; d\gamma_s^p \; d\gamma_t^p\right)^T \quad (12)$$

$d\varepsilon_n$	[-]	Local normal strain increment on integration plane
$d\gamma_{s\ or\ t}$	[-]	Local shear strain increments on integration plane
$d\Lambda_i$	[-]	Increment of the local plastic multiplier
g_i	[-]	Plastic potential function
C_i	[-]	Local compliance matrix

To subsequently obtain the global strain increment $d\varepsilon$, the local strain increments from all integration planes have to be weighted, transformed again and summarized.

$$d\varepsilon = \left(d\varepsilon_{xx} \; d\varepsilon_{yy} \; d\varepsilon_{zz} \; d\gamma_{xy} \; d\gamma_{yz} \; d\gamma_{xz}\right)^T \approx 3 \cdot \sum_{i=1}^{n_{SP}} (T_i \cdot d\varepsilon_i \cdot w_i) \quad (13)$$

$$w_i = \frac{A_i}{A_{sphere}} \quad (14)$$

n_{SP}	[-]	Number of integration planes
w_i	[-]	Weight coefficient for plane i
$d\varepsilon_{xx}$	[-]	Global normal strain increment
$d\gamma_{xy}$	[-]	Global shear strain increment

The weight factors w_i depend on the number of planes and their distribution. Although a higher number of planes essentially leads to more accurate results, the required computational effort limits that number. According to (Wiltafsky, 2003), calculations based on 2x33 symmetric integration planes (n_{SP} = 33 as input parameter) are a good

balance between accuracy and effort. This approach also was applied in this thesis if not declared differently. (Galavi 2007), (Schädlich 2012)

4 Multilaminate models for soils

Two multilaminate constitutive models for soils will be discussed in the following chapters, namely the “Basic model” and the “Advanced model” or “Hvorslev model” as it is called in this thesis. The Basic model refers to the model proposed by Wiltafsky (2003) which was modified by Scharinger (2007) and Galavi (2007). Scharinger (2007) incorporated small strains stiffness; Galavi (2007) incorporated inherent anisotropy, destructuration and a linear strain softening formulation. The Hvorslev model introduced by Schädlich (2012), extends the Basic model by incorporating cross-anisotropic stiffness in the small strain range and by defining a Hvorslev failure surface with subsequent strain softening. In this thesis, the emphasis is put on the strain softening formulations / behaviour of both models. (Galavi 2007), (Schädlich 2012)

Both models are elasto-plastic models acting on the level of one integration plane. Hence, instead of describing a global yield surface, yield surfaces on each plane are described in the following.

4.1 Basic model

According to Schweiger et al. (2009), the Basic model predicts the behaviour of loose to medium dense sand or normally to slightly overconsolidated clays with good accuracy. To activate the Basic model in the current version of the multilaminate soil model the input parameter *switch*$_{HV}$ has to be set to 0. (Galavi 2007)

- *switch*$_{HV}$ = 0 → Basic model

4.1.1 Yield criteria

The yield criterion of the Basic model separates the elastic region from the plastic region. It consist of three separate yield functions, namely f_t (= tension yield function), f_d (= deviatoric yield function) and f_v (= volumetric yield function). Each one is a function of effective normal stress σ_n', shear stress τ and the hardening / softening rules. Figure 20 shows the yield criterion with the three independent yield functions respectively. (Galavi 2007)

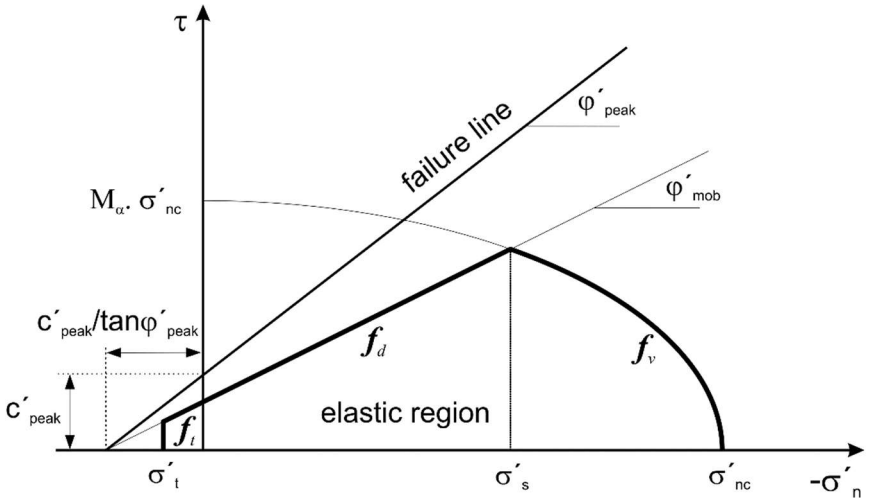

Figure 20 Yield and failure criterion on an integration plane, (Galavi 2007)

Each yield function is valid for a different range of normal effective stress σ_n':

For $\sigma_n' = \sigma_t'$, the tension yield function f_t is considered:

$$f_t = \sigma_n' - \sigma_t' = 0 \quad (15)$$

$$\sigma_t' = c_{peak}'/tan\varphi_{peak}' \quad (16)$$

σ_t'	[kPa]	Tensile strength
c_{peak}'	[kPa]	Effective cohesion at peak strength
φ_{peak}'	[°]	Effective friction angle at peak strength

For $\sigma_t' \geq \sigma_n' \geq \sigma_s'$, the deviatoric yield function f_d is considered:

$$f_d = \tau + \sigma_n' \cdot tan\varphi_{mob}' - \frac{c_{mob}' \cdot tan\varphi_{mob}'}{tan\varphi_{peak}'} = 0 \quad (17)$$

σ_s'	[kPa]	Effective normal stress at the intersection point f_d - f_v
τ	[kPa]	Shear stress on integration plane
c_{mob}'	[°]	Mobilised cohesion
φ_{mob}'	[-]	Mobilised friction angle

For $\sigma_s' > \sigma_n'$, the volumetric yield function f_v is considered:

$$f_v = \frac{\sigma_n'^2}{\sigma_{nc}'^2} + \frac{\tau^2}{(M_\alpha \cdot \sigma_{nc}')^2} - 1 = 0 \quad (18)$$

σ_{nc}'	[kPa]	Effective normal preconsolidation stress of structured soil on integration plane

M_α	[-]	Shape factor determining the shape of the vol. yield curve

4.1.2 Strain hardening

In the Basic model, the deviatoric and volumetric parts of the yield criterion harden independently (Figure 21, Figure 22).

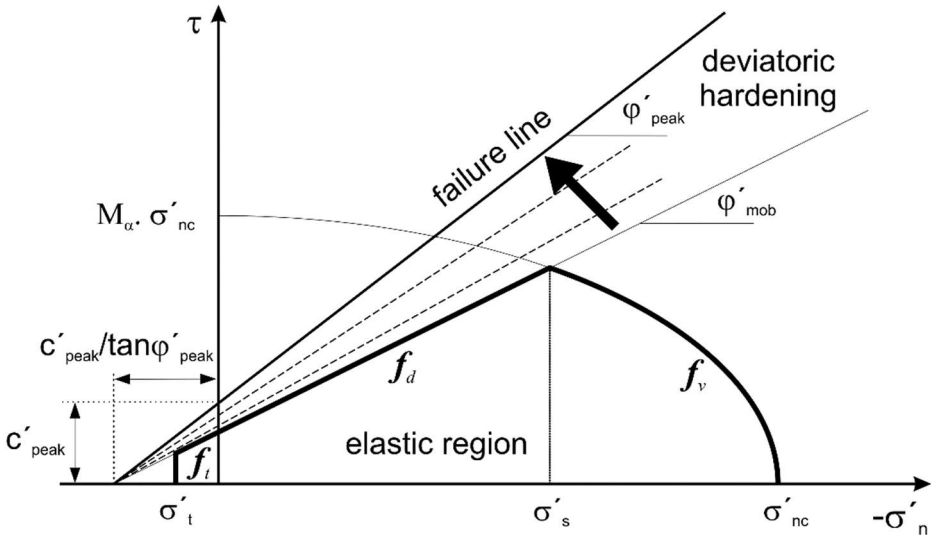

Figure 21 Deviatoric hardening, (Galavi 2007)

Deviatoric hardening rule (straight line), according to Schädlich, 2012:

$$tan\varphi'_{mob} = tan\varphi'_i + (tan\varphi'_{mod} - tan\varphi'_i) \cdot \frac{\varepsilon^p_{\gamma,d}}{\varepsilon^p_{\gamma,d} + \frac{A_{mat}}{3}} = 0 \qquad (19)$$

φ'_i	[°]	Mobilised friction angle related to the initial stress state
φ'_{mod}	[°]	Modified friction angle
$\varepsilon^p_{\gamma,d}$	[-]	Plastic shear strain from the deviatoric yield curve
A_{mat}	[-]	Parameter controlling the rate of deviatoric hardening

With increasing plastic deviatoric strain $\varepsilon^p_{\gamma,d}$, the mobilised friction angle φ'_{mob} increases until the peak friction angle φ'_{peak} is reached. The parameter A_{mat} controls the rate of the deviatoric hardening and can be calibrated against triaxial test data. Large values of A_{mat} lead to a slower mobilization of the friction angle which results in higher plastic shear strains. (Galavi 2007)

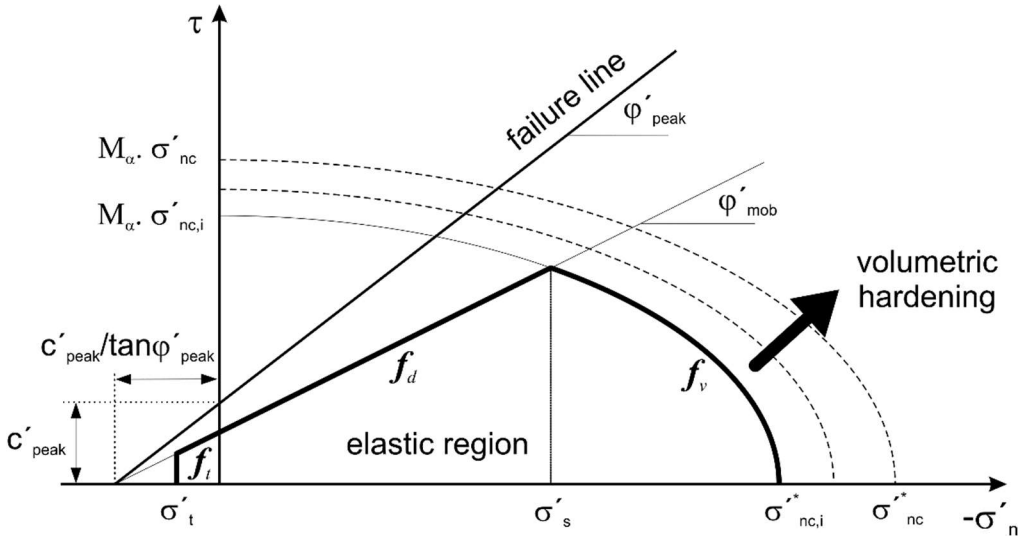

Figure 22 Volumetric hardening, (Galavi 2007)

Volumetric hardening rule (elliptical curve), according to Schädlich, 2012:

$$\sigma_{nc}^{\prime *} = \left[\left(-\sigma_{nc,i}^{\prime *} \right)^{1-m} + K \cdot \frac{(m-1)}{p_{ref}^{m-1}} \cdot \Delta\varepsilon_{n,v}^{p} \right] \quad (20)$$

$$\mathrm{K} = \frac{3}{p_{ref} \cdot \left[\frac{1}{E_{oed,ref}} + \frac{3 \cdot (1-2\nu')}{E_{ur,ref}} \right]} \quad (21)$$

$\sigma_{nc}^{\prime *}$	[kPa]	Effective normal preconsolidation stress of reconstituted soil on integration plane
$\sigma_{nc,i}^{\prime *}$	[kPa]	Initial effective normal preconsolidation stress state of reconstituted soil on integration plane
m	[-]	Power index, controlling stress dependency of stiffness
K	[-]	Hardening parameter
p_{ref}	[-]	Reference stress
$\Delta\varepsilon_{n,v}^{p}$	[-]	Plastic normal strain increment from the volumetric yield curve
$E_{oed,ref}$	[-]	Reference stiffness for primary oedometer loading
$E_{ur,ref}$	[-]	Stiffness for un- and reloading at reference stress

With increasing plastic normal strain $\varepsilon_{n,v}^{p}$, the elliptical curve expands, with K defined as the volumetric hardening parameter. There is no predefined limit for volumetric hardening. (Galavi 2007)

4.1.3 Strain softening

Full mobilisation of shear strength is reached when $\varphi'_{mob} = \varphi'_{peak}$, $c'_{mob} = c'_{peak}$ and the corresponding local damage strain $\varepsilon_{di} = \varepsilon_{di,peak}$. The damage strain is a function of the

summation of all absolute values of plastic strains (normal and shear strains), obtained by all parts of the yield curve. (Galavi 2007)

$$\varepsilon_{di} = (1 - A_d)\, \varepsilon^p_{n,i} + A_d\, \varepsilon^p_{\gamma,i} \quad (22)$$

$$\varepsilon^p_{n,i} = \left|\varepsilon^p_{n,d}\right| + \left|\varepsilon^p_{n,v}\right| + \left|\varepsilon^p_{n,t}\right| \quad (23)$$

$$\varepsilon^p_{\gamma,i} = \left|\varepsilon^p_{\gamma,d}\right| + \left|\varepsilon^p_{\gamma,v}\right| + \left|\varepsilon^p_{\gamma,t}\right| \quad (24)$$

$\varepsilon^p_{n,i}$	[-]	Summation of all absolute values of plastic normal strains
$\varepsilon^p_{\gamma,i}$	[-]	Summation of all absolute values of plastic shear strains
A_d	[-]	Scaling parameter to control the relative proportion of distortional and volumetric degradation
φ'_{mob}	[-]	Mobilised friction angle

Any further increase of ε_{di} leads to a decrease of φ' and c' until they reach their predefined residual values φ'_{res} and c'_{res} (Figure 23).

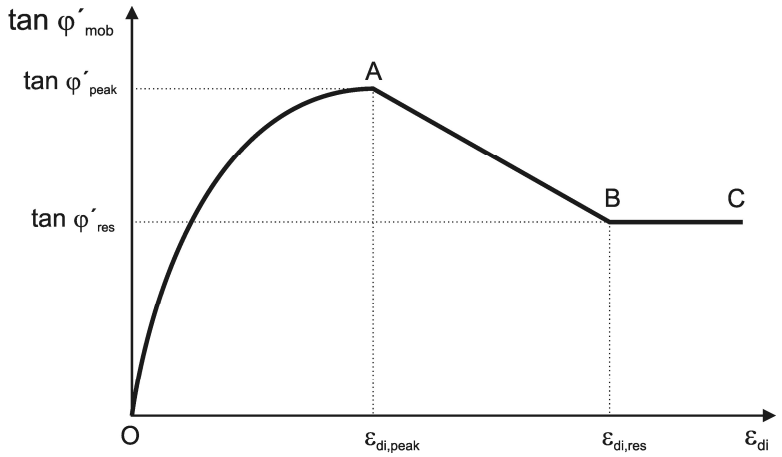

Figure 23 Linear strain softening in relation to the damage strain, (Galavi 2007)

The rate of strength reduction is defined by two linear strain softening rules, the friction softening rate $m_{soft,\varphi}$ and the cohesion softening rate $m_{soft,c}$. Both are acting independently, thus leading to three different softening scenarios (Figure 24). Experimental data shows that the cohesion softening rate is usually higher than the friction softening rate. (Galavi 2007)

$$tan\varphi'_{mob} = -m_{soft,\varphi}\left(\varepsilon_{di} - \varepsilon_{di,peak}\right) + tan\varphi'_{peak} \quad (25)$$

$$c'_{mob} = -m_{soft,c}\left(\varepsilon_{di} - \varepsilon_{di,peak}\right) + c'_{peak} \quad (26)$$

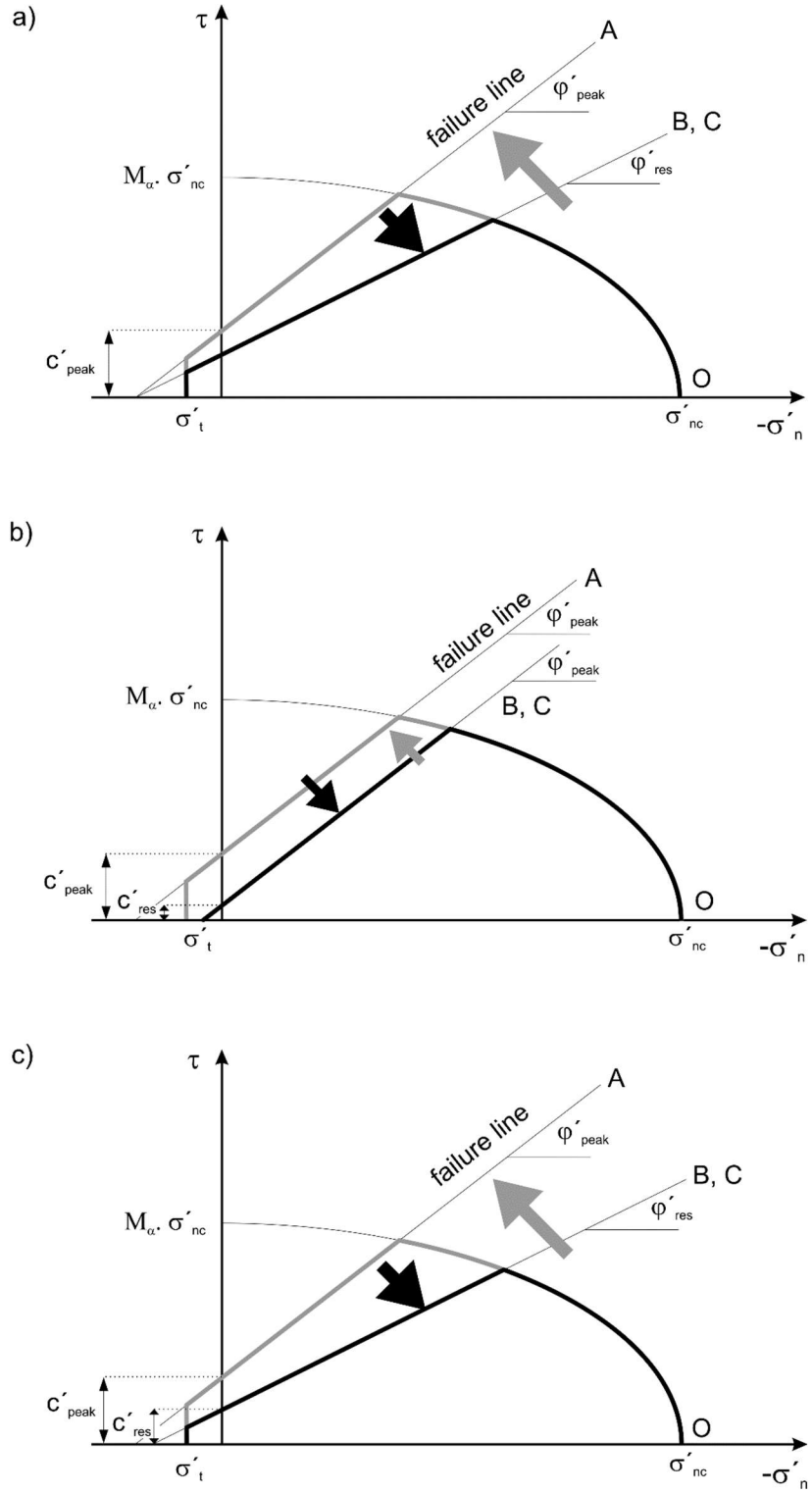

Figure 24 a) Friction softening, b) Cohesion softening, c) Friction and cohesion softening, (Galavi 2007)

4.2 Hvorslev model

The Hvorslev model modified the Basic model in order to enable predictions of heavily overconsolidated clay and dense sand (Schädlich 2012) To activate the Hvorslev model, the input parameter $switch_{HV}$ has to be set to 1 or 2.

- *switch$_{HV}$* = 1 → Hvorslev model with regularization
- *switch$_{HV}$* = 2 → Hvorslev model no regularization

4.2.1 Hvorslev surface and strain softening

Additional to the yield surfaces of the Basic model, a strength boundary surface is introduced on integration plane level, namely the Hvorslev yield surface f_{HV} (Figure 26). First proposed by Hvorslev (1937), the surface describes the peak shear strength of heavily overconsolidated soils at various initial volumes. By normalization of stresses according to the vertical pressure σ'_{ve} at the current void ratio at the normal consolidation line, a linear relationship is obtained (Figure 25). Hence, the cohesion $c' = c'_{ve} \cdot \sigma'_{ve}$ and is no longer a true material constant but depends on σ'_{ve}. (Schädlich 2012)

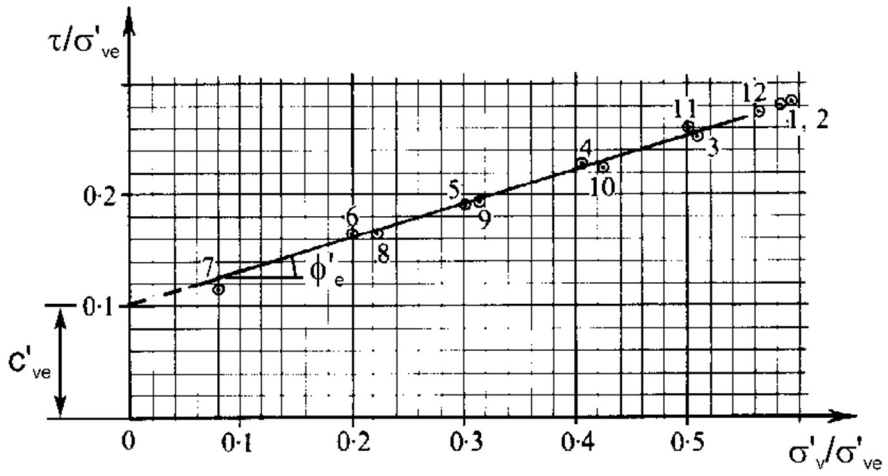

Figure 25 Failure of Wiener Tegel, (Schädlich 2012)

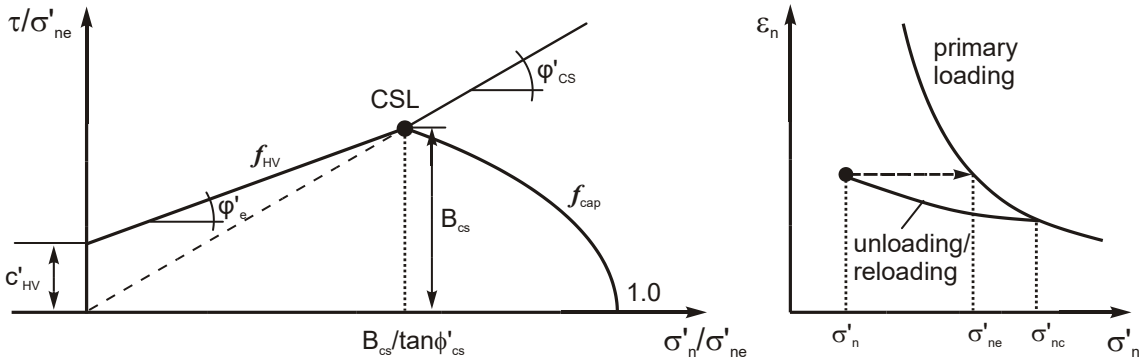

Figure 26 Normalized yield surface on integration plane level, (Schädlich 2012)

Therefore, on integration plane level, c'_{HV} is not an independent input parameter but is determined by the intercepting point of the cap yield surface f_{cap} with the critical state failure line and the Hvorslev surface inclination φ'_e. (Schädlich 2012)

The local Hvorslev surface is defined by:

$$f_{HV} = \tau + \sigma'_n \cdot tan\varphi'_e + c'_{HV} \cdot \sigma'_{ne} \quad (27)$$

$$c'_{HV} = B_{CS} \cdot \left(1 - \frac{tan\varphi'_e}{tan\varphi'_{CS}}\right) \quad (28)$$

c'_{HV}	[-]	Cohesion intercept of the Hvorslev surface, normalised with σ'_{ne}
σ'_{ne}	[kPa]	Equivalent normal stress on local normal consolidation line
B_{CS}	[-]	Supplementary parameter to define the position of the critical state line
φ'_{CS}	[°]	Effective friction angle at critical state
φ'_e	[°]	Inclination of the Hvorslev surface

An input of distinctive peak strength values is not required anymore. The Hvorslev surface serves as a peak strength boundary surface which gets activated once the stress path reaches that surface. Before activation, plastic strains are obtained from the strain hardening deviatoric yield surface. Any further increase of strain, after activating the Hvorslev surface leads to strain softening. The position of the Hvorslev surface is linked to the position of the cap yield surface, hence any change of one surface changes the other inevitable. Therefore, the softening rule of the Hvorslev surface is equivalent to the hardening rule of the cap yield surface. (Schädlich 2012)

4.3 Small strain stiffness

Generally the small strain stiffness curve is defined by two parameters, the initial isotropic shear modulus at small strain at reference pressure $G_{0,ref}$ and a reference shear strain γ. In case of multilaminate models, the degradation of small strain stiffness depends on the local deviatoric strain ε_{deg}. Hence, the curve is defined by two deviatoric strain parameters. The onset of the stiffness degradation is defined by $\varepsilon_{deg,1}$, whereas $\varepsilon_{deg,2}$ defines the transition to large strains (Figure 27). Although the degradation between those values is linear on a local scale (Figure 28b), the deviatoric strains vary from plane to plane which results in a rather smooth degradation on a global scale (Figure 28a). (Schädlich 2012)

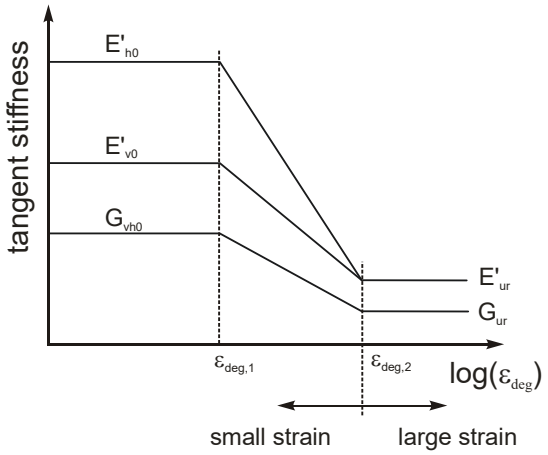

Figure 27 Degradation of small strain stiffness behaviour and transition to large strain behaviour, (Schädlich 2012)

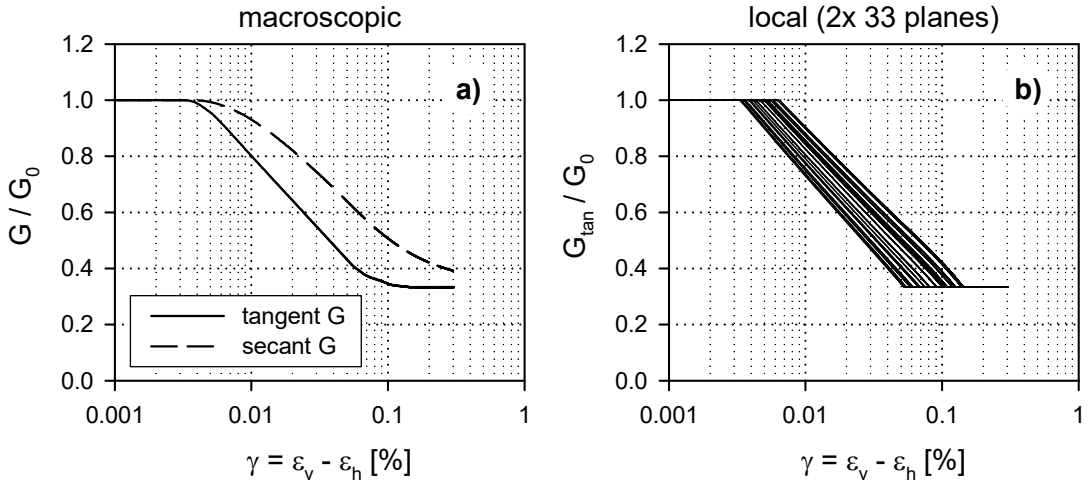

Figure 28 Macroscopic (a) and local (b) degradation of small strain stiffness, (Schädlich 2012)

If small strain stiffness is activated, $\varepsilon_{deg,1}$ and $\varepsilon_{deg,2}$ should be calibrated against existing data, in terms of a comparing the global behaviour (Figure 28a) with the data.

5 Multilaminate models applied to simple triaxial simulations

The principal intention to work with multilaminate constitutive models was mainly due to their ability of simulating strain softening behaviour. The implemented non-local strain softening should help to model the displacement behaviour of a so-called slow moving slope under the influence of groundwater fluctuations. The main aim was, to investigate the possibility to reproduce this kind of continuous movements with strain softening. However, first calculations with a simple slope indicated unexpected and uninterpretable results. Therefore, a number of simple load-controlled, axisymmetric and biaxial simulations are analysed in this chapter. These simulations serve to investigate the general behaviour of the multilaminate constitutive models. At first, studies about the material behaviour before strain softening (chapter 5.2) are analysed. The stress-strain behaviour, the small strain stiffness behaviour and the influence of the maximum load fraction on multilaminate models are discussed respectively. Secondly, studies about the material behaviour with induced strain softening (chapter 5.3) are analysed. The stress-strain behaviour and the determination of softening points for the BMwS and the HM are discussed. At last, the strain softening behaviour due to cyclic loading of a simple biaxial model (chapter 5.3.3) is analysed.

In the course of these studies, a number of application notes are presented, along with an analysis about the determination and development of softening points. It has to be noted that these simulations are not intended to reproduce any specific experimental results.

5.1 Applied constitutive models and material parameters

The following studies were carried out with three different constitutive models, particularly the Basic model, the Hvorslev model and the Hardening Soil Small model as a reference model. Additionally the Basic model is capable of simulating two cases, a simulation with non-local strain softening and one without softening. Hence, for the Basic model, investigations for both types (with and without strain softening) were performed. The different models are denoted as follows:

- Hardening Soil Small model (HSS)
- Basic model with softening (BMwS)
- Basic model no softening (BMnS)
- Hvorslev model (HM)

Attention has to be paid to the different values of the K_0-value in case of BMwS and BMnS. While the BMwS has peak values of c = 3 kPa, φ = 18° and residual values of c = 1 kPa, φ = 12°, the BMnS has just one parameter set for both, peak and residual values with c = 3 kPa, φ = 18°. The fact that the K_0-value has to be calculated according to the residual values in the Basic model leads to two different K_0-values, in particular K_0 = 0.792 for the BMwS and K_0 = 0.691 for the BMnS. As a consequence, the volumetric behaviour of these two models is not comparable in detail. If not specified otherwise, the parameters shown in Table 4 will be used for the following studies.

The softening rates $m_{soft,c}$ and $m_{sof\ ,\varphi}$ are set to the highest values recommended by Galavi, 2007. Hence, maximum softening is obtained for any strain increase after the local damage strain ε_{di} reached $\varepsilon_{di,peak}$ (chapter 4.1.3).

Table 4 Material parameters

Parameter	Basic Model with Softening	Basic Model without Softening	Hvorslev model	Hardening Soil Small	Unit
$E_{50,ref}$ =				18000	[kPa]
$E_{oed,ref}$ =	15000	15000	15000	15000	[kPa]
$E_{ur,ref}$ =	37500	37500	37500	37500	[kPa]
p_{ref} =	100	100	100	100	[kPa]
m =	0.7	0.7	0.7	0.7	[-]
ν_{ur} =	0.2	0.2	0.2	0.2	[-]
A_{mat} =	19	19	19		[10^{-3}]
c'_{peak} =	3	3	0	3	[kPa]
φ'_{peak} =	18	18	18	18	[°]
OCR =	1	1	1		[-]
R_f =	0.95	0.95	0.95	0.95	[-]
K_{0nc} =	0.7921	0.691	0.691	0.691	[-]
n_{CP} =	33	33	33		[-]
$G_{0,ref}$ =	44000*	44000*	44000*	45000	[kPa]
$\gamma_{0.7}$ =				0.0002	[-]
$\varepsilon_{deg,1}$ =	0.000025*	0.000025*	0.000025*		[-]
$\varepsilon_{deg,2}$ =	0.002*	0.002*	0.002*		[-]
φ'_e =	17	17	12		[°]
φ'_{res} =	12	18	18		[°]
c'_{res} =	1	3	0		[kPa]
$m_{soft,\varphi}$ =	0.1	0.1	0		[-]
$m_{soft,c}$ =	5	5	0		[-]
L_{cal} =	0.1	0.1	0.1		[m]
$A_{vol/dev}$ =	1	1	1		[-]
MaxPoint =	500	500	500		[-]
$SSS_{recovery}$ =	1	1	1		[-]
h_{soft} =	0	0	80		[-]

*Fitted in a triaxial compression stress path to gain similar results as the HSS model (see chapter 4.3)

The parameters of the multilaminate model are not discussed in detail in this thesis. A detailed description is given in (Galavi 2007), (Schädlich 2012) and (Schädlich 2014). Furthermore, all models concerning this chapter were calculated drained.

5.2 Axisymmetric / Biaxial simulations without endplates

The numerical axisymmetric / biaxial test simulations reported in this chapter were performed to study the constitutive model behaviour before strain softening starts.

The test specimen is 1m high and 0.25m wide, for both the axisymmetric as well as the biaxial simulation. After the initial phase the simulation consists of four consecutive loading / unloading phases. The horizontal load $q_{horizonta}$ remains at $q_{horizontal}$ = 100 [kPa] during the complete simulation, while the vertical load $q_{vertical}$ starts at $q_{vertical}$ = 100 [kPa] and is increased to $q_{vertical,max}$ ≈ 200 [kPa] in phase 2 and phase 4. Hence a complete unloading reloading cycle can be simulated (Figure 29).

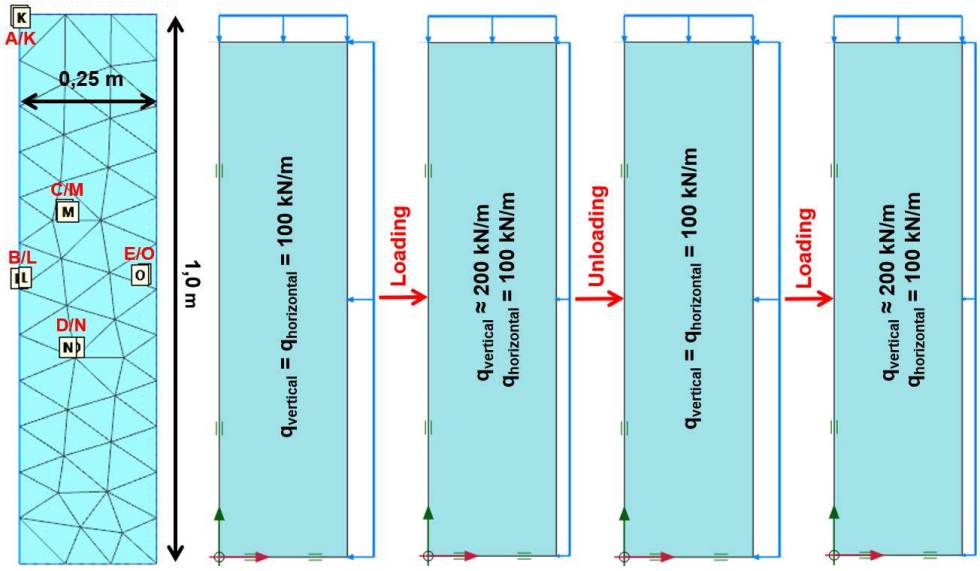

Figure 29 Model geometry and loading / unloading cycle, Number of 15-noded elements: 72

For each constitutive model the vertical load $q_{vertical,max}$ is increased up to 1 kPa below failure load. Hence, $q_{vertical,max}$ slightly differs between the constitutive models. It has to be noted that failure load in this context coincides with failure of the complete model. All values are summarized in Table 5.

Table 5 Summary loading / unloading cycle

	Axisymmetric / Biaxial model without plate							
	Phase 1		Phase 2 (1st loading)		Phase 3 (unloading)		Phase 4 (2nd loading)	
	$q_{vertical}$ [kPa]	$q_{horizontal}$ [kPa]	$q_{vertical,max}$ [kPa]	$q_{horizontal}$ [kPa]	$q_{vertical}$ [kPa]	$q_{horizontal}$ [kPa]	$q_{vertical,max}$ [kPa]	$q_{horizontal}$ [kPa]
HSS	100	100	197	100	100	100	197	100
BMwS / BMnS	100	100	205	100	100	100	205	100

HM	100	100	196	100	100	100	196	100

There are no endplates at the top or the bottom of the specimen, therefore the load is applied directly onto the specimen, which leads to the following conditions:

- Uniform stress level in the hole specimen (Figure 30)
- Uniform strains in the hole specimen (Figure 30)
- No appearance of failure points (Figure 30)
- No appearance of softening points

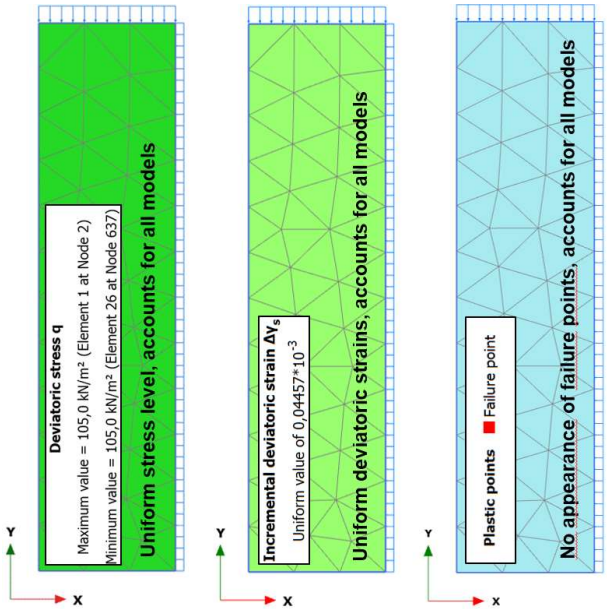

Figure 30 Axisymmetric / Biaxial model - Stresses, Strains and failure points indicate a uniform response

5.2.1 Stress-strain behaviour and Small strain stiffness behaviour

Stress-strain curves of calculations without endplates are shown in Figure 31 for the axisymmetric models as for the biaxial models. Even before strain softening occurs the behaviour of the BMwS is not equal to the behaviour of BMnS. This circumstance can be explained by the difference of the K_0-value, between those versions of the Basic model.

In general, the multilaminate models react much stiffer at the beginning of the first loading phase than the HSS model. Furthermore, the multilaminate models show principally no hysteresis during the unloading / reloading process, which derives from the shear strain-shear modulus behaviour (Figure 34). This will be discussed later on.

The biaxial multilaminate models show a slight curvature at the end of the unloading / beginning of the reloading phase. This behaviour is even more visible in the p'- q - space

as shown in Figure 32. The reason for this behaviour is a rotation of the principal effective stresses σ_1' and σ_2' as exposed in Figure 33. In contrast to the axisymmetric simulations, the "out of plane" cartesian effective stress σ_z' exceeds 100 kPa during the loading cycle and settles between σ_x' and σ_y'. In case of the biaxial HSS-model, σ_z' does not exceed σ_x' at any point. This leads to a stress state analogical to the axisymmetric HSS-simulation, which is also reflected in a similar stress-strain behaviour (Figure 31).

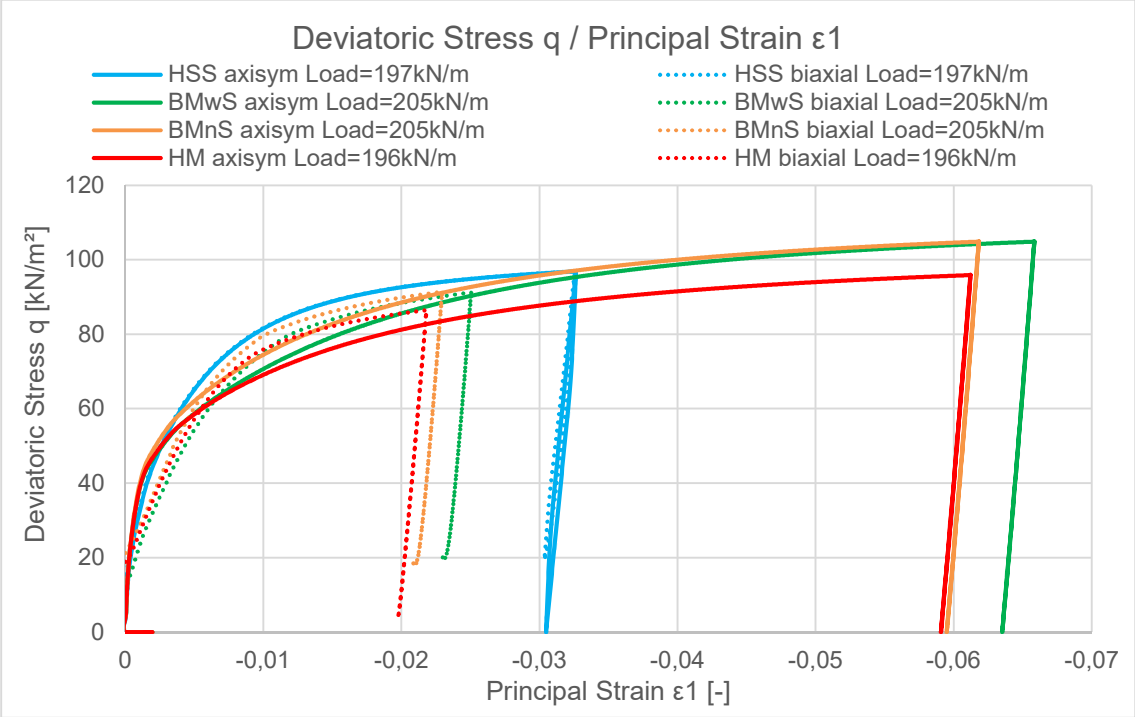

Figure 31 Axisymmetric / Biaxial tests; Stress-strain curves for all models, Phase 2 – Phase 4

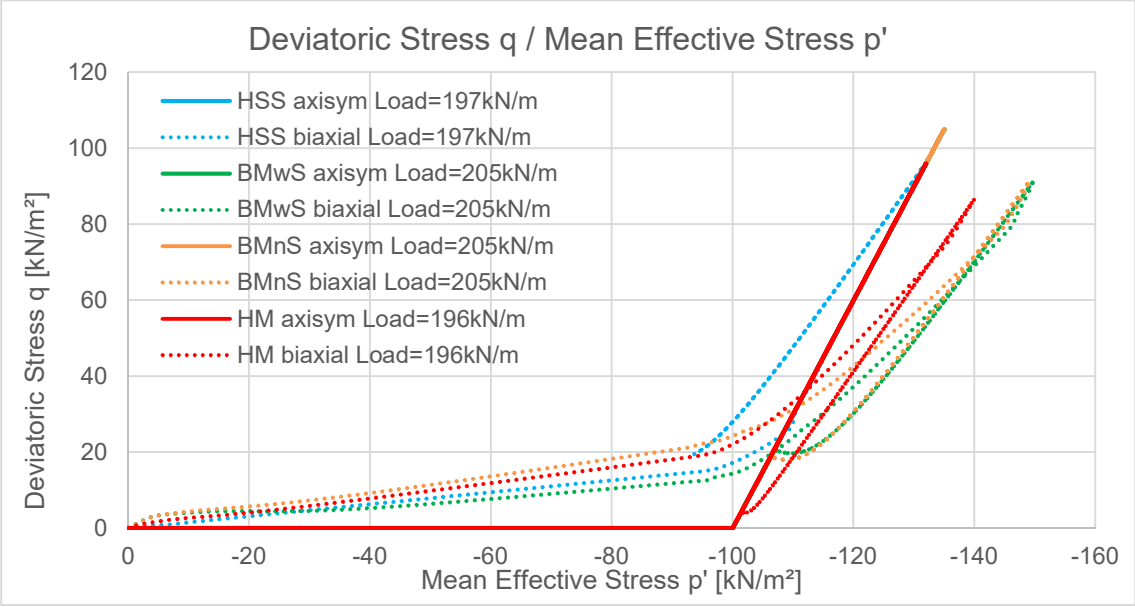

Figure 32 Axisymmetric / Biaxial tests; p'-q curves for all models, Phase 1 – Phase 4

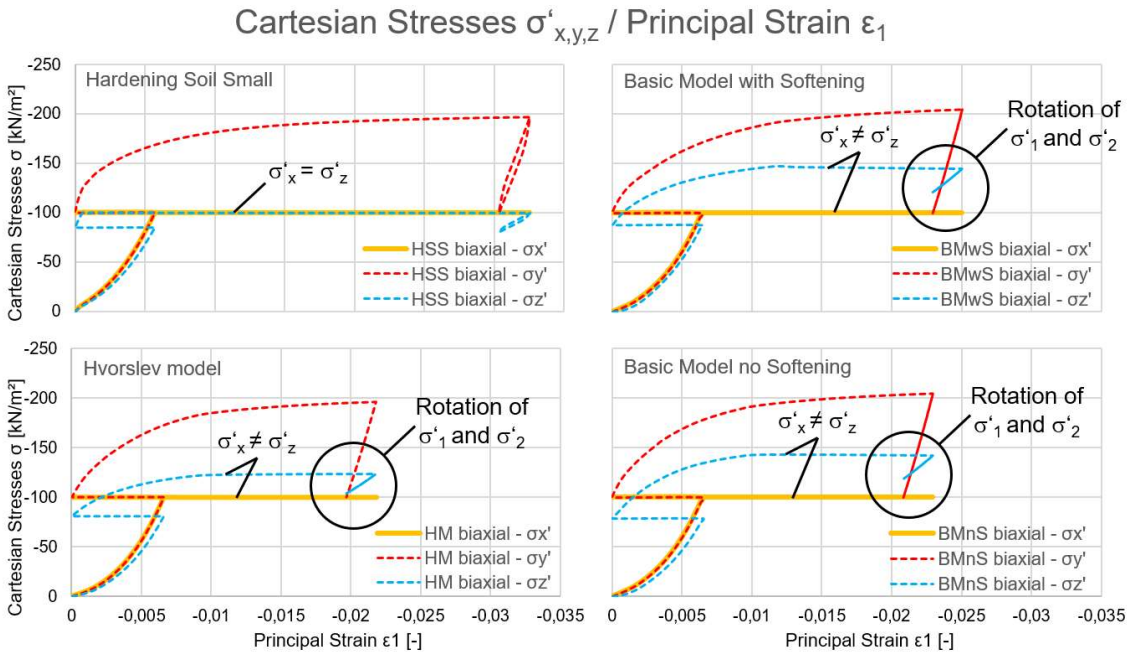

Figure 33 Biaxial Tests; Cartesian stress - strain curves for all models, Phase 1 – Phase 4

Figure 34 displays the shear modulus $G_{tan,ref}$ over shear strains γ_s for all axisymmetric models. In theory, the shear modulus is set to the small strain stiffness, at the beginning of the first loading and after each change in strain direction (e.g. in case of unloading / reloading). Any further increase of strain in the same direction results inevitably in a decreasing shear stiffness until the unloading / reloading stiffness G_{ur} is reached. Considering the before described effects, the HSS model shows an appropriate behaviour. The shear modulus of the multilaminate models increases continuously during the unloading phases and decreases during the reloading phase. This does not reflect the expected behaviour, as described above. However, the small strain stiffness behaviour explains the absence of hysteresis, discussed in Figure 31. The reason for this small strain stiffness behaviour could not be clarified. Nonetheless, it has to be mentioned that the implementation of the small strain stiffness mechanism depends on the constitutive model; especially the modelling of strain history differs significantly between the used constitutive models. Furthermore, the required magnitude of change in the strain direction to reactivate the entire small strain stiffness is defined differently in all models.

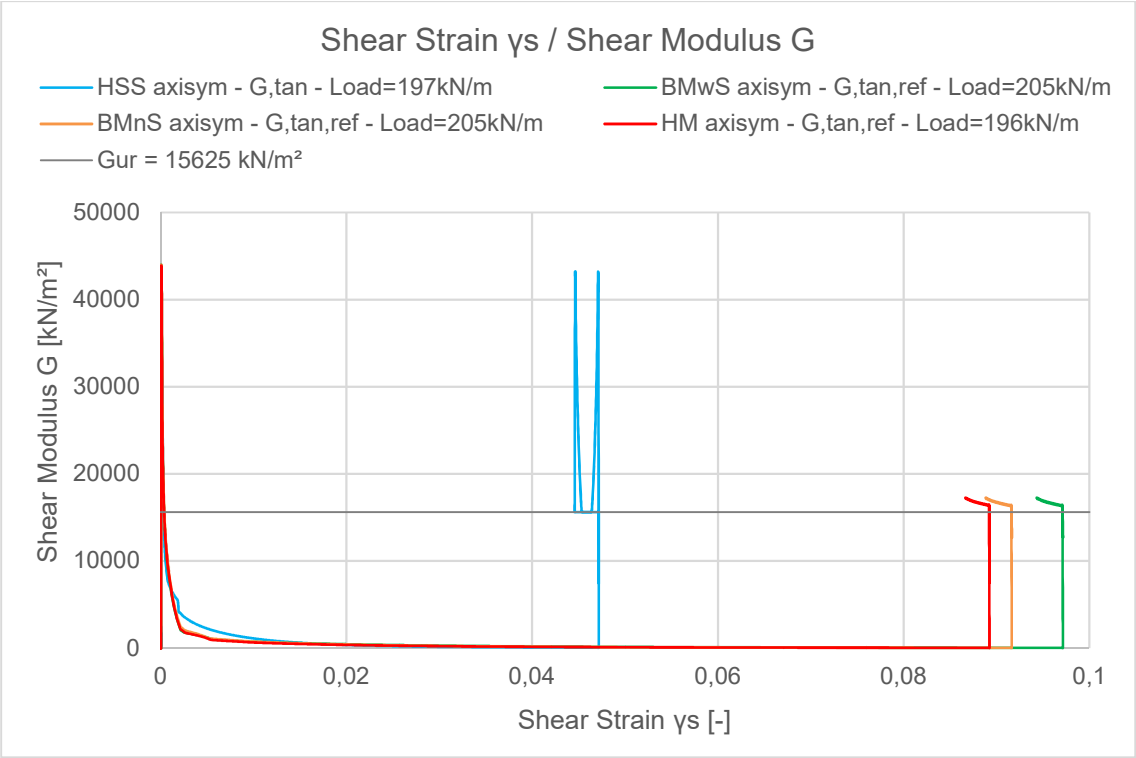

Figure 34 Axisymmetric Tests; Small strain / unloading / reloading stiffness with $q_{vertical,max}$, Phase 1 – Phase 4

However, if the maximum vertical load $q_{vertical,max}$ is decreased by 2 kPa, the BMnS and the HM show an appropriate behaviour concerning the small strain stiffness (Figure 35). Furthermore, a small hysteresis can be recognized in Figure 36. However, the multilaminate models show a stiffer response in the unloading / reloading range, compared to the HSS model. Apparently the behaviour of the BMwS still remains the same, despite any change of the maximum vertical load, as can be seen in Figure 35 for $q_{vertical,max}$ = 203 kPa and Figure 37 for $q_{vertical,max}$ = 190 kPa. Conclusively, can be said that this seems to be a numerical problem, which should be investigated, but finally should not have a significant influence on following results.

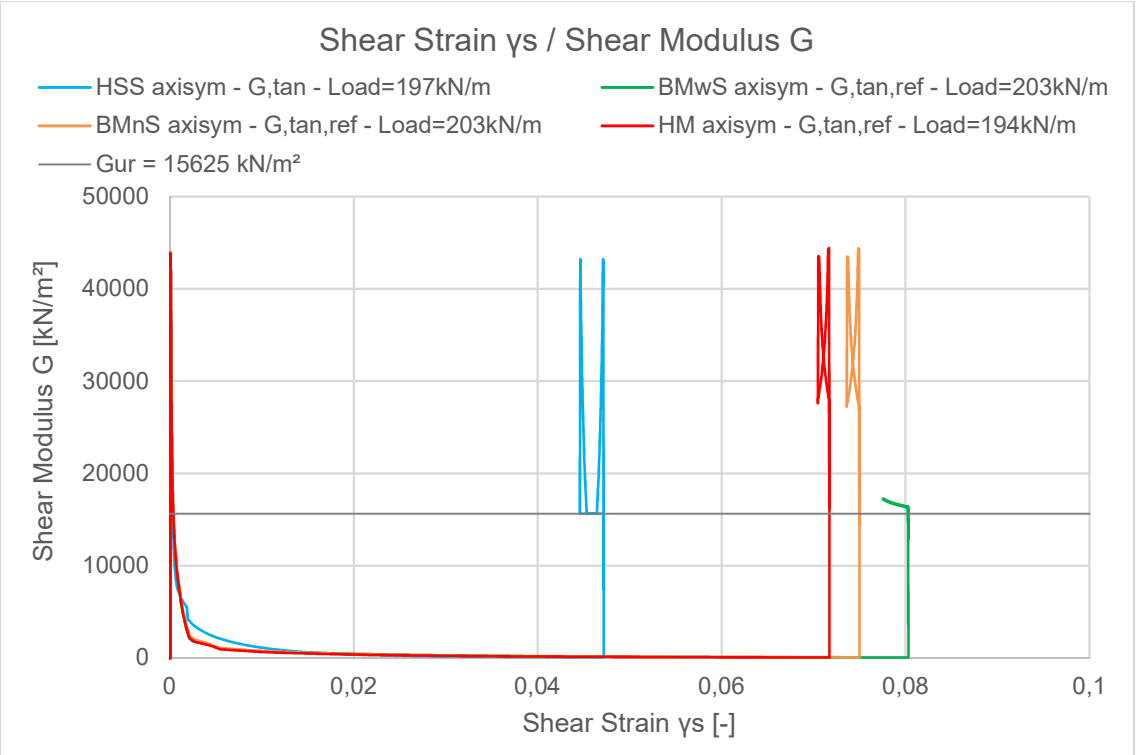

Figure 35 Axisymmetric tests; Small strain / unloading / reloading stiffness with $q_{vertical,max}$ – 2 kPa, Phase 1 – Phase 4

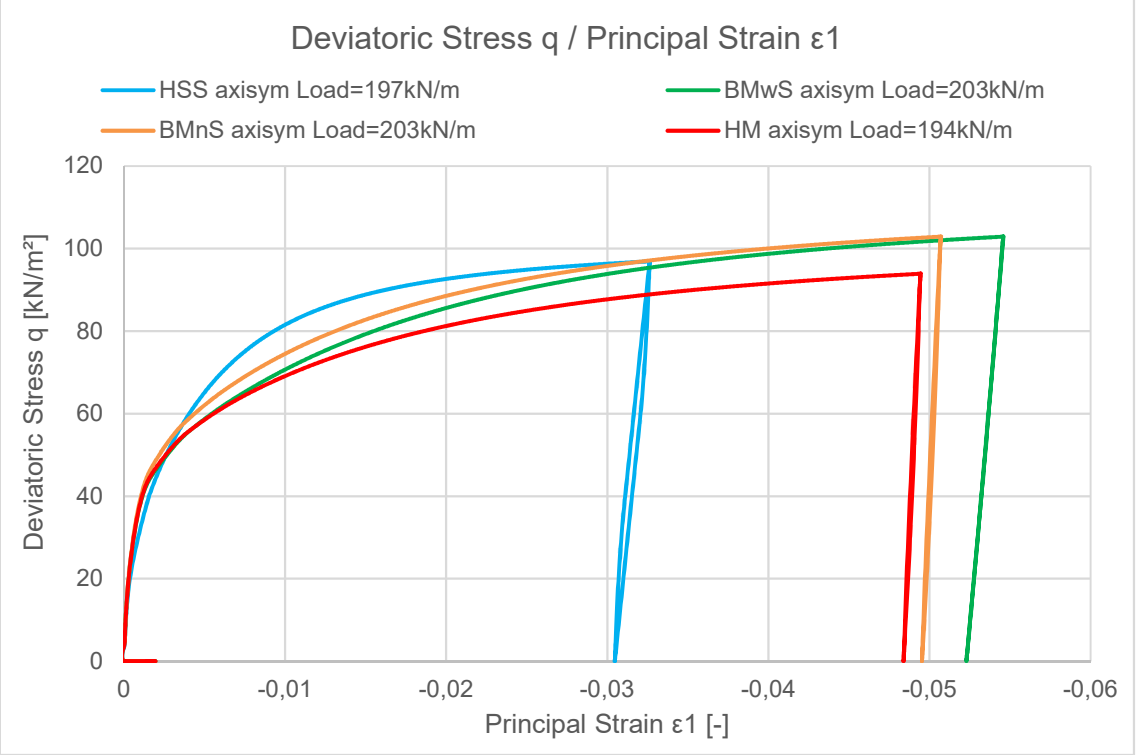

Figure 36 Axisymmetric tests; Stress-strain curves with $q_{vertical,max}$ – 2 kPa, Phase 2 – Phase 4

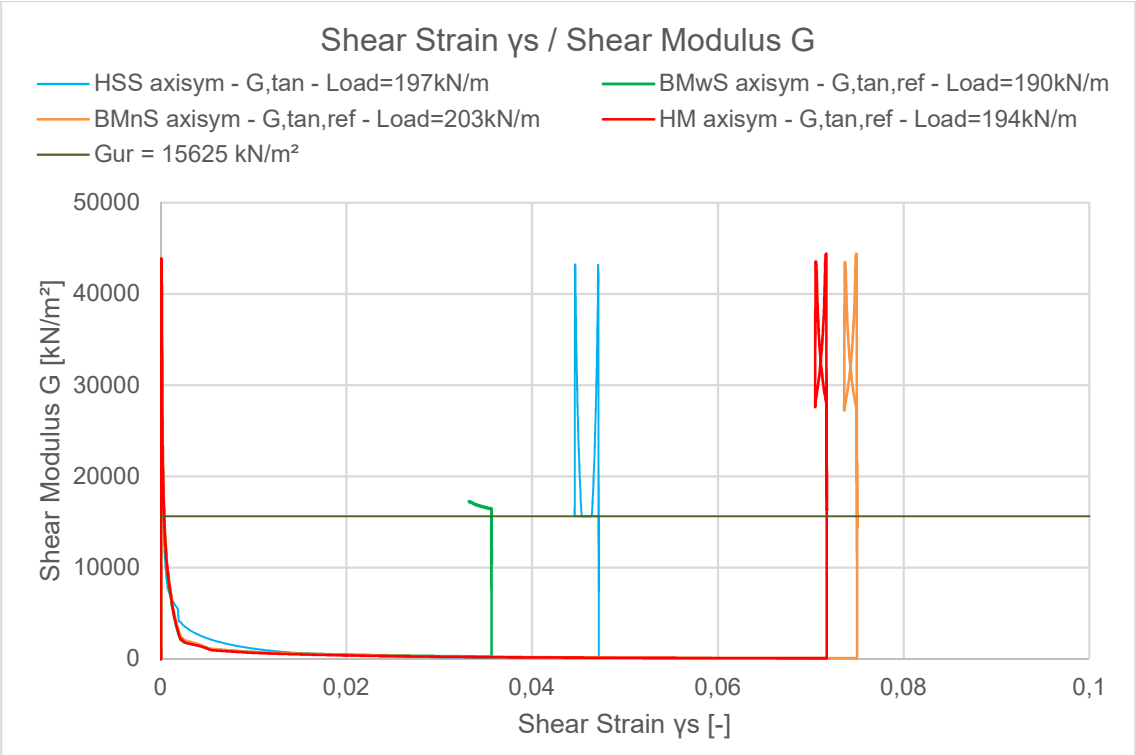

Figure 37 Axisymmetric tests, Small strain / unloading / reloading stiffness with $q_{vertical,max}$ = 190 kPa for the BMwS, Phase 1 – Phase 4

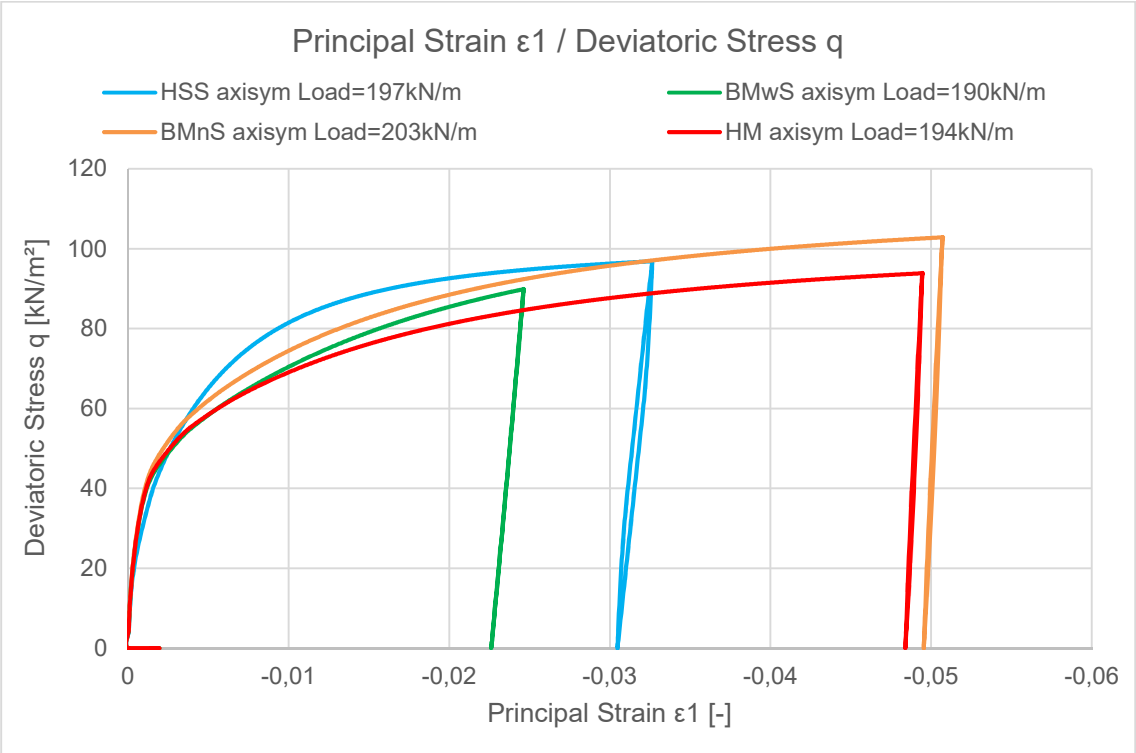

Figure 38 Axisymmetric tests; Stress-strain curves with $q_{vertical,max}$ = 190 kPa for the BMwS, Phase 2 – Phase 4

5.2.2 Influence of the maximum load fraction

The maximum load fraction (= LF) is a PLAXIS related term, which determines the maximum size of load / unbalance applied in one calculation step. The possible input value lies between 0 – 1 (default value = 0.5) and indicates the fraction which can be applied maximally at once (e.g. LF = 0.5 → 1/0.5 = 2 steps to solve the unbalance). It is important to note that this value only determines the maximum load fraction. If convergence concerning the stress-displacement behaviour is low, more steps are possible. Furthermore, the user might want to force more steps by using a smaller value in order to observe the deformation process or prevent divergence. (R.B.J. Brinkgreve, 2017)

Influence of the LF under constant loading direction: After the initial phase and the isotropic loading of the specimen, the axisymmetric models were loaded with $q_{vertical}$ = 300 kPa. Varying inputs for the max. load fractions were used, ranging from 0.05 – 0.9. In case of the multilaminate constitutive models a divergence issue was observed as shown in Figure 40. The behaviour of the HSS model is illustrated in Figure 39. The stress-displacement curve of the HSS model (Figure 39) is almost unaffected by any change of the LF and shows an accurate stress-displacement curve even with LF = 0.9. On the other side, the BMnS is highly influenced by the LF and shows inaccurate stress-displacement curves with increasing values for LF (Figure 40). Calculations with LF > 0.15 deliver already significantly deviating curves. However, a value of 0.15 cannot simply be taken as reference because the LF is associated to the maximum load itself. For instance, if $q_{vertical}$ = 400 kPa is applied the LF must be lower than 0.15 to obtain the same accuracy.

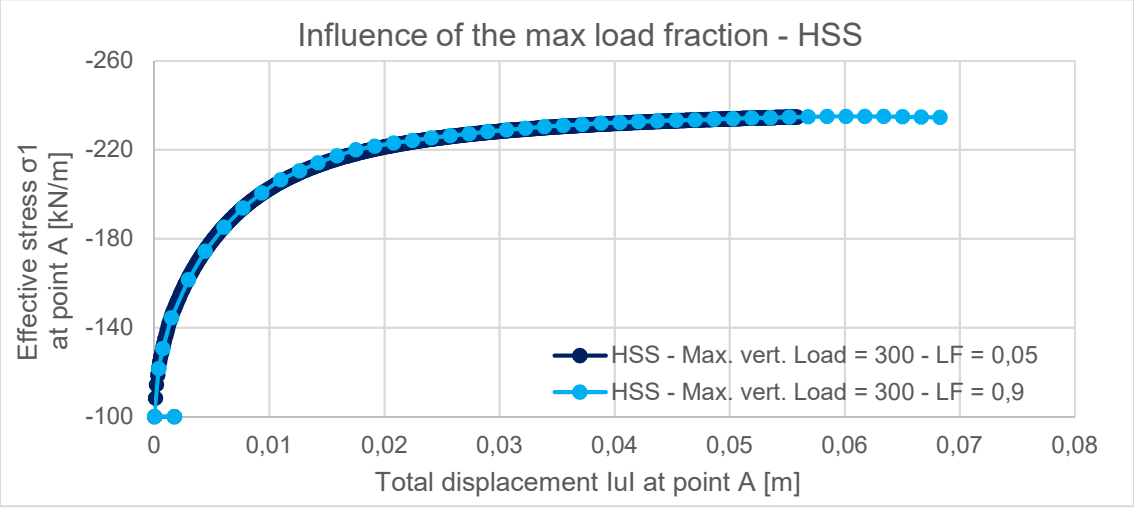

Figure 39 Influence of the maximum load fraction on the HSS model

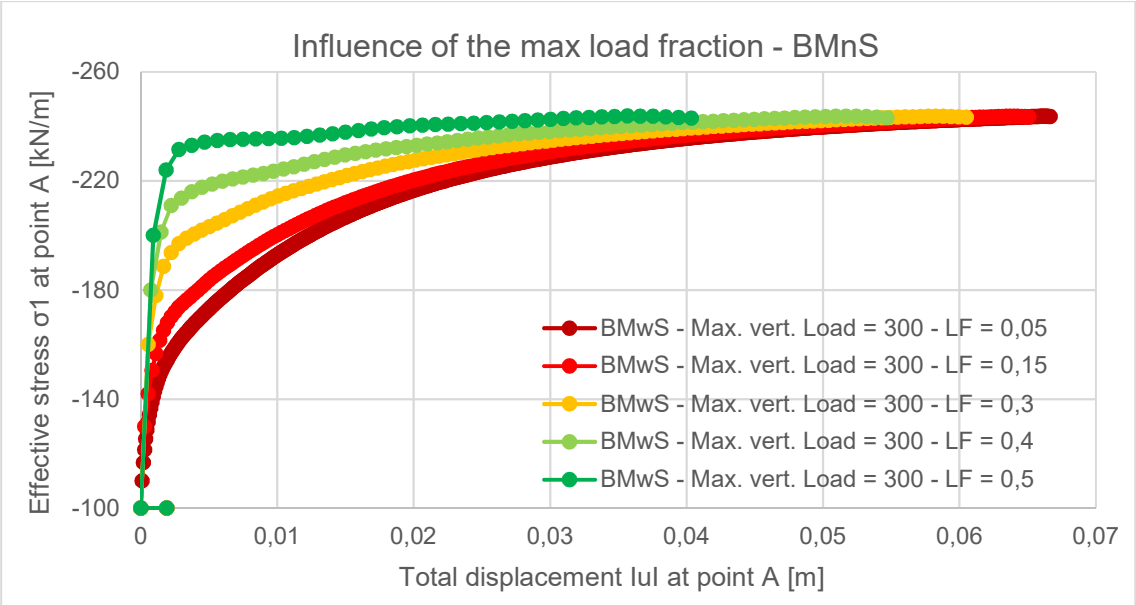

Figure 40 Influence of the maximum load fraction on multilaminate models

Influence of the LF under cyclic loading: Using a LF which is "too high" for the given load step, increases the calculation error and could lead to a significant distortion of results as shown in Figure 41 to Figure 44. All axisymmetric models were loaded with $q_{vertical}$ ≈ 200 kPa. Afterwards four unloading / reloading cycles were simulated with LF = 0.5 and LF = 0.05. Figure 42 and Figure 44 present the percental increase of displacement relative to the displacements after the first loading. Using a LF = 0.5, the percental increase of displacements for the multilaminate models is at 0.5% after four cycles. This percental increase of displacements drops down to roughly 0.1% if LF = 0.05 is applied. To obtain an error equal to zero is not possible due to numerical issues. However, a calculation error of 0.4% purely derives from using an inappropriate LF. Furthermore, the total displacements at the end of the last loading cycle, obtained from the multilaminate constitutive models, depend significantly on the applied LF. Applying a LF of 0.5 produces between 0.04 – 0.05 m of total displacements (Figure 41), whereas a LF of 0.05 results in total displacements of 0.06 – 0.065 m (Figure 43).

Again, a different LF barely affects the results of the HSS model. A percental increase of displacements of around 0.1% is obtained for both values for the max. load fraction. Furthermore, the HSS model produces a constant value of 0.032 m of total displacements at the end of the last loading cycle.

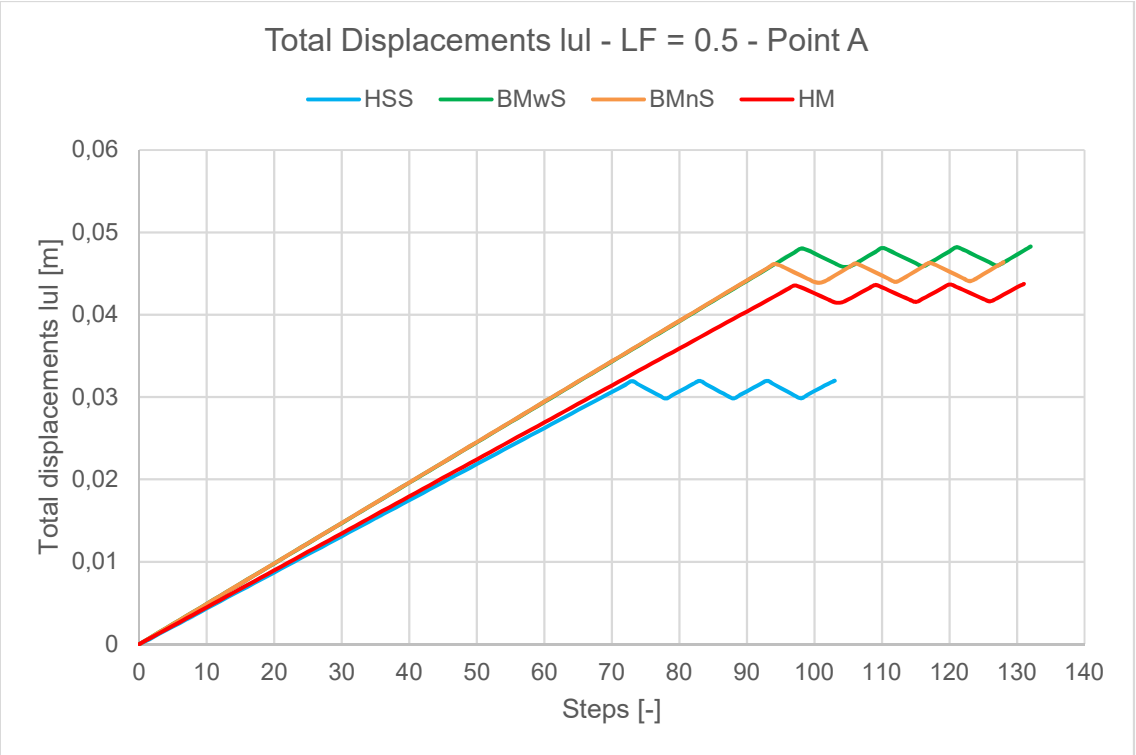

Figure 41 Total displacements due to cyclic loading with LF = 0.5

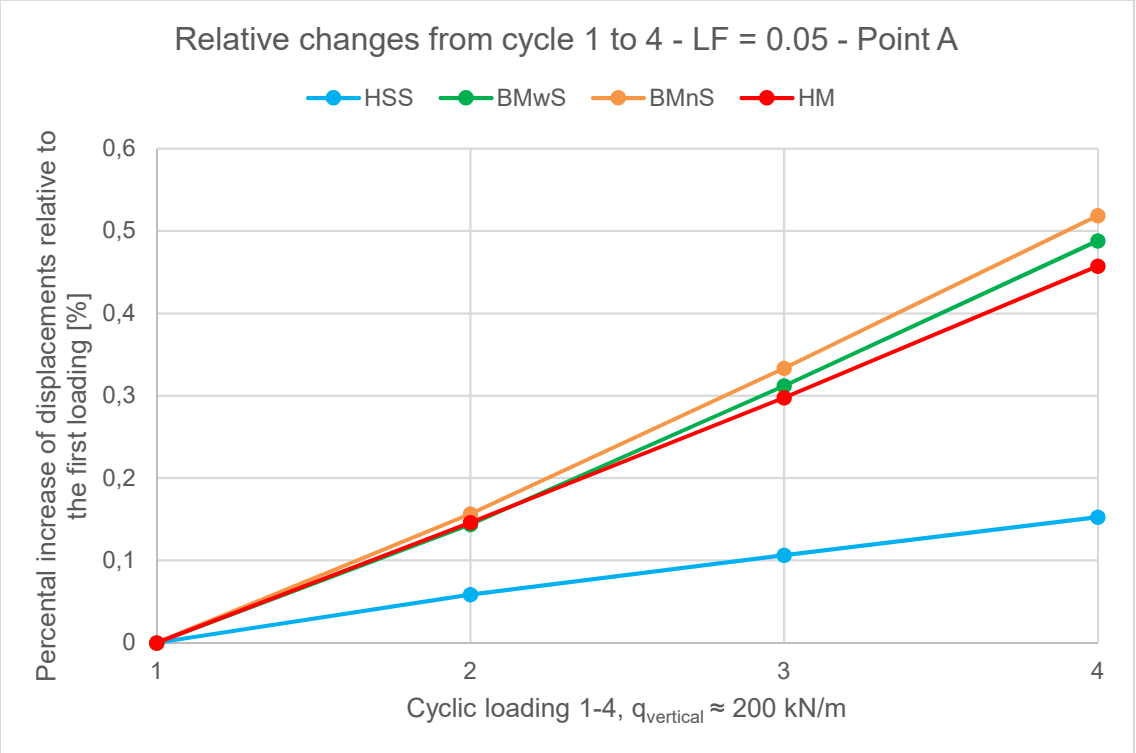

Figure 42 Relative displacements between the loading cycles with LF = 0.5

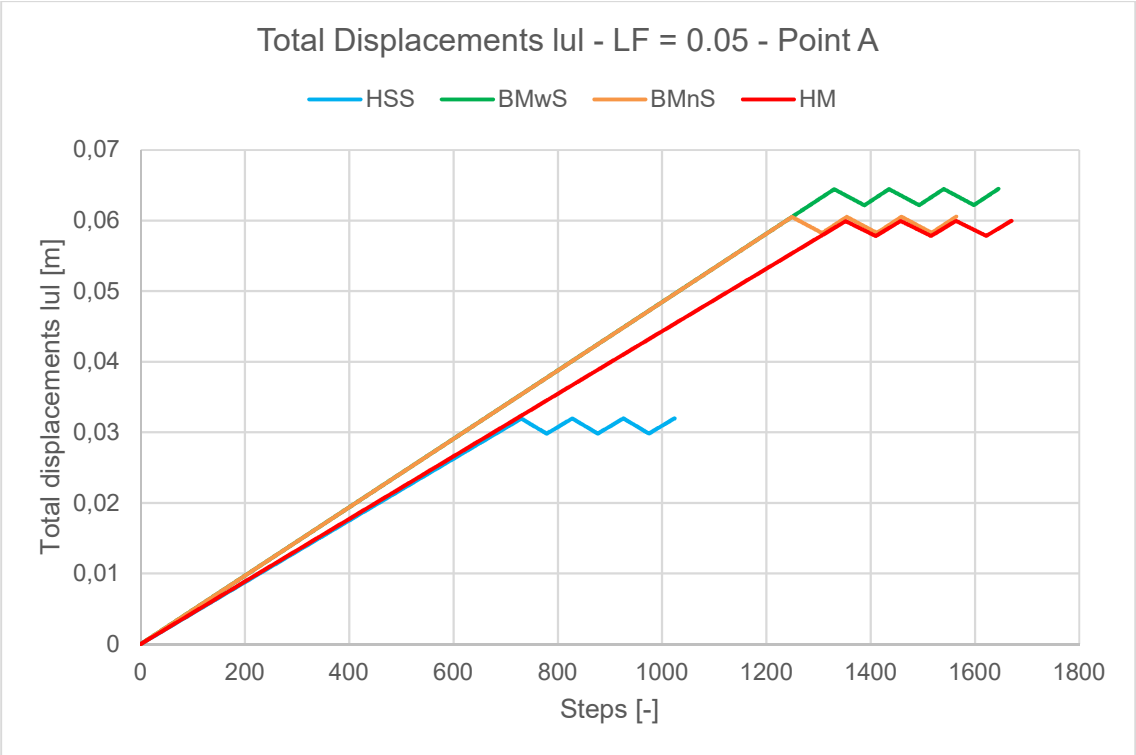

Figure 43 Total displacements due to cyclic loading with LF = 0.05

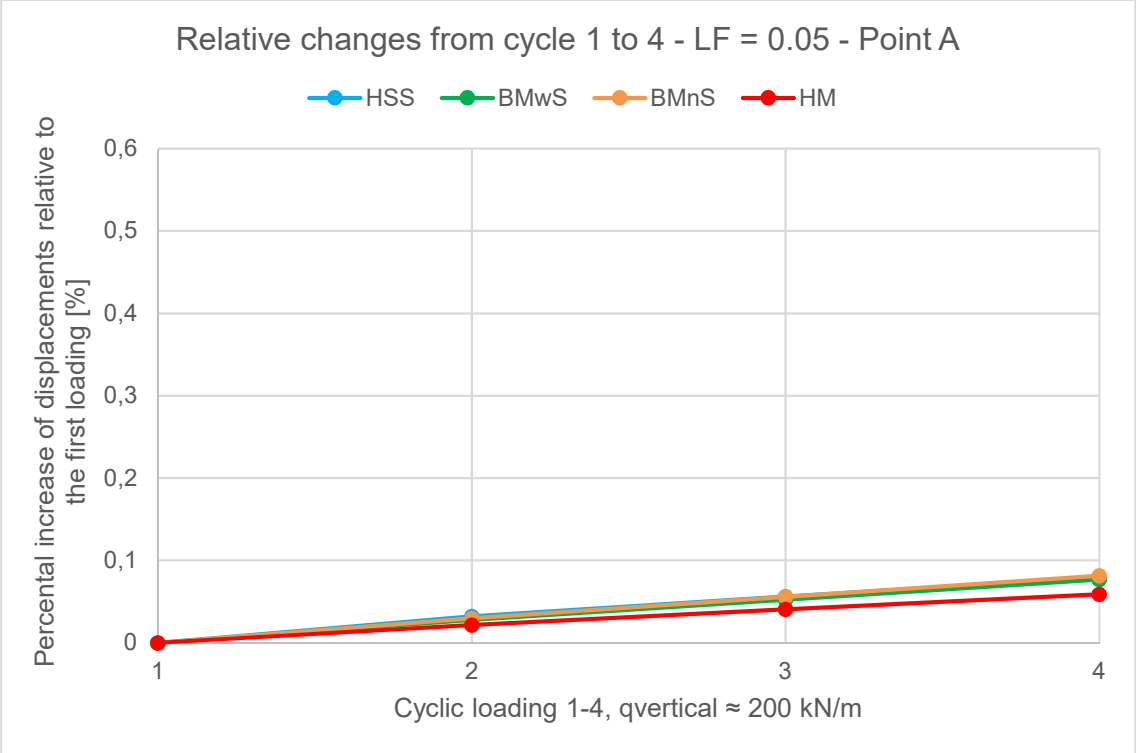

Figure 44 Relative displacements between the loading cycles with LF = 0.05

To obtain reliable results, the influence of the max load fraction should be checked for the specific model. Otherwise, a maximum value of LF <= 0.1 can be taken as a first estimation. Simulations in this thesis are calculated with LF = 0,05, if not declared differently.

5.3 Biaxial simulations with endplate

The numerical biaxial tests reported in this chapter were performed to study the constitutive model behaviour after the development of strain softening.

The model is 1m high and 0.25m wide with plates at the bottom and the top of the specimen. After the initial phase the simulation consists of four consecutive loading / unloading phases. The horizontal load $q_{horizontal}$ remains at $q_{horizonta}$ = 100 kPa during the complete simulation, while the vertical load $q_{vertical}$ starts at $q_{vertical}$ = 100 kPa and is increased to $q_{vertical,max}$ ≈ 200 kPa in phase 2 and phase 4. Hence a complete unloading reloading cycle is simulated (Figure 45).

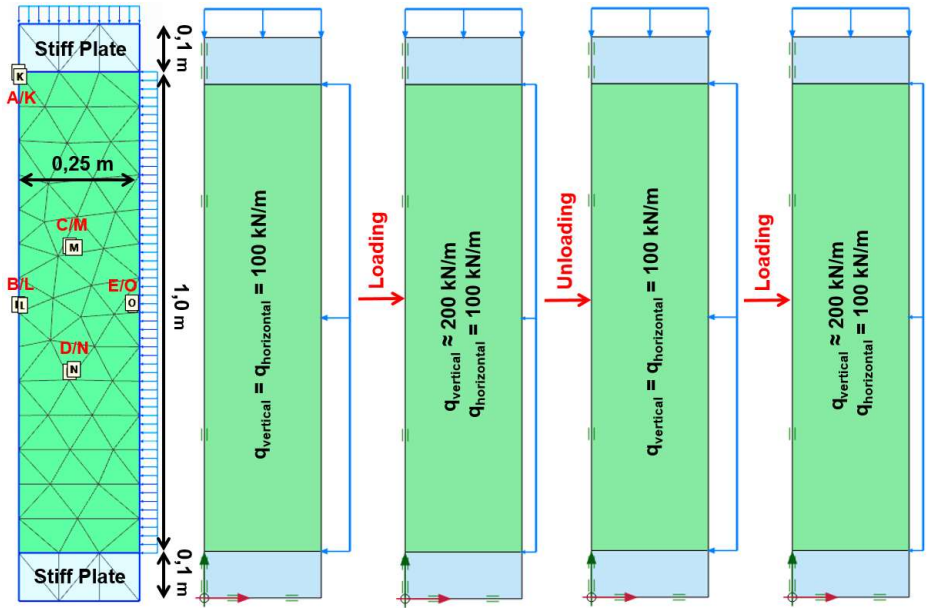

Figure 45 Model geometry and loading / unloading cycle, Number of 15-noded elements: 96

For each constitutive model the vertical load $q_{vertical,max}$ is increased up to 1 kPa below failure load. Hence, $q_{vertical,max}$ slightly differs between the constitutive models. It has to be noted that failure load in this context coincides with failure of the complete model. All values are summarized in Table 6.

Table 6 Summary loading / unloading cycle

	Biaxial model with plate							
	Phase 1		Phase 2 (1st loading)		Phase 3 (unloading)		Phase 4 (2nd loading)	
	$q_{vertical}$ [kPa]	$q_{horizontal}$ [kPa]	$q_{vertical}$ [kPa]	$q_{horizontal}$ [kPa]	$q_{vertical}$ [kPa]	$q_{horizontal}$ [kPa]	$q_{vertical}$ [kPa]	$q_{horizontal}$ [kPa]
HSS	100	100	196	100	100	100	196	100

BMwS	100	100	197	100	100	100	197	100
BMnS	100	100	201	100	100	100	201	100
HM	100	100	195	100	100	100	195	100

Unlike a model where the load is applied as a boundary condition directly to the soil specimen (Chapter 5.2), vertical loads are transferred to the specimen via stiff plates in the current simulations. The endplates lead to the following conditions:

- Non-uniform stress level in the hole specimen (Figure 46)
- Non-uniform strains in the hole specimen (Figure 46)
- Formation of shear bands (Figure 46)
- Appearance of failure points (Figure 46)
- Appearance of softening points

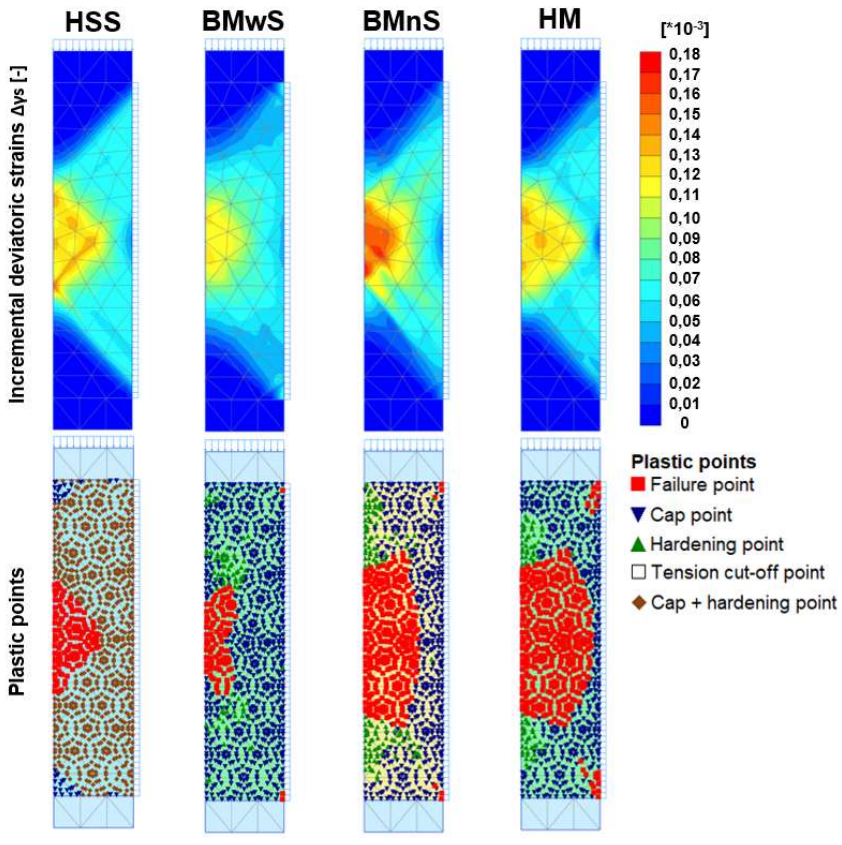

Figure 46 Biaxial models with end plates: Incremental deviatoric strains and plastic points indicate a non-uniform response

5.3.1 Stress-strain behaviour

Stress-strain curves of all calculations with endplates are shown in Figure 47 and Figure 48. The results at point L (Figure 47) are very similar to the already presented curves of

the models without endplates (chapter 5.2.1). All multilaminate models show no hysteresis in Point L, thus they show no appropriate small strain stiffness behaviour (chapter 5.2.1). Furthermore, they show a slight curvature at the end of the unloading / reloading phase, which indicates a change of the principal stress directions.

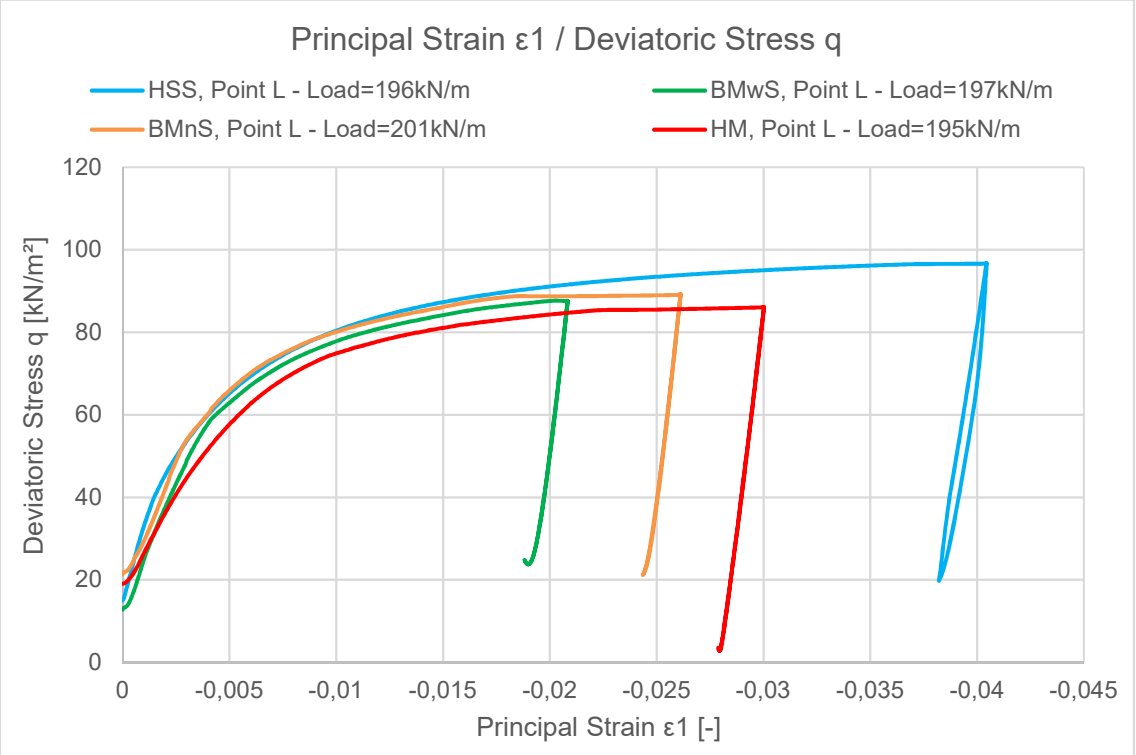

Figure 47 Biaxial tests; Stress-strain curves for all models at point L, Phase 2 – Phase 4

The stresses and strains at point K (Figure 48) are generally lower, thus the models are far from failure. Furthermore, stresses at Point K are significantly influenced by the stiff endplates.

As observed in chapter 5.2.1, lower stress states lead to rather appropriate behaviour concerning the small strain stiffness, thus all models except the HM, show hysteresis. The change of the principal stresses is even more significant at this point, due to the adjacent top endplate.

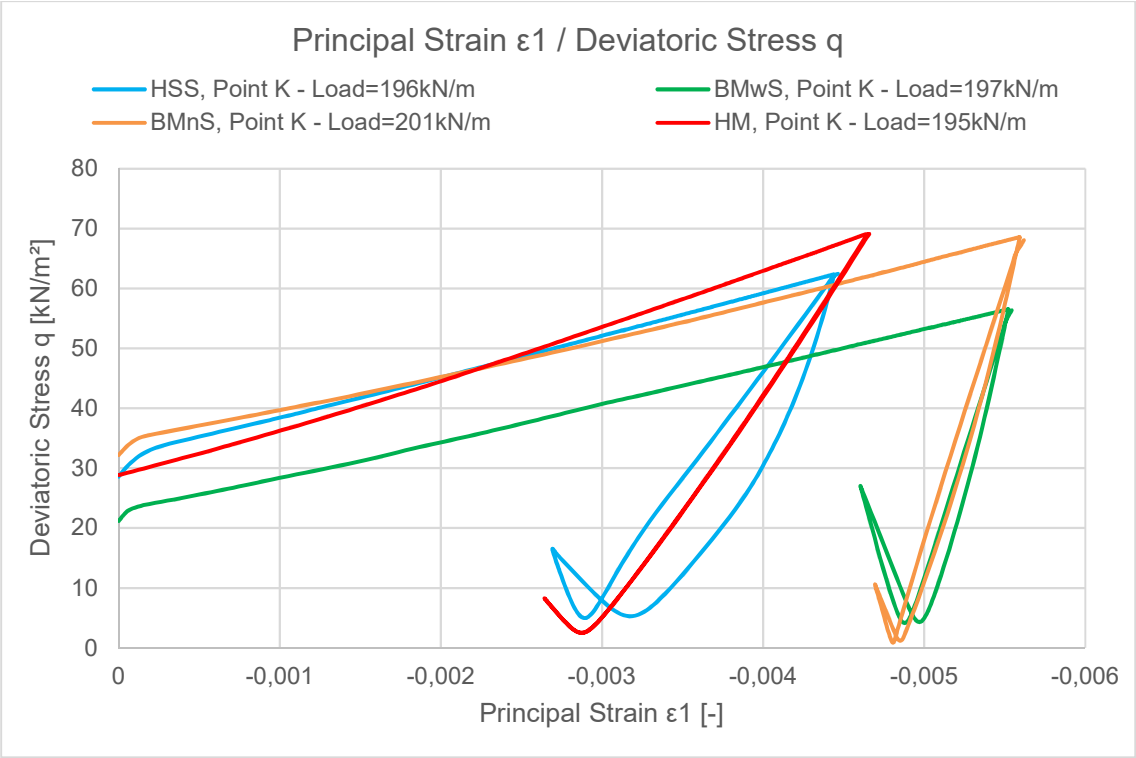

Figure 48 Biaxial tests; Stress-strain curves for all models at point K, Phase 2 – Phase 4

5.3.2 Determination of softening points

To evaluate the results produced by models using a multilaminate constitutive model with strain softening, it is essential to know which points or integration planes are in the strain softening range. For clarification, even if just a single integration plane is in the strain softening range, the associated stress point is considered as a softening point. There are two ways of evaluating softening points:

- Analysis of sate variables (BMwS, HM)
- Analysis of plastic points (only BMwS)

Analysis of state variables: For the BMwS, the state variables $tan\varphi_m$ (mobilised friction angle in softening) and c_i (cohesion in softening) deliver data about softening. The equivalent for the HM is the state variable ε_{di} (local damage strain). Apart from the information, whether an integration plane (and therefore the stress point) is in softening or not, the data also indicates how much softening already occurred. Beside the fact that the state variables deliver a lot of information, the analysing process is relatively time consuming and inconvenient.

Analysis of plastic points: The following only accounts for the BMwS. As a quick alternative to the state variables, plastic points give an indication about the state of stress points. A stress point marked as failure point indicates that it is in the strain softening

range. However, attention has always to be paid on the plastic point history. A stress point is marked as a failure point as long as it lies at the failure surface. Any shift back into the elastic range leads to a different plastic point indication, although strain softening already occurred. Hence, every softening point was a failure point at least once during the calculation. The analysis of plastic points for determining the number of softening points cannot be applied to the HM due to the additional Hvorslev surface. Figure 49 and Figure 50 show how failure points compare to softening points during the two loading cycles of the biaxial model.

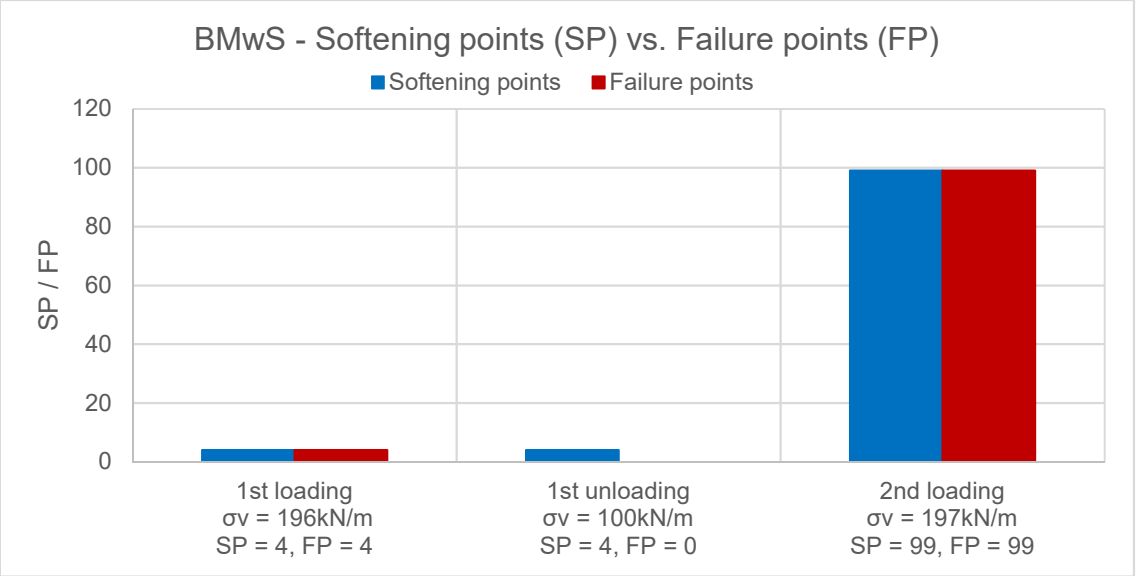

Figure 49 Comparison of softening points (SP) vs. failure points (FP) – BMwS

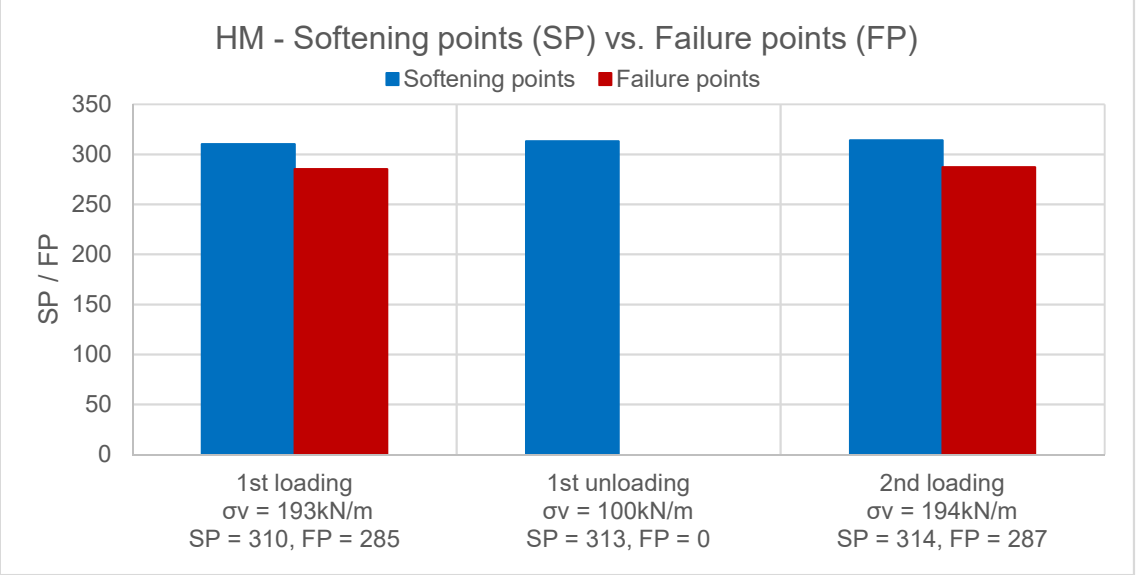

Figure 50 Comparison of softening points (SP) vs. failure points (FP) – HM

5.3.3 Development of softening points due to cyclic loading

The following results concerning the development of displacements and softening points due to cyclic loading, are obtained by simulating four loading cycles onto the biaxial model with endplates.

Development of displacements due to cyclic loading for all models: Figure 51 shows the total displacements at the top of the soil sample for all loading phases. Figure 52 shows the percental increase of displacement for each loading phase in point A, relative to the displacements after the first loading. The relative increase of displacements of the HSS model is around 1% after four loading cycles, whereas the multilaminate models produced an increase of 0.2 – 0.6%. This small increase of displacements can be related to the numerical error, hence there is no indication of an influence of strain softening concerning the increase of displacements due to cyclic loading for this simulation. Due to the theoretical formulation of the constitutive models, these results are as expected. The un- / reloading cycles are only performed in the elastic range. Therefore, no additional plastic strains are produced and additional strain softening is impossible.

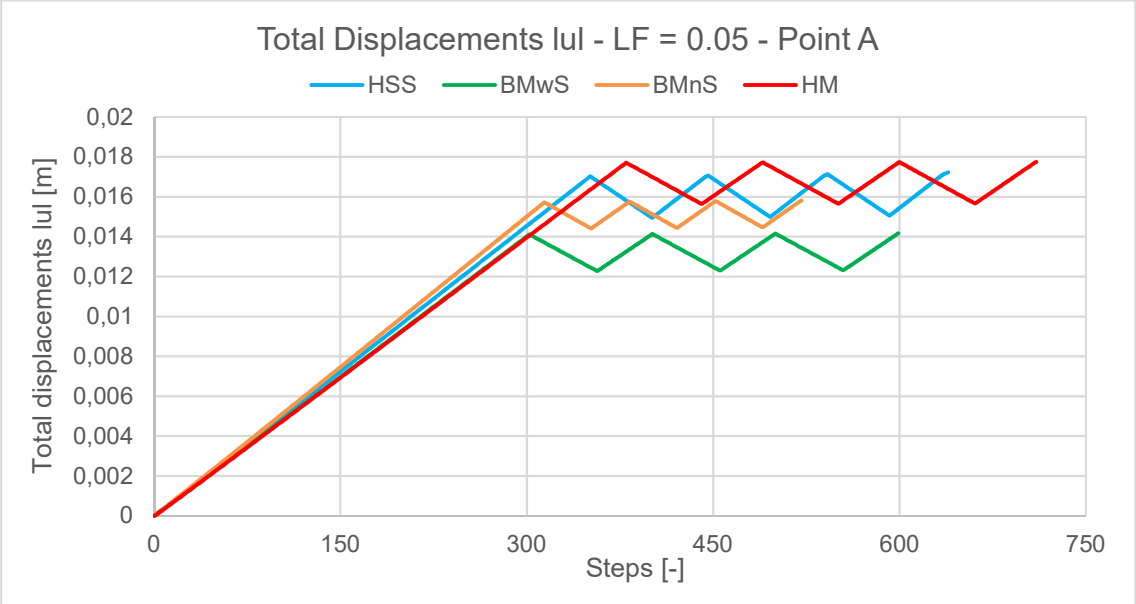

Figure 51 Total displacements due to cyclic loading at point A

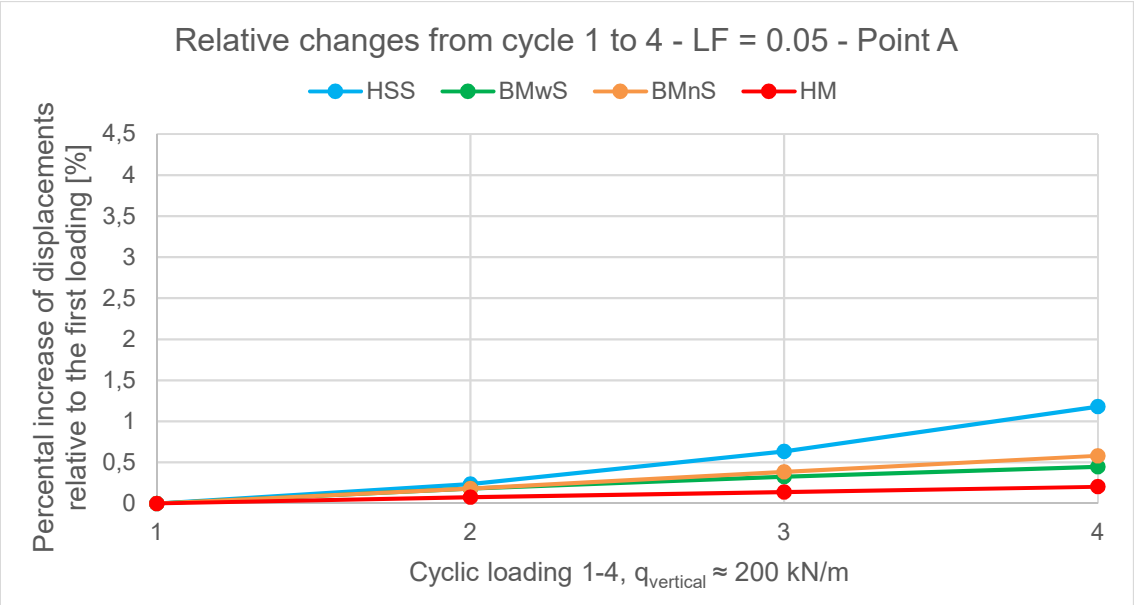

Figure 52 Relative displacements between the loading cycles at point A

Evaluation of the strain softening behaviour due to cyclic loading for the BMwS:
The softening rate for stress points or integration planes in softening is defined by:

$$SR = \frac{|\varphi_{current} - \varphi_{peak}|}{|\varphi_{res} - \varphi_{peak}|} \quad (29)$$

For instance, a softening rate of 0% indicates that no softening occurred. A softening rate of 100% indicates that full softening occurred, with strength parameters in the softening points equal to the defined residual strength parameters. Figure 53 shows the development of the softening rate for the stress point with the minimum strength values for each loading phase. Figure 54 shows the mean softening rate for all stress points in softening for each loading phase. Both figures indicate that strain softening certainly occurs within the first phase. However, the softening rates for φ and c remain for the following phases, which underlines the previous observation that strain softening has no significant influence on this particular simulation. Furthermore, it has to be noted that the number of integration points in softening remains at 111 points for all loading cycles. Again, these results are as expected, no additional plastic strains are produced and additional strain softening is impossible.

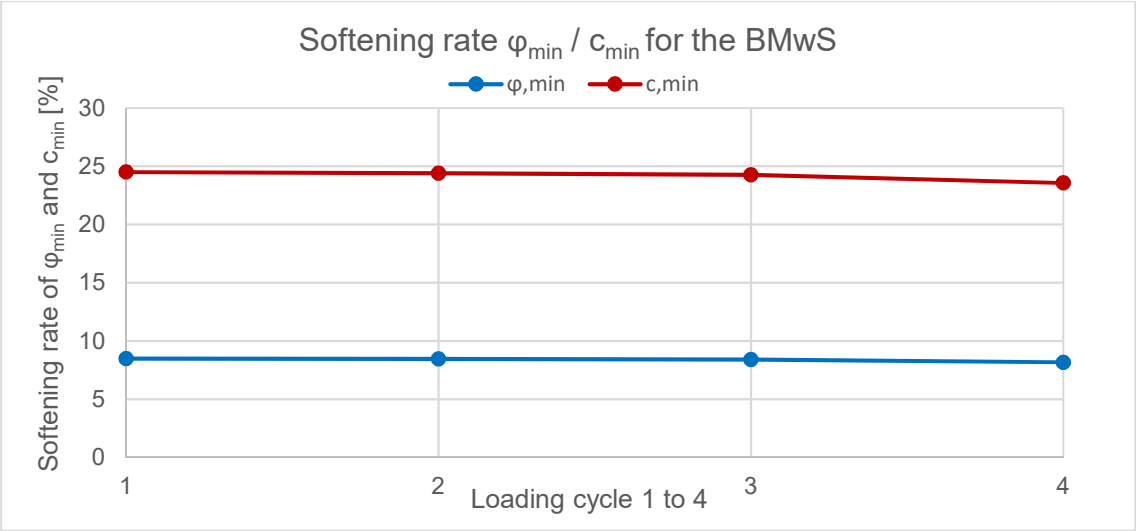

Figure 53 Development of the softening rate for the stress point with the minimum strength values

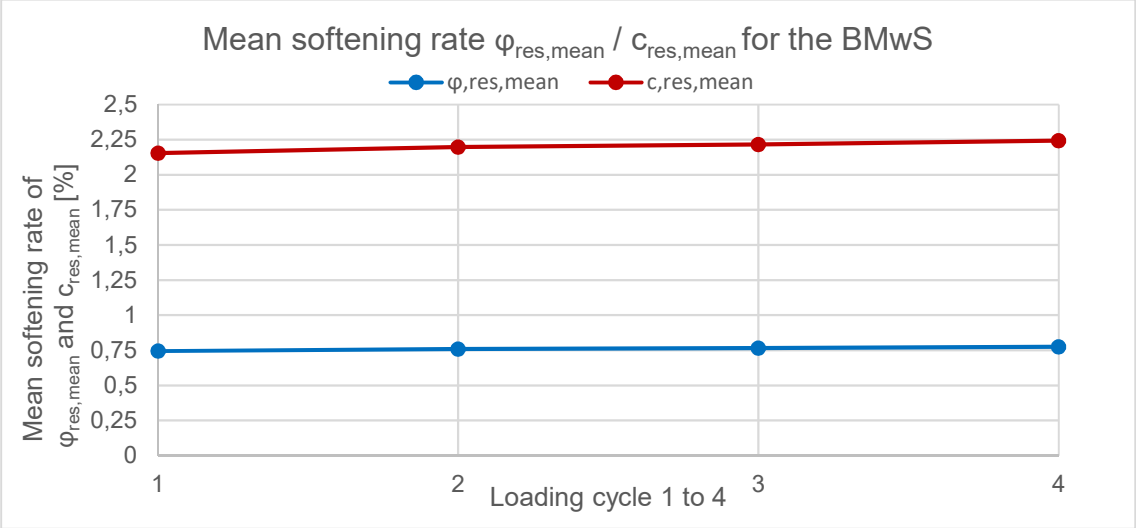

Figure 54 Mean softening rate for all stress points in softening

5.4 Conclusion

The analyses with simple axisymmetric- and biaxial models revealed several points, which have to be considered when the multilaminate models are applied to boundary value problems.

Under certain stress states, the BM as well as the HM show no hysteresis during the unloading / reloading cycle. Furthermore, attention has to be paid on the input of the maximum load fraction (LF). A high input of LF, or even the default value ($LF_{default}$ = 0,5), could lead to inaccurate results regarding the stress-strain behaviour of the material. This holds for all used multilaminate models. A sufficient value for the LF, depends highly on the maximum load itself. Hence, no absolute recommendation can be made. But a value of 0.1 or smaller is suggested and should lead to acceptable results in most cases.

A comparison between the BMwS and the BMnS revealed that the stress strain behaviour is significantly different, even before strain softening emerges. This can be explained by the mandatory use of a different K_0 value for each model. The K_0 value of the BMwS should always depend on the residual strength parameters. This circumstance inflicts that, either the K_0 values of the two models are distinct, or the peak strength values of the BMwS do not match the strength values of the BMnS. Hence, the behaviour of both models cannot match, even before strain softening.

For the BMwS, softening points are equal to failure points (→ failure history has to be observed) and vice versa. This doesn't count for the HM, where most softening points equal failure points but not necessarily have to.

As expected, cyclic loading has no significant influence on the development of displacements or the strain softening behaviour if the cyclic loading produces no additional strains. The additional obtained strain softening and displacements after four loading cycles are within the numerical error.

6 Multilaminate models applied to a simple slope

In order to investigate the influence of strain softening on the deformation characteristics and the FoS of a slope, a simple slope (see chapter 2.3.1) was modelled with the BMwS, considering an undrained excavation and water level changes under undrained conditions, all followed by a consolidation analysis. Considering that the application of an "automatic" φ - c reduction is not feasible for multilaminate constitutive models, the strength parameters were reduced stepwise until failure was reached. The FoS was calculated manually. For comparison, additional simulations were carried out with the BMnS and the HSS model. Furthermore, the softening rate of the BMwS depending on the FoS of the system will be discussed in this chapter. Finally, attention is paid to the question whether fluctuating water levels may lead to an additional softening of the slope material.

6.1 Numerical model and material parameters

The numerical model is an undrained, plane strain simulation of an excavation and subsequent groundwater fluctuations (Figure 55). The used drainage type is Undrained (A). The geometry relates to the model used in chapter 2.3 (Figure 4).

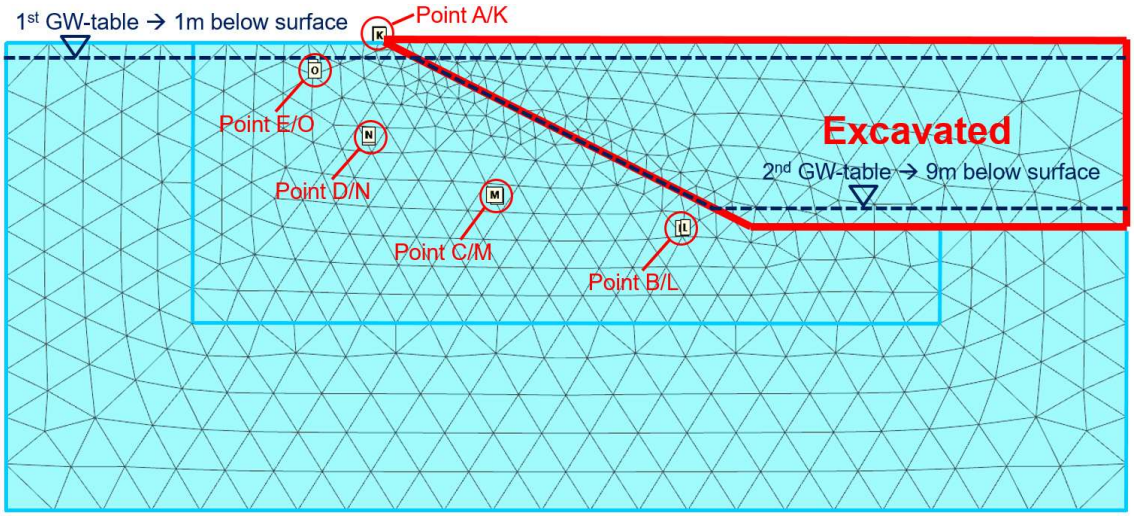

Figure 55 FE-model with 880 15-noded elements

Following phases were simulated:

- Initial phase (1st GW-table) (K_0-procedure)
- Phase 1: Excavation creating the slope (1st GW-table)
- Phase 2: Consolidation until minimum excess pore water pressure of 0.5 kPa is reached (1st GW-table)
- Phase 3: GW – drawdown of 8 meters (2nd GW-table)

- Phase 4: Consolidation for 0.5 days (2nd GW-table)
- Phase 5: GW – raise of 8 meters (1st GW-table)
- Phase 6: Consolidation for 0.5 days (1st GW-table)

The following tables present the material properties (Table 7) and the coordinates of the selected nodes of interest (Table 8), respectively. For material parameters, which are not listed, see Table 4. The difference between peak cohesion and residual cohesion for the BMwS has to be very small, otherwise the slope fails immediately after the first drawdown (Phase 3).

Table 7 Initial material parameters

Parameter	BMwS	BMnS	HSS	Unit
c'_{peak} =	6	6	6	[kPa]
φ'_{peak} =	40	40	40	[°]
K_{0nc} =	0.4264	0.3572	0.3572	[-]
φ'_{res} =	37	40		[°]
c'_{res} =	5.7	6		[kPa]

Table 8 Selected points

	A / K	B / L	C / M	D / N	E / O
x	20 / 20.03	36.24 / 36.41	26.33 / 26.18	19.43 / 19.43	16.47 / 16.56
y	0 / -0.05	-10.34 / -10.29	-8.67 / -8.57	-5.51 / -5.35	-1.74 / -1.93

6.2 Deformation characteristics

The deformations of points A and C are shown in Figure 56 (all models) and Figure 57 (only Basic models) for the most critical phases; Phase 3 (Drawdown) and Phase 4 (Consolidation). Figure 58 (all models) and Figure 59 (only Basic models) show the displacements of the slope surface after Phase 4 (Consolidation). For reasons of visibility, the displacements are multiplied by factor 5 (Figure 58) and by factor 30 (Figure 59). The displacements in x-direction are positive for movements to the right side, whereas the displacements in y-direction are positive for upward movements.

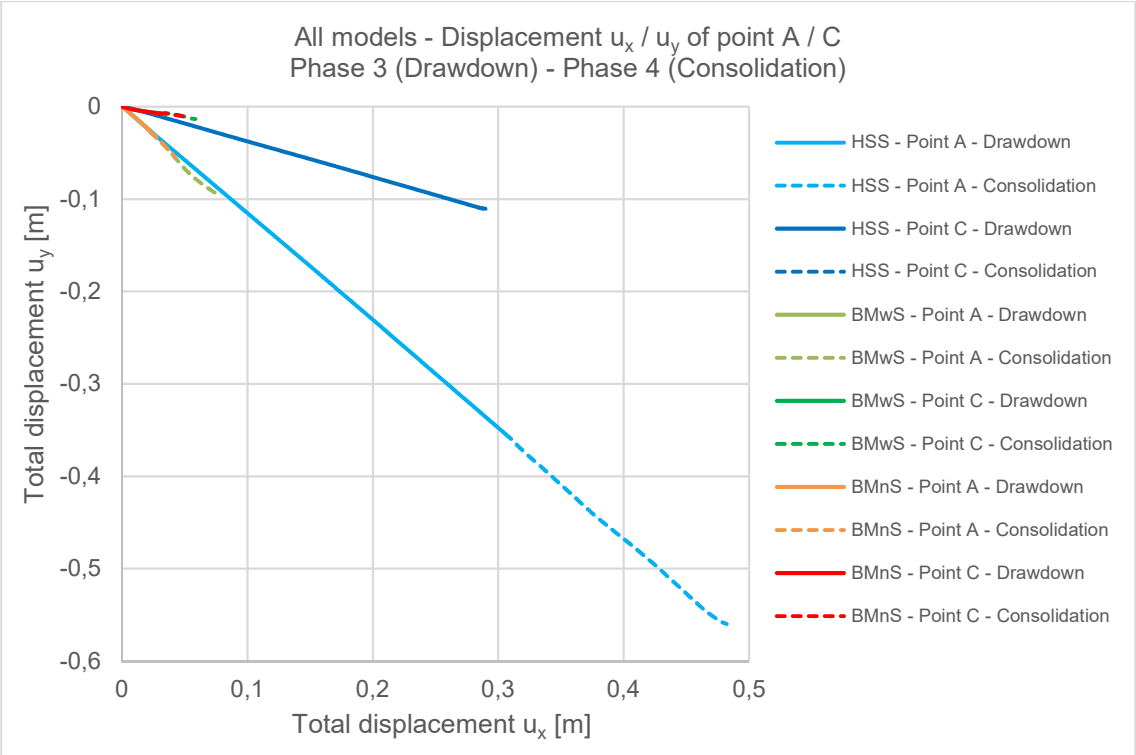

Figure 56 Displacements of point A / C during phase 3 and 4 for all models

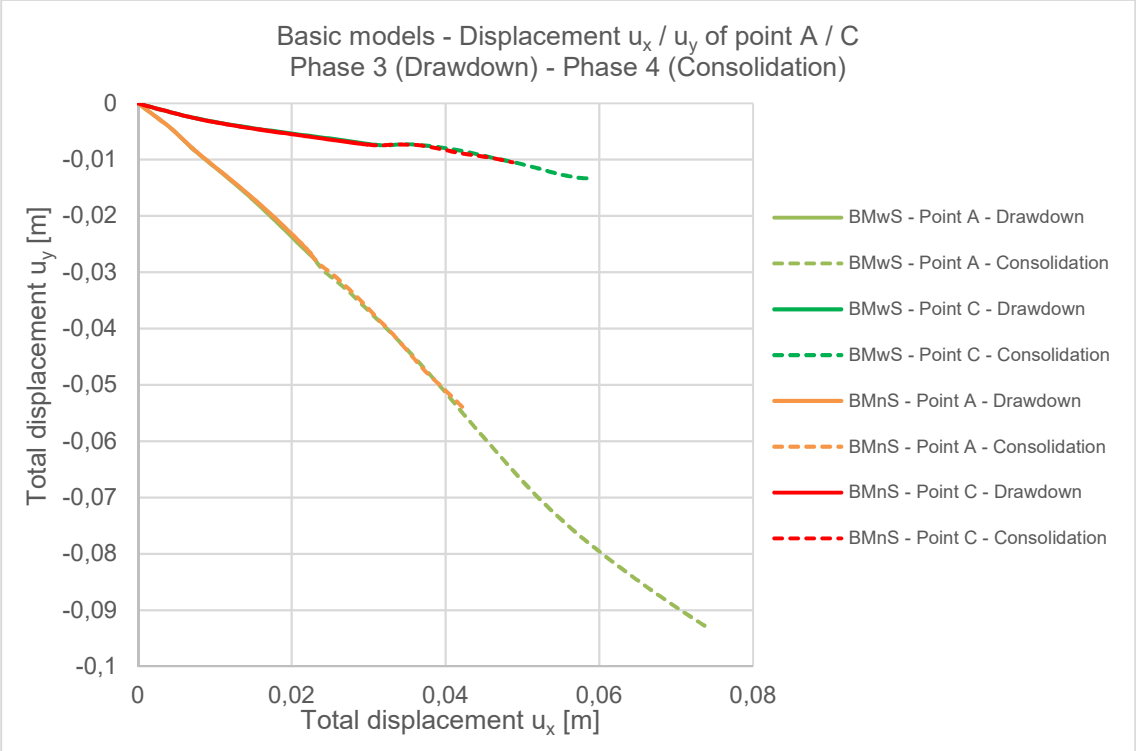

Figure 57 Displacements of point A / C during phase 3 and 4 for the Basic models

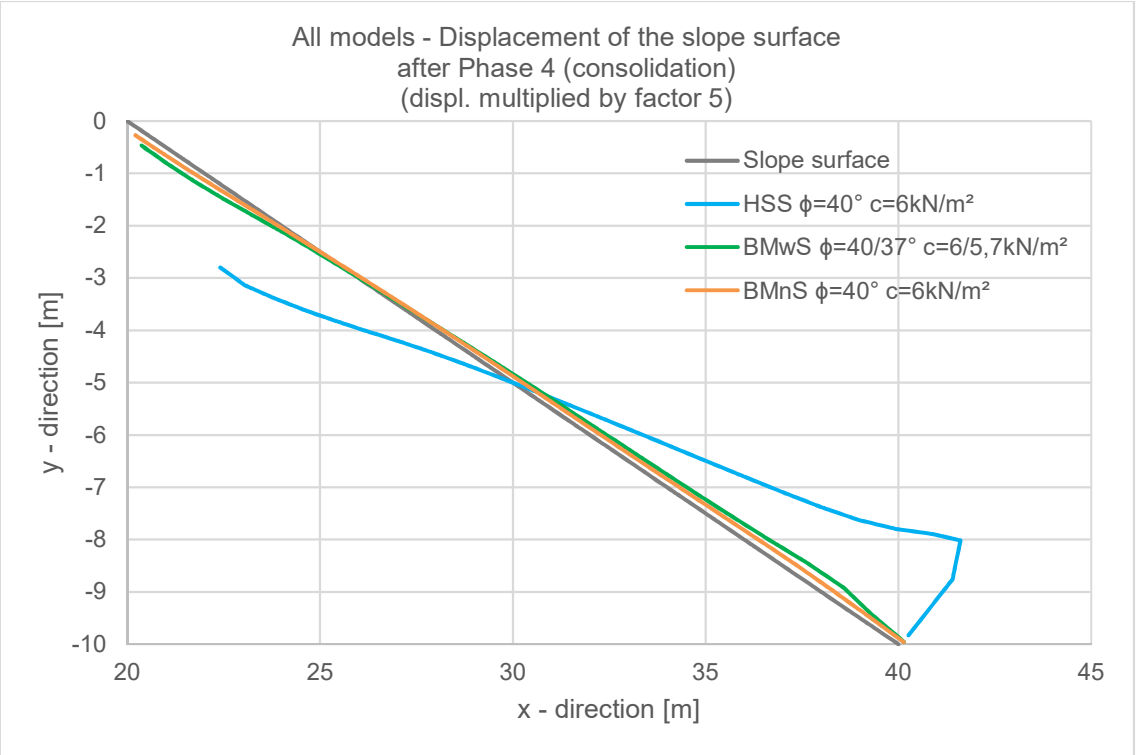

Figure 58 Displacements of the slope surface after phase 4 (consolidation) for all models

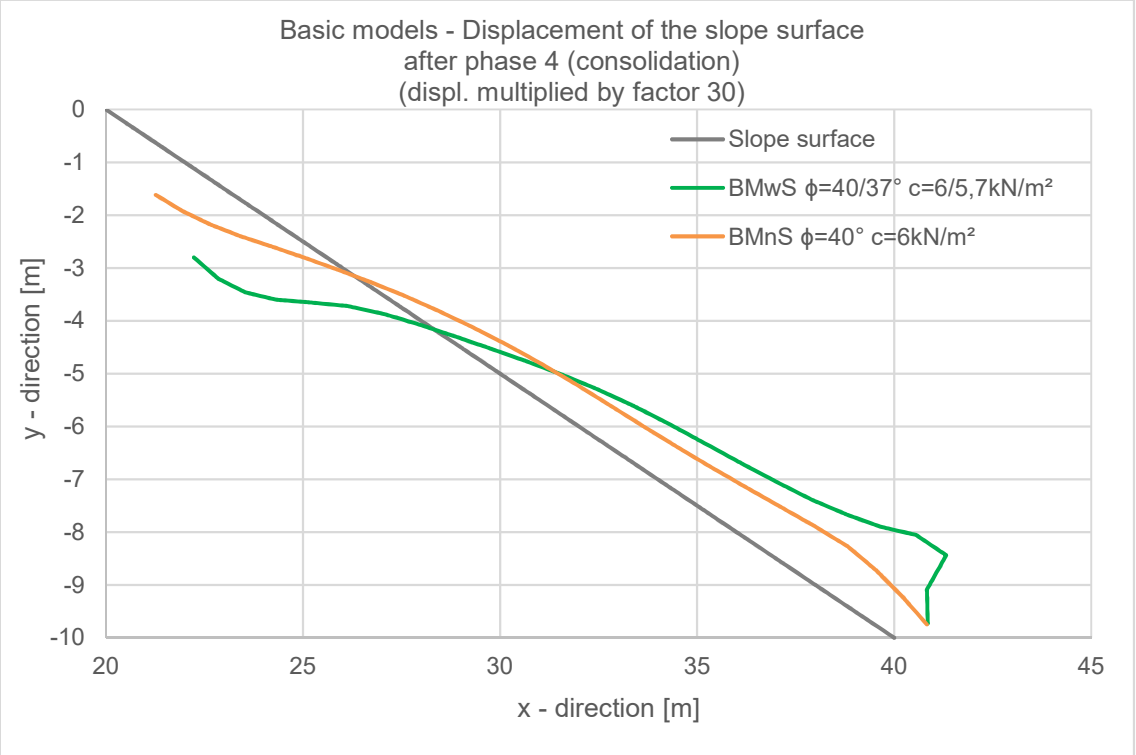

Figure 59 Displacements of the slope surface after phase 4 (consolidation) for the BMwS and the BMnS

In general, all models show qualitatively very similar displacement characteristics. However, the HSS model produces much larger displacements than the Basic models. The studies concerning the general behaviour of the multilaminate models (chapter 5),

already showed, that simulations with the HSS model result in different strains compared to the multilaminate models. Further adjustment of the hardening parameters for the multilaminate models may lead to a more comparable deformation behaviour between the HSS- and the Basic models. Figure 60 shows the failure points after phase 4 (consolidation) for all three constitutive models. The distinct slip surface in case of the HSS model occurs already in phase 3 (drawdown). However, the multilaminate models produce only a small amount of failure points in the middle of the slope during the drawdown. The apparent slip surface for the BMwS develops in the consolidation phase. Due to this higher amount of failure points in the HSS model, significantly higher deformations are produced with the HSS model in the drawdown phase (phase 3).

The results of the multilaminate models are relatively similar to each other, with the BMwS producing deformations approximately two times larger than the BMnS after phase 4 (consolidation). After the drawdown event, the deformations are similar. This difference in deformations after the consolidation can be explained by the development of failure points in the system. The BMwS is much closer to failure after phase 4 (see chapter 6.3), hence produces more failure points with a distinct slip surface (Figure 60). The appearance of failure points far away from the slip surface could be related to the development of pore water pressures during the drawdown (phase 3) and the consolidation (phase 4). The area with the highest pore water pressures compares relatively well with failure points of the BMnS and the BMwS in the middle of the slope. In this case an influence of the strain softening on the deformation behaviour of a mainly load-controlled system is apparent. However, this is mainly due to the general state of the slope near to the ultimate limit state. Under such conditions, sufficient deformations are produced by the loading to cause a significant softening.

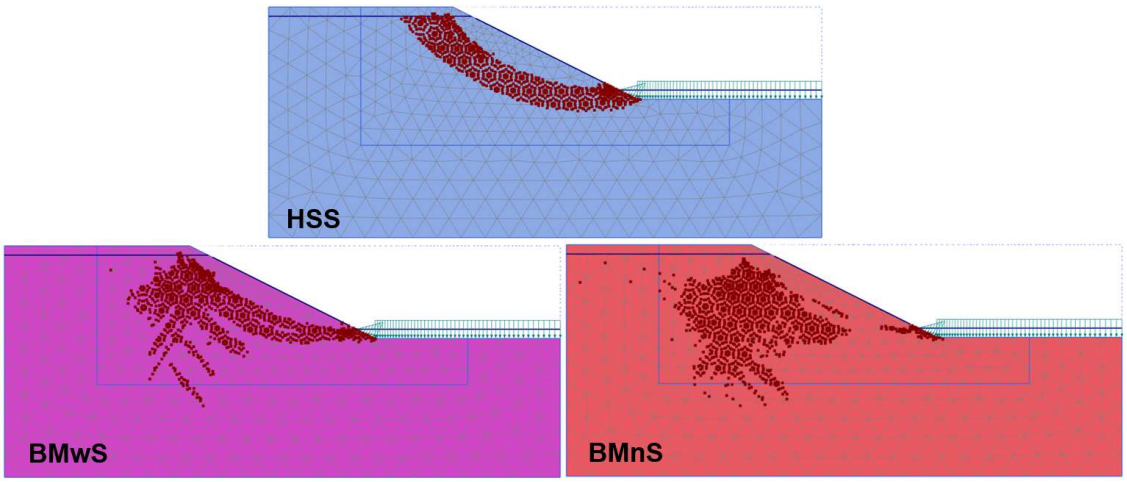

Figure 60 Total amount of failure points (failure point history) after phase 4 (consolidation)

6.3 Influence of strain softening on the stability of a simple slope

To determine if strain softening has a significant influence on the stability of this simple slope, the FoS was calculated for all three models (BMwS, BMnS, HSS). Since an "automatic" φ - c reduction is not feasible for multilaminate constitutive models, the FoS, were obtained by manually reducing the strength parameters stepwise until failure occurred in one phase. Next, the systems with strength parameters right before failure occurred, were determined as reference systems with FoS = 1.0. Accordingly, the FoS for the initial systems ($\varphi'_{initial}$ = 40°, $c'_{initial}$ = 6 kPa) were obtained with:

$$FoS = \frac{c'_{initial}}{c'_{FoS=1}} = \frac{tan\varphi'_{initial}}{tan\varphi'_{FoS=1}} \quad (29)$$

The accuracy of the determined FoS is not higher than the interval between the reduction steps. The interval was set to 0.01 multiplied by the initial strength parameters, thus the error cannot be larger than 0.01 concerning the FoS. This interval was applied to all strength parameters equally, including the residual strength parameters of the BMwS. Table 9 presents the obtained FoS for all three models with the used strength parameters.

Table 9 Strength parameters with corresponding FoS for all models

BMwS			**BMnS**			**HSS**		
φ'_{peak} φ_{res}	c'_{peak} c_{res}	**FoS**	φ'	c'	**FoS**	φ'	c'	**FoS**
40 37	6 5.7	1.01	40	6	1.08	40	6	1.07 (1.03)
39.72 36.73	5.94 5.64	1.00	37.85	5.55	1.00	38.10	5.61	1.00
39.44 36.46	5.88 5.59	< 1.00 Failure in phase 4	37.58	5.50	< 1.00 Failure in phase 4	37.85	5.55	< 1.00 Failure in phase 3

The FoS obtained by the BMwS is lower (FoS = 1.01) than the FoS obtained by the BMnS (FoS = 1.08). Consequently, the activation of softening in the Basic model has an influence on the factor of safety of the slope.

For the HSS model two different FoS were obtained. By applying the method of a stepwise reduction of the strength parameters, a FoS of 1.07 could be observed. Applying the standard safety analysis ("automatic" φ - c reduction without activation of IUB, see chapter 2.3.5) after the critical drawdown (Phase 3), results in a FoS of 1.03.

However, in case of the HSS model, the FoS obtained by the stepwise reduction (FoS = 1.14) has been taken as reference, according to the suggestions mentioned in chapter 2.4.

6.3.1 Degree of softening in case of the BMwS depending on the FoS

The following figures were evaluated to investigate the softening rate concerning the stability (FoS) of a load controlled system. To extend the following diagramms above a FoS of 1.01 (Table 9), additional simulations with slightly higher strength parameters (= higher FoS) were carried out. Table 10 presents the used strength parameters with the corresponding FoS.

Table 10 Strength parameters with corresponding FoS for the BMwS

BMwS		
φ'_{peak} φ_{res}	c'_{peak} c_{res}	FoS
41.65 38.62	6.36 6.04	1.07
40.84 37.82	6.18 5.87	1.04
40.56 37.55	6.12 5.81	1.03
40.28 37.27	6.06 5.76	1.02
40 35	6 5	1.01
39.72 36.73	5.94 5.64	1.00

The evaluation of the softening rate was performed after the final phase (phase 6 – consolidation), for each strength reduction step. Figure 61 shows the softening rate for the stress point with the minimal strength values, whereas Figure 62 shows the mean softening rate for all stress points in softening. The minimal cohesion c_{min} is at 100% for all simulations, due to the small difference between peak and residual cohesion and the high cohesion softening ($m_{soft,c}$ = 5).

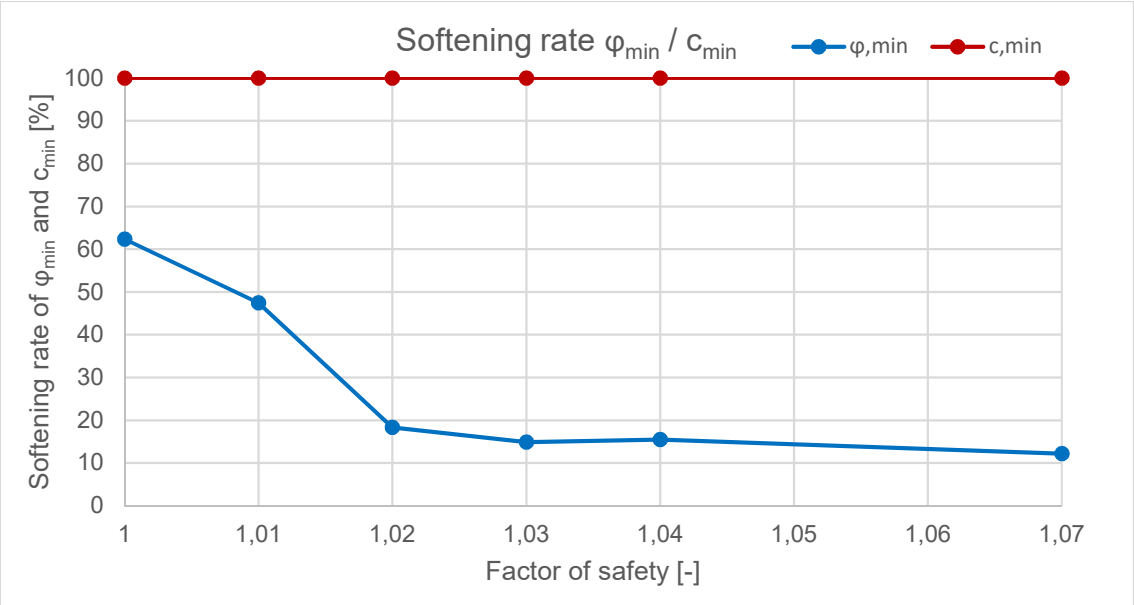

Figure 61 Softening rate of φ_{min} and c_{min} for different FoS after phase 6

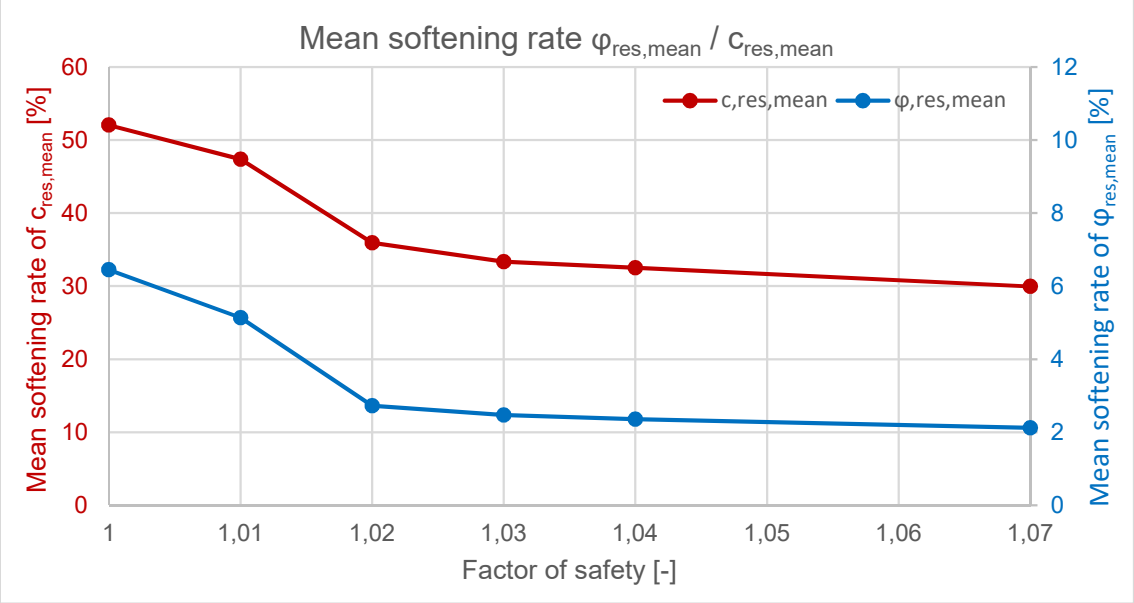

Figure 62 Mean softening rate of $\varphi_{res,mean}$ and $c_{res,mean}$ for different FoS after phase 6

It could be observed that a FoS above 1.02 results in a relatively stable softening rate, nearly unaffected by an increase of the FoS. This small amount of softening could be related to the development of pore water pressures before failure due to the undrained water level decrease. With decreasing stability under a FoS of 1.02, sufficiently displacements are produced to induce relevant strain softening in a stress controlled system. At this point of the simulation, failure state is almost reached. Hence, the sudden increase of the softening rate between 1.02 and 1.0, is produced due to the development of an distinct slip surface, as can be seen in Figure 63. Figure 63 illustrates the total amount of failure points (failure point history) after the last phase (phase 6), for different FoS.

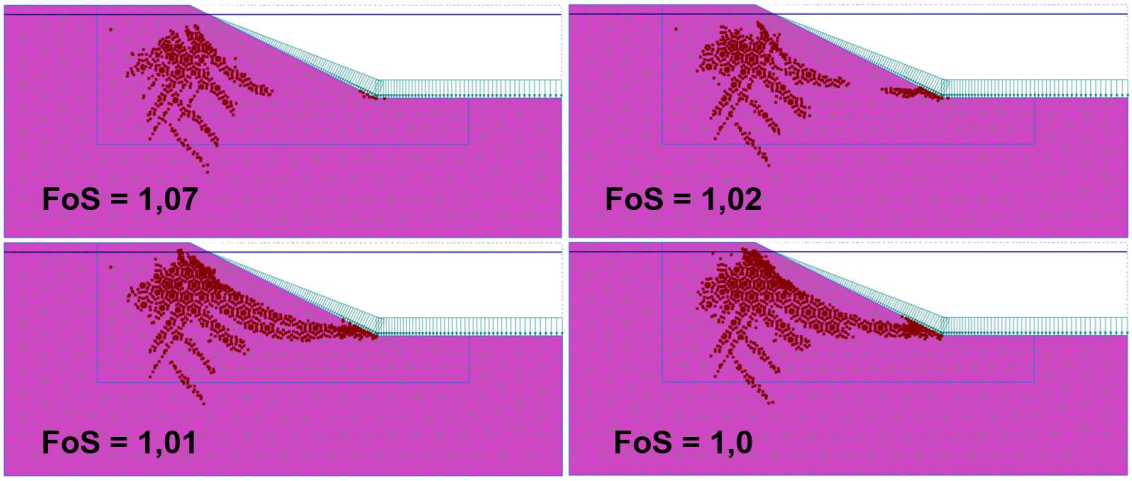

Figure 63 Total amount of failure points (failure point history) for different FoS – Phase 6 (consolidation)

Figure 64 shows the development of the total number of stress points / integration planes in softening. A very similar behaviour could be observed compared to the softening rates, with an increase of softening points / integration planes between 1.02 and 1.01. Again, the number of stress points / integration planes in softening is relatively constant before the appearance of the slip surface. Furthermore, the percentage of integration planes in softening is only a fraction of the stress points in softening, because strain softening rather concentrates on one or just a few planes.

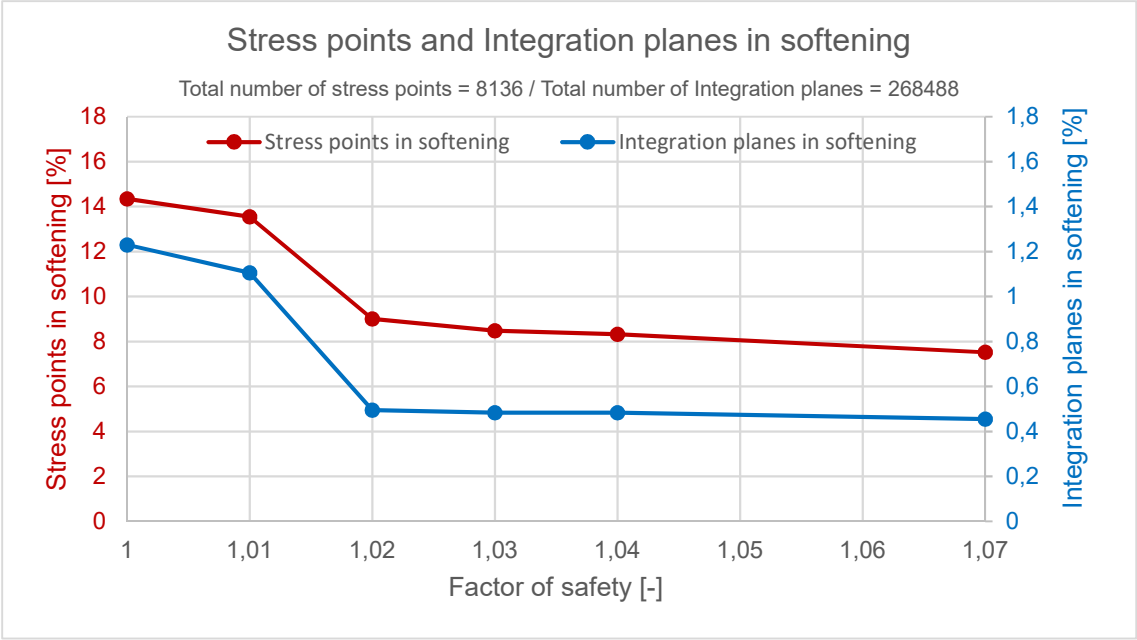

Figure 64 Percentage of stress points / integration planes in softening for different FoS after phase 6

6.4 Softening behaviour of a simple slope due to cyclic loading

The following discussion concerns the (softening) behaviour of a simple undrained slope under cyclic loading, obtained by simulating ten GW-fluctuation cycles (one cycle equals phase 3 to phase 6, see chapter 6.1). Simulations for all three constitutive models (HSS, BMnS, BMwS) were conducted.

During the GW-fluctuation cycles, the steady state pore water pressures of the slope tend towards a state with “mean” excess pore water pressures, corresponding to the two GW-tables. Pore pressures and effective stresses change significantly during each phase, before reaching that intermediate state. Hence, also without strain softening, the HSS model and the Basic models produced additional displacements after each GW-fluctuation cycle. This behaviour complicates the simulation of progressive strain softening with the BMwS for the analysed slope. On the one hand, low strength parameters are required to “push” the system close enough to failure, to produce deformations large enough to obtain relevant strain softening (see chapter 6.3.1). On the other side, any additional deformations, after relevant strain softening occurred, tend to lead to an immediate failure of the system without producing additional deformations. This is especially true for such simple systems as presented in this chapter. Accordingly, the BMwS produced failure in phase 7 (2. Drawdown), with the initial strength parameters (Table 7), whereas the BMnS and the HSS model calculated all ten GW-fluctuation cycles. Applying higher strength parameters for the BMwS, may lead to no failure but the strain softening is negligible. This is also the case for the later presented real project.

6.5 Conclusion

The stability analysis of a simple slope with GW – fluctuations showed that strain softening material certainly has an impact on the FoS. In this particular example, a difference of around 0.07 percentage points between the FoS of the BMwS and the FoS of the BMnS could be determined. The deformation characteristics are similar for all three models. However, the HSS model produces much larger displacements compared to the Basic models. Precise adjustment of the hardening parameter of the Basic models is recommended.

In a mainly load controlled system, as presented in this chapter, the softening behaviour is sensitive to the peak strength parameters. High peak strength parameters lead to almost no softening points in all applied phases. Reducing the peak strength parameters until the FoS of the analysed system is almost 1.0, leads to a significant number of softening points in the loading phases. Furthermore, a relevant strain softening is

apparent. The boundary between those states is very small. Thus, a simulation of a progressively deforming (failing) slope influenced by strain softening could not be accomplished for this model.

7 Multilaminate models applied to a real project

A slow moving sliding mass is located on the right orographic side of a water storage basin with fluctuating water tables. The movement rates of the sliding mass can be partially related to water level fluctuations in the reservoir. The objective of this chapter is to clarify whether strain softening in combination with the fluctuating water level might be a reason for the progressive displacements of the slow moving slope. Therefore, the BMwS was applied to the relevant soil clusters at the slope toe as shown in Figure 65. To compare the results with a system without strain softening behaviour, the BMnS was applied to the relevant soil clusters in a second simulation. Although cyclic loading indicated no progressive failure on simple models (Chapter 5), in a more complex model the strain softening might lead to significant stress redistributions and therefore to a recognizable influence of the strain softening on the displacement behaviour of the slope. Furthermore, the BMwS was applied with two different residual strength parameter sets, to analyse the influence of the residual strength parameters on the system. Hence, two different simulations with the BMwS were carried out. Once, with “high” residual parameters close to the peak strength parameters and once with “low” residual parameters (see Table 11).

7.1 Numerical model and material parameters

The numerical model is a plane strain simulation with undrained and drained materials. Due to the fluctuating water levels, a fully coupled flow deformation analysis would make sense. However, this is not possible due to some numerical problems with the multilaminate models in fully coupled analyses. Therefore, the water level changes were modelled in a staged construction with subsequent consolidation analysis. However, it has to be mentioned that these analyses do not lead to the same results as fully coupled analyses. Figure 65 shows the FE-model, with the softening materials marked in red.

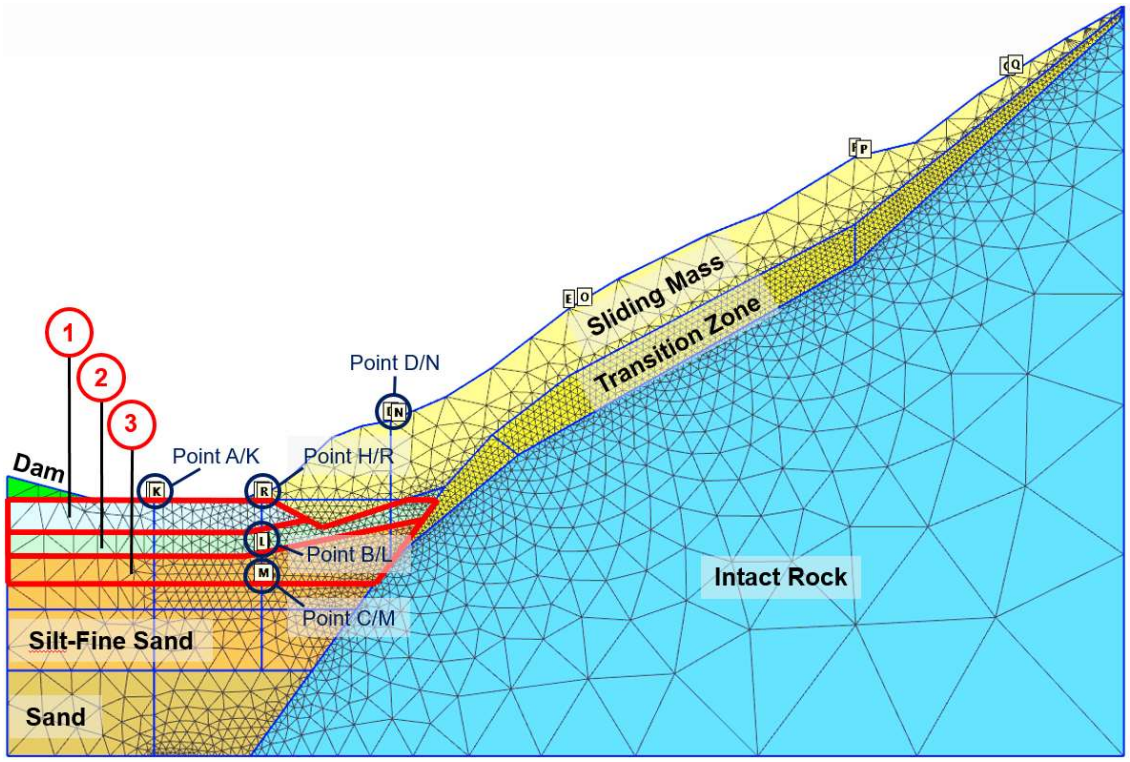

Figure 65 FE-model (Length: 400 m, Height: 360 m)

Beside the soil with softening behaviour (marked with the numbers 1, 2 and 3 in Figure 65 and Figure 66), following constitutive models and drainage types were used in this simulation.

- Intact Rock: Linear elastic, Non-porous
- Transition Zone: Mohr-Coulomb, drained
- Sliding Mass: Mohr-Coulomb, drained
- Dam: Linear-elastic, drained
- Silt-Fine Sand: Hardening Soil, Undrained (A)
- Sand: Hardening Soil Small, Undrained (A)

The soils with softening behaviour were simulated using the BMwS, Table 11 shows the assigned material parameters. The load fraction was set to LF = 0.1 for all calculation phases. For material parameters, which are not listed, see Table 4.

The same model was simulated with the BMnS for reasons of comparison. Hence, the influence of strain softening could be observed. The peak strength parameters of the BMwS were used as strength parameters for the BMnS. The remaining parameters for the BMnS correspond to the parameters for the BMwS (Table 11).

Table 11 Material parameters for soils with softening behaviour

Parameter	1) Fine Sand (FS)	2) Fine Sand, Silty (FSS)	3) Silt, Fine Sand (SFS)	Unit
$E_{oed,ref}$ =	35000	8750	7000	[kPa]
$E_{ur,ref}$ =	105000	45000	36000	[kPa]
m =	0.5	0.8	1	[-]
c'_{peak} =	2	2	3	[kPa]
φ'_{peak} =	35	32.5	27.5	[°]
R_f =	0.9	0.9	0.9	[-]
K_{0nc} =	0.4408 (high) 0.4627 (low)	0.4775 (high) 0.5 (low)	0.5538 (high) 0.5774 (low)	[-]
$G_{0,ref}$ =	175000			[kPa]
$\varepsilon_{deg,1}$ =	0.00001			[-]
$\varepsilon_{deg,2}$ =	0.005			[-]
φ'_{res} =	34 (high) 32.5 (low)	31,5 (high) 30 (low)	26,5 (high) 25 (low)	[°]
c'_{res} =	1 (for both)	1 (for both)	2 (high) 1 (low)	[kPa]
$A_{vol/dev}$ =	0.25	0.25	0.25	[-]
$SSS_{recovery}$ =	1	0	0	[-]

After the initial phase (gravity loading) and the simulation of the geological composition of the model, the following loading cycle was repeated ten times to simulate GW-fluctuations (Figure 66):

- Phase 1: GW – drawdown (2nd GW-table)
- Phase 2: Consolidation for 0.33 days (2nd GW-table)
- Phase 3: GW – raise (1st GW-table)
- Phase 4: Consolidation for 0.33 days (1st GW-table)

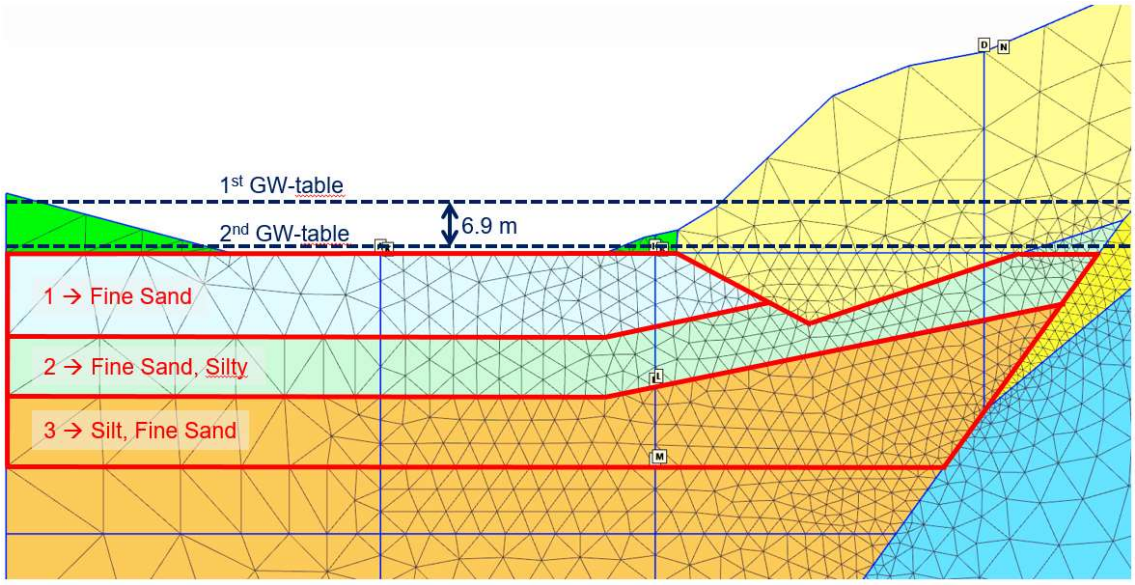

Figure 66 Section of the FE-model, GW-tables (BMwS)

7.2 Results

The progress of displacements for points A, D and H are illustrated in Figure 67 for the simulations with the BMnS and the BMwS with high residual parameters. Figure 68 shows the displacements for the same points for the simulations with the BMnS and the BMwS with low residual parameters. The plotted displacements are starting at phase 1, with the first drawdown. The points are located at the bottom of the reservoir (Points A and H) and at the foot of the sliding mass (Point D). All points show ongoing movements, mainly driven by phases simulating a drawdown. Only small differences could be observed by comparing the two BMwS with the BMnS. Furthermore, the BMwS with low residual strength parameters produces slightly less displacements at point D and H, compared to the results of the BMwS with high residual values.

Although adding more cycles would certainly cause further deformations, it can be observed that the additional obtained deformations are decreasing with each cycle for all three models. Plotting the displacements over time for the two BMwS (Figure 69 and Figure 70) confirms this observation. The general progress of the displacements of all observed points tend to level at a specific value after a certain amount of time.

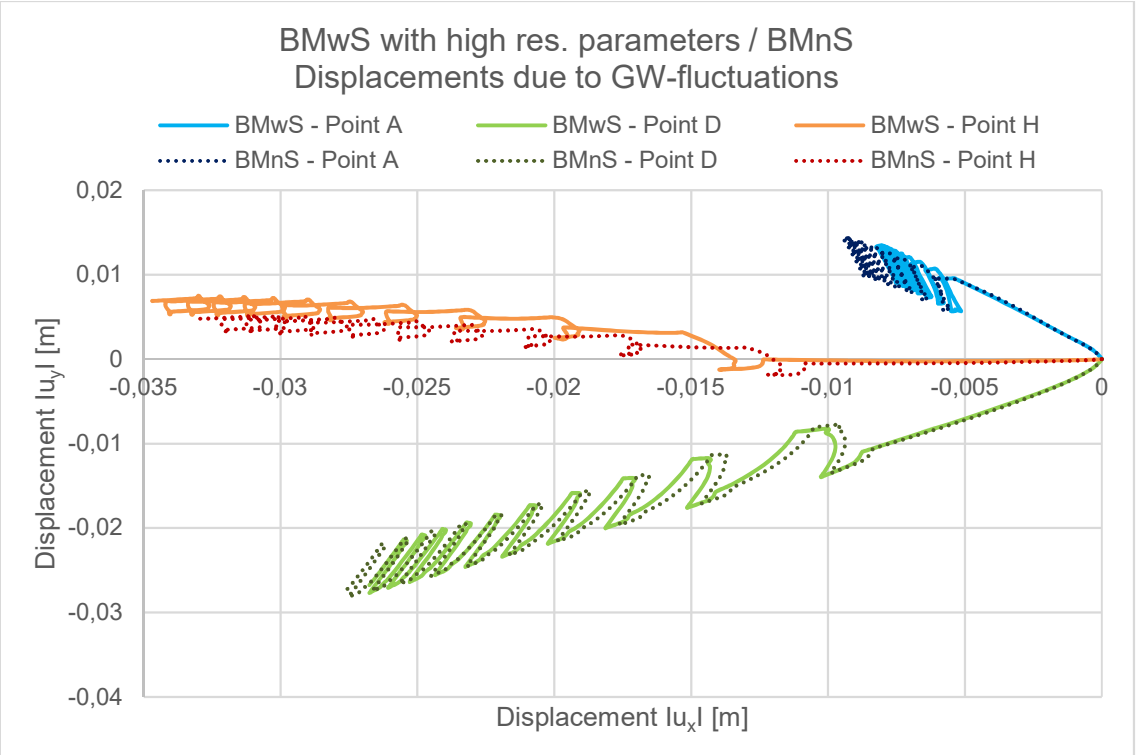

Figure 67 BMwS with high residual parameters / BMnS - Total displacements for points A, D, H

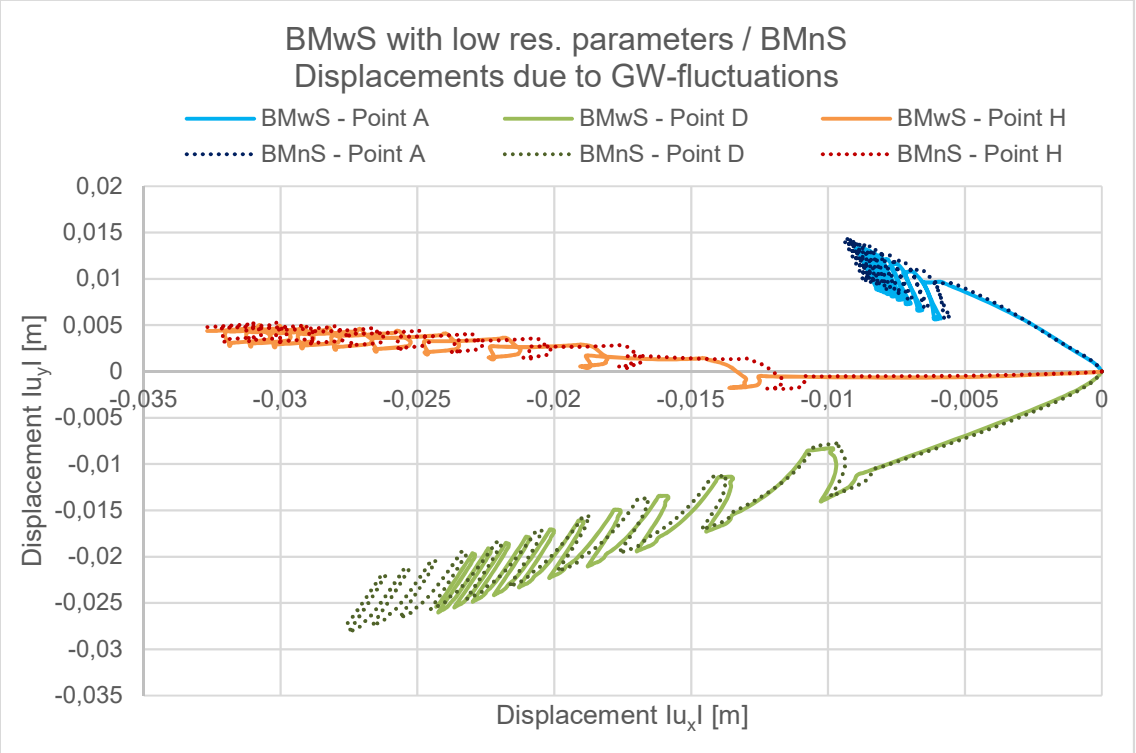

Figure 68 BMwS with low residual parameters / BMnS - Total displacements for points A, D, H

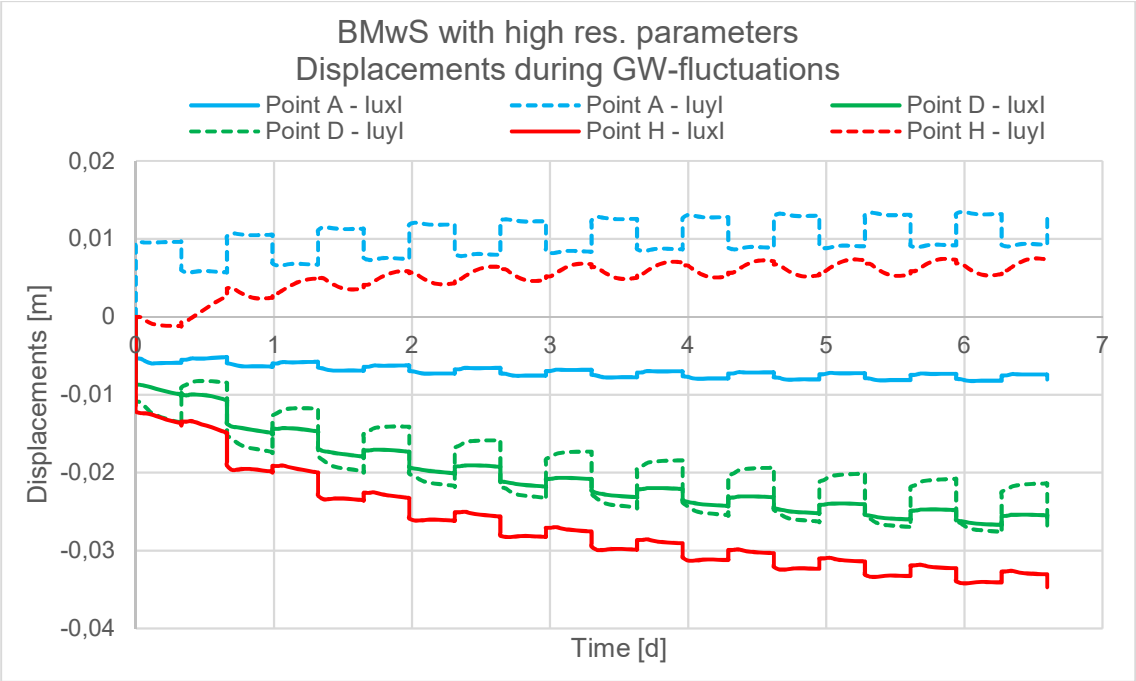

Figure 69 BMwS with high residual parameters - Total displacements vs time for points A, D, H

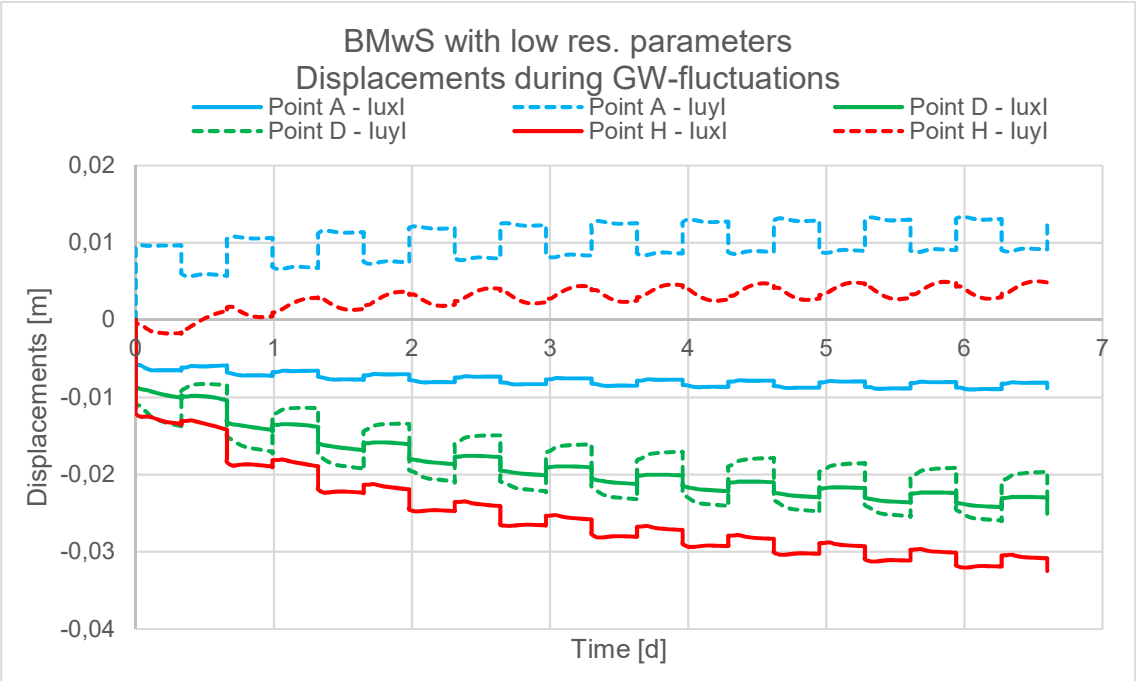

Figure 70 BMwS with low residual parameters - Total displacements vs time for points A, D, H

The development of the total failure points over the course of the GW-fluctuations are illustrated by Figure 71 (BMnS), Figure 72 (BMwS with high res. values) and Figure 73 (BMwS with low res. values). Hence, these figures illustrate the plastic point history, once for all materials and once only for the softening materials. Phase 1 indicates the first drawdown respectively.

All models obtained a few additional failure points due to the cyclic loading. Most of them emerged during the first cycles, especially during the phases simulating a drawdown. The majority of the additional failure points occurred in the clusters assigned with softening materials (= additional softening points). The BMnS produced the most amount of total failure points at the end of the simulation, whereas the total amount of failure points obtained by the two BMwS is certainly lower. A clear indication for a progressive failure by using the BMwS could not be detected.

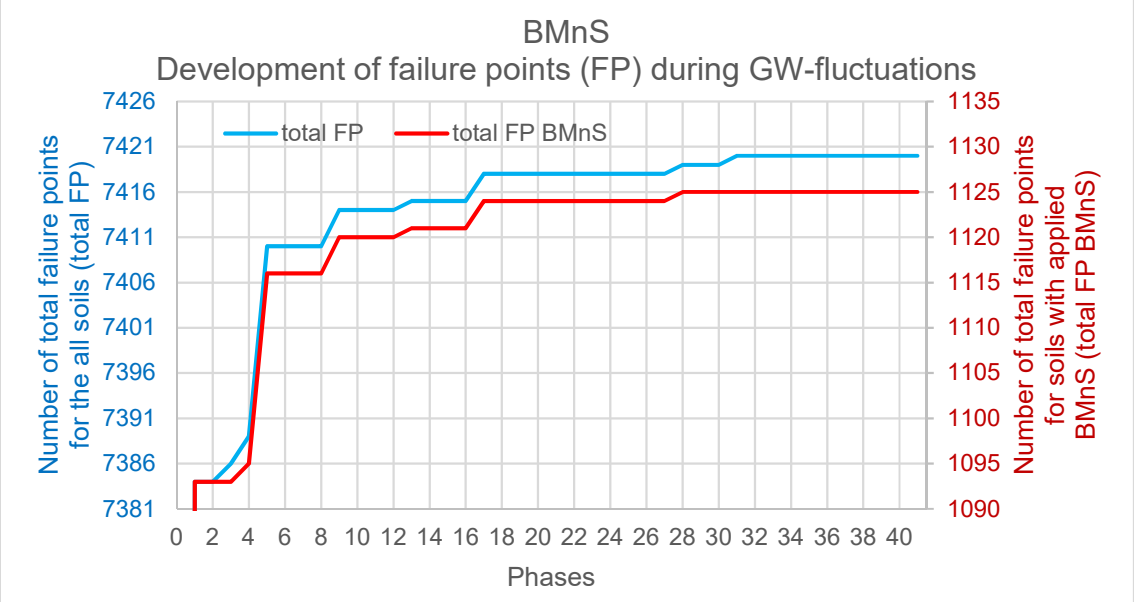

Figure 71 BMnS - Development of failure points (FP)

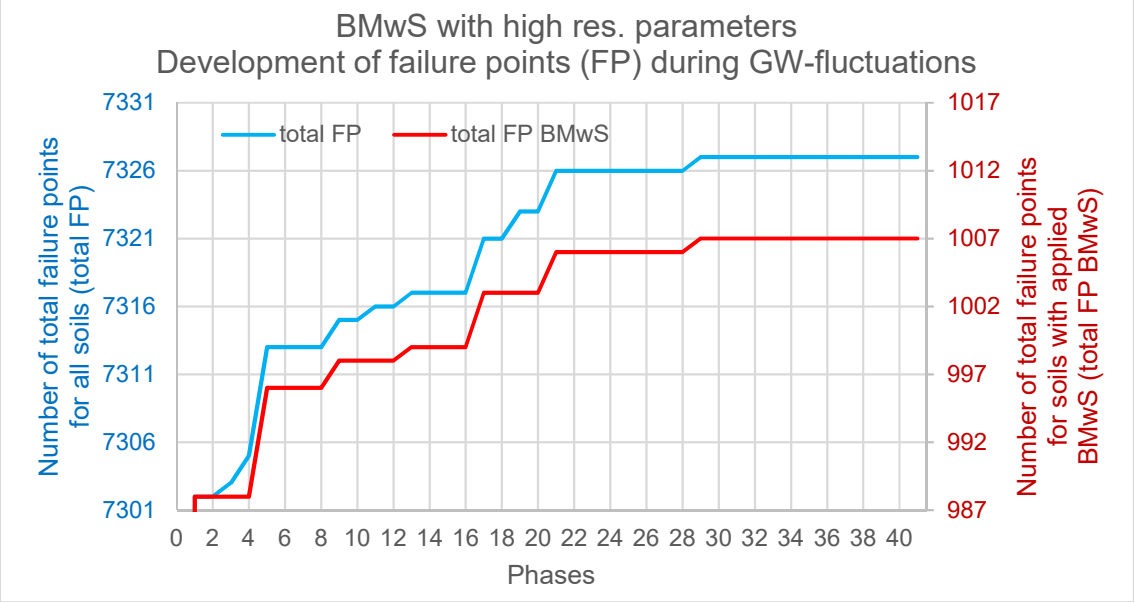

Figure 72 BMwS with high residual strength parameters - Development of failure points (FP)

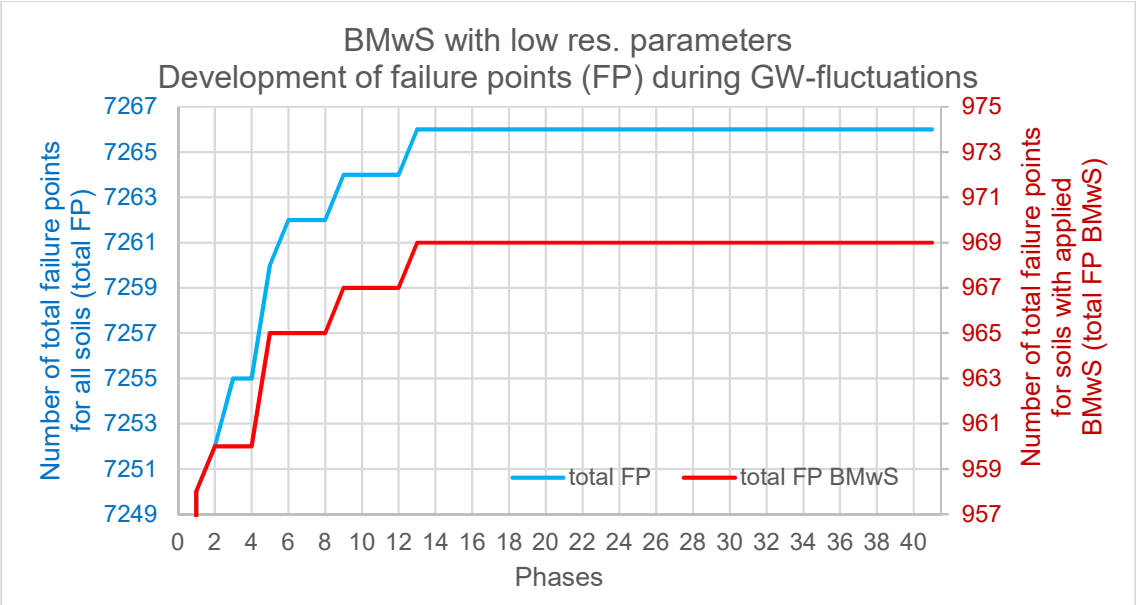

Figure 73 BMnS with low residual strength parameters - Development of failure points (FP)

The mean softening rate for all stress points in softening for all concerned soils (FS, FSS, SFS) is illustrated by Figure 74 (BMwS with high res. values) and Figure 75 (BMwS with low res. values). The mean softening rate after the simulation of the geological composition is compared to the rate after the simulation of the last drawdown (Phase 42). Slightly increasing rates could be observed for the FS-soil and the FSS-soil, especially for the BMwS with high residual parameters.

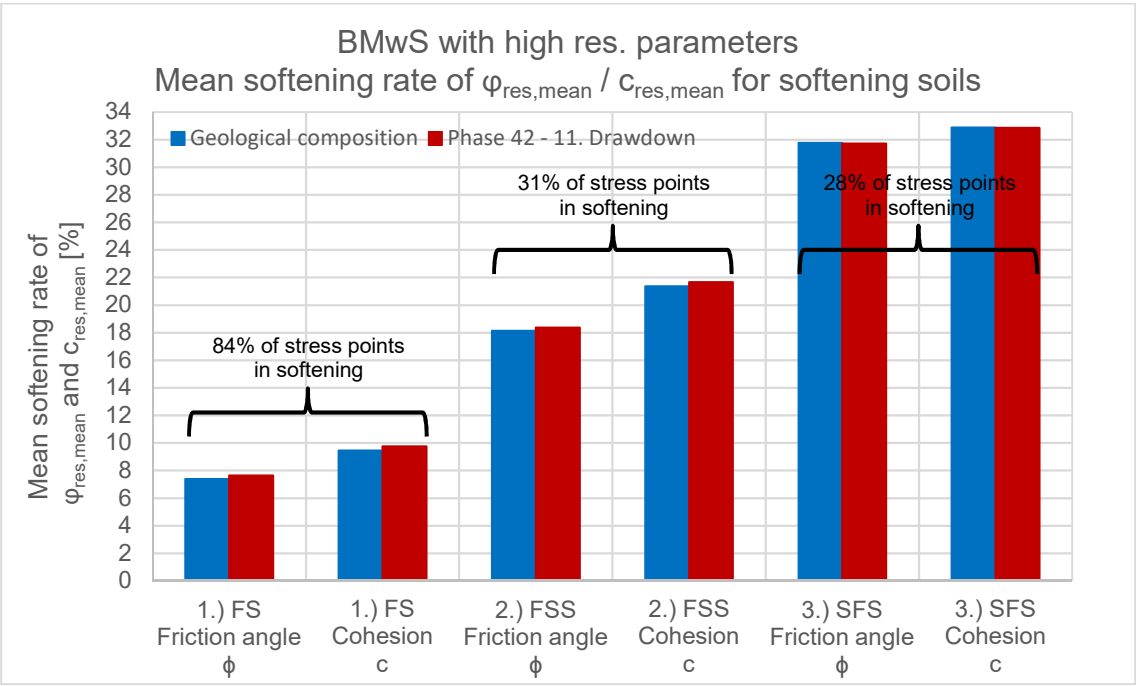

Figure 74 BMwS with high residual parameters - Mean softening rate of $\varphi_{res,mean}$ and $c_{res,mean}$ for all softening soils

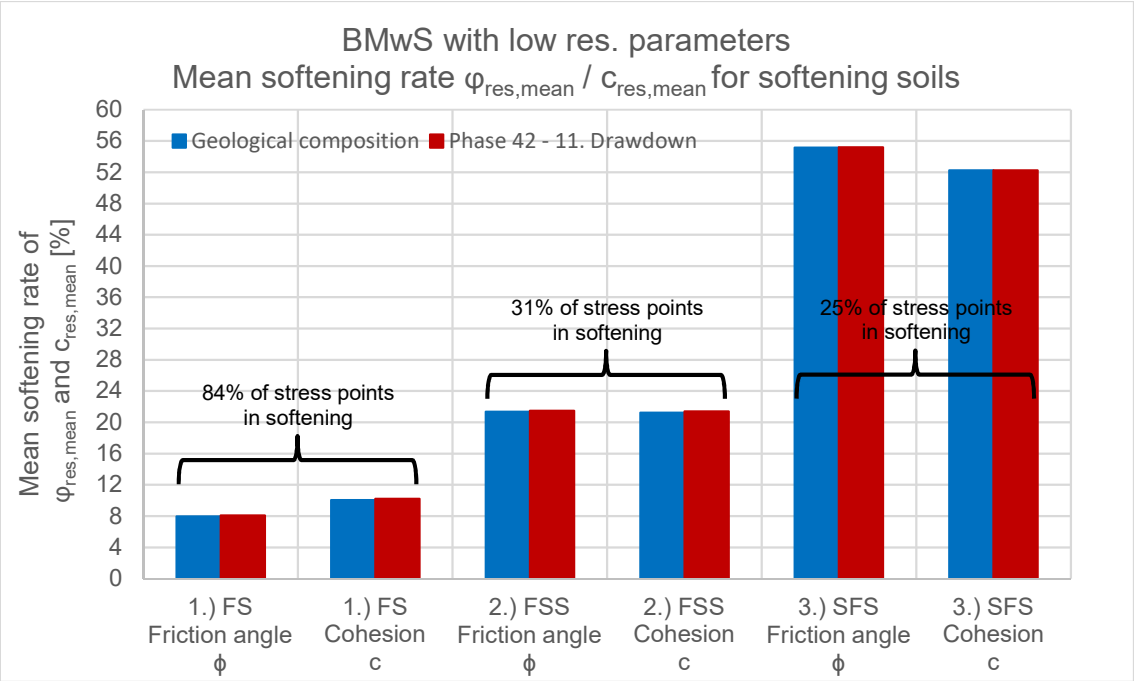

Figure 75 BMwS with low residual parameters - Mean softening rate of $\varphi_{res,mean}$ and $c_{res,mean}$ for all softening soils

7.3 Conclusion

For this particular case study, strain softening certainly has a very limited influence on the deformation of the system. Although some additional softening points are obtained during the loading cycles, the softening rate itself increased little or remained constant. Furthermore, applying lower residual strength on the BMwS did not increase the deformations in general. At certain points the deformation even decreased compared to the BMwS with high residual values. The assumption that lower residual values lead to higher deformations could not be confirmed. It has to be mentioned, that due to the changed residual friction angle also the volumetric hardening is changed. This might explain the unexpected behaviour of smaller deformations with lower residual strength parameters. Simulating a progressive failure by using the BMwS might be possible for this example, but parameters would have to be adjusted very precisely, to push the system closer to failure. Alternatively, the combination of the BMwS (strain softening behaviour) with a time-dependent constitutive model (“creeping”) may produce a progressive strain softening also in case of load controlled systems.

8 Conclusion and outlook

Two multilaminate constitutive models, the Basic model (Galavi 2007) and the Hvorslev model (Schädlich 2012), have been presented (chapter 4). Emphasis has been put onto the analysis of strain softening behaviour, which both models are capable of. Basic studies helped to identify several issues, which have to be considered if the presented multilaminate models are applied to real projects (chapter 5). Especially, the influence of the maximum load fraction, the partly inappropriate behaviour concerning the small strain stiffness and the determination of softening points have been investigated. Moreover, the multilaminate constitutive models have been compared against the commonly used Hardening Soil Small model, through basic studies and through stability analysis of a simple slope.

Furthermore, studies about the determination of the safety factor for a simple slope have been conducted. First, the influence of the different drainage types (Undrained (A), (B) and (C)) on the factor of safety of an undrained excavated slope has been investigated (chapter 2). Second, the influence of strain softening on the factor of safety of a slope under fluctuating water tables has been analysed (chapter 6). Thereby, an influence of strain softening on the factor of safety has been confirmed. However, simulating a progressive deformation behaviour of the slope, triggered by strain softening due to GW-fluctuations has not been observed, except for strength parameter sets, which are near the ultimate limit state.

Finally, a simulation of a real project has been analysed with the objective of observing a potential progressive failure controlled by strain softening (chapter 7). Again, this could not be validated in that particular case study with the used material models and the presented geometry. However, this might be feasible under specific circumstances.

9 Bibliography

Galavi, V. (2007). *A Multilaminate Model for Structured Clay incorporating Inherent Anisotropy and Strain Softening.* Dissertation. Institut für Bodenmechanik und Grundbau.

R.B.J. Brinkgreve, S. K. (2017). *Plaxis 2D Reference Manual.* Amsterdam.

Schädlich, B. (2012). *A Multilaminate Constitutive Model for Stiff Soils.* Dissertation. Institut für Bodenmechanik und Grundbau.

Schädlich, B. (2014). *How to use the multilaminate soil model MMS_HV.* Internal report. Institut für Bodenmechanik und Grundbau.

Scharinger, F. (2007). *A Multilaminate Model for Soil incorporating Small Strain Stiffness.* Dissertation. Institut für Bodenmechanik und Grundbau.

Verschiedene Autoren (2009). *Stabilisierung von Rutschhängen, Böschungen und Einschnitten.* 24. Christian Veder Kolloquium.

Wiltafsky, C. (2003). *A Multilaminate Model for Normally Consolidated Clay.* Dissertation. Institut für Bodenmechanik und Grundbau.